



UNIVERSITAT POLITÈCNICA
DE CATALUNYA
BARCELONATECH

Nonlinear and Stochastic Dynamics of Semiconductor Lasers: Modulation, Transient Dynamics and Synchronization

Jordi Zamora Munt

Memòria presentada per a optar al grau de Doctor per la
Universitat Politècnica de Catalunya

Directors:

Cristina Masoller
Jordi García Ojalvo

Departament de Física i Enginyeria Nuclear
Universitat Politècnica de Catalunya

Terrassa, 2011

Agraïments

Durant aquests anys dedicats a la investigació m'he adonat de com de dur pot arribar a ser el treball d'un investigador i a l'hora com de gratificant és veure que el fruit del teu esforç és reconegut. Vaig iniciar la tesi doctoral esperant arribar a convertir-me en un bon científic al acabar. De la mà dels meus directors de Tesi, la Cristina Masoller i en Jordi García Ojalvo, he anat creixent poc a poc com a científic però també com a persona. M'han anat guiant en la recerca polint amb paciència infinita el meu treball i jo he intentat donar el millor de mi, algunes vegades amb més èxit que d'altres. Agraïco molt la confiança que em van donar desde el primer dia i que any rere any m'han anat demostrant. Sempre he intentat ser mereixedor d'aquesta amb esforç i il·lusió. Sempre portaré amb mi l'optimisme contagiós del Jordi i la capacitat de treball de la Cristina.

Si demà em donessin la opció d'anar endarrere en el temps i tornar a triar en quin grup vull fer el doctorat, sens dubte, tornaria a triar aquest grup. En lloc podria haver estat envoltat de millors companys, amics i persones. Si no hagués estat pel Jordi Tiana, que va proposar el meu nom com a professor substituït i que em va permetre conèixer al Jordi i la Cristina, avui, probablement, no estaria escrivint aquestes línies. Moltes gràcies a la Lorena, la Belen, l'Andrés, el Pau, la Marta, el Nikhil, el Vito, la Lina, el Cristi, la Núria, el Toni i l'Oriol per haver estat amb mi quan els he necessitat, sempre disposats a ajudar i compartir. He après moltes coses al seu costat i desitjo poder seguir disfrutant de les magnífiques discussions de sobretaula amb tots ells. Un agraïment especial es mereixen la M. Carme i el

Ramon que sempre m'han donat grans consells i s'han preocupat per mi.

I want to acknowledge to Raj Roy the opportunity he gave me and his patience, warmth and hospitality that made me feel at home despite I was thousands of kilometers far away. His advices in how to proceed in the research and how to focus on the main ideas of the problem has completely changed my perspective of research. Also acknowledge to Bhargava and Adam and in extension to all the members of Raj's group for their help and confidence, receiving me as any other member of the group from the first day. I appreciate the valuable advices of Edward Ott and his receptivity. I have enjoyed a lot working with him.

He disfrutat profundament parlant de ciència amb tots aquells companys i companyes que he anat trobant en congressos al llarg d'aquests anys i que sense ells no haurien estat una experiència tant gratificant.

No vull deixar passar la oportunitat d'agrair a tots els companys de docència la magnífica experiència que ha suposat treballar amb ells. He intentat aprendre tant com he pogut, tant del Jordi com dels Jaumes, el Juan Carlos, el Jose Antonio, el Josep Lluís, la Crina, l'Idalberto, l'Alexander, el Carles, l'Antonio i de tants d'altres que han passat per la universitat i tots sempre s'han comportat de manera realment extraordinària.

El Pep i el David han estat els meus confidents durant aquells inoblidables sopars del dimecres i han estat al meu costat durant tot aquest temps. Fa temps que caminem junts i espero seguir fent-ho molts més anys. Ells m'han demostrat que ni el pas del temps ni la distància poden acabar amb l'amistat.

També vull donar les gràcies a tots els amics de Castellar (l'Ignasi, la Mari, el Santi, l'Edu, la Elena, l'Oriol, el Xavi i la Davínia) amb els qui he compartit tantes i tantes cerveses al voltant d'una taula parlant de tots els temes haguts i per haver, que m'han animat i esperonat quan ho he necessitat i que m'han fet sentir estimat i valorat. Sempre és reconfortant tornar-te a sentir com a casa.

Agraixo a la meva família la fe cega que han tingut en la meva feina. Sempre

s'han preocupat per mi i m'han ajudat en tot allò que han pogut amb abnegació i amor.

Qui més ha sofert tots els meus mal de caps i dubtes probablement ha estat la Mariona. M'ha aconsellat amb seny i objectivitat i sempre ha intentat animar-me quan les coses no anaven bé. Sense ella, no hauria arribat al final d'aquest camí. L'altre persona que sempre he tingut com a referència ha estat la Maite, qui ha cregut sempre en mi i les meves possibilitats, més fins i tot, que jo mateix. Sempre disposada a escoltar-me, ha aguantat estoicament les meves explicacions sobre la recerca que estava fent. A elles dues, les dues dones de la meua vida, a les que admiro i venero els hi dedico la meua Tesi.

Jordi Zamora Munt

Contents

Summary	1
I INTRODUCTION	5
1 Introduction to semiconductor lasers	7
1.1 Historic overview and types of semiconductor lasers	7
1.2 Edge-Emitting Lasers (EELs)	11
1.3 Vertical-Cavity Surface-Emitting Lasers (VCSELs)	15
1.3.1 Polarization switching and bistability	19
2 Rate-equation models of semiconductor lasers	23
2.1 Lang-Kobayashi model for an Edge-Emitting Laser with optical feed- back	24
2.1.1 Steady state solutions of the Lang-Kobayashi model: the ex- ternal cavity modes	27
2.2 SFM Model for a Vertical-Cavity Surface -Emitting Laser	30
2.2.1 Steady state solutions of the SFM model	33

3	Nonlinear and stochastic dynamics of semiconductor lasers	37
3.1	Effects of the current sweep across a bifurcation point	38
3.2	Optical feedback induced dynamics	40
3.3	Noise induced dynamics	47
3.3.1	Stochastic dynamics in multi-mode semiconductor lasers . . .	49
3.4	Synchronization of nonlinear oscillators	52
3.4.1	Synchronization phenomena in semiconductor lasers	53
3.4.2	Synchronization phenomena controlled by the system size . . .	57
II	RESULTS	61
4	Generation of optical pulses in VCSELs below the static threshold	63
4.1	Asymmetric triangular current modulation	64
4.2	Characterization of optical pulses	66
4.2.1	Influence of noise in pulse generation	72
4.3	Conclusions and discussion	74
5	Logical stochastic resonance in VCSELs	75
5.1	Aperiodic current modulation	76
5.1.1	Encoding scheme of the VCSEL logical response	78
5.2	VCSEL-based stochastic logic gate via polarization bistability	82
5.2.1	Analysis of the reliability of the stochastic logic gate	82
5.3	Conclusions and discussion	88
6	Transient LFFs in a semiconductor laser with optical feedback	91

6.1	Transient Low Frequency Fluctuations in the LK model	94
6.1.1	Probability distribution of the stochastic transient time	95
6.1.2	Effect of the parameters of the LK model on the stochastic duration of the LFF transient	99
6.1.3	Transients in a low-dimensional phenomenological model	105
6.2	Conclusions and discussion	108
7	Quorum sensing and crowd synchrony in delay-coupled semicon- ductor lasers	111
7.1	Modeling framework	112
7.2	Zero-lag synchronization of a network of coupled lasers	114
7.2.1	Transition to the synchronized state	117
7.2.2	Minimum number of lasers for stable synchronization	119
7.3	Conclusions and discussion	120
III	FINAL REMARKS	123
8	Summary of results and future work	125
8.1	Summary of results	126
8.2	Perspectives for future work	128
IV	Bibliography	131
V	Publications	157

Summary

The aim of this Thesis is the study how the interplay of nonlinear deterministic dynamics and stochastic dynamics of semiconductor laser (SCLs) influences information processing and synchronization in these devices, based on the numerical study of two well-known models for SCLs.

In Part I we discuss the basic features of semiconductor lasers and the different dynamical regimes that can be induced in these devices. In Chapter 1 we describe the main characteristics of the two types of SCLs used in this Thesis. Vertical-cavity surface-emitting lasers (VCSELs) are characterized by allowing the emission of two linear orthogonal polarizations due to the cylindrical geometry of the cavity and emit a single-longitudinal mode due to the small length of the active region. Edge-emitting lasers (EELs) can emit multi-longitudinal-modes with a polarization that is fixed by the rectangular cavity geometry. In Chapter 2 we describe the two rate-equation models for these SCLs. We use the so-called spin-flip model for VCSELs and the Lang-Kobayashi model for EELs. Those models are widely accepted and successfully describe the statistic and dynamic behaviour of these SCLs qualitatively and quantitatively. In Chapter 3 we introduce various of the dynamical regimes that can be induced in SCLs by external perturbations. In this chapter, we describe the effects of current modulation close to a bifurcation point where critical slowing down takes place. We introduce the different dynamical regimes induced by optical feedback focusing in the low frequency fluctuations (LFFs) regime and its origin and different descriptions. The influence of noise in SCLs is also discussed and

studied in the case of bistable polarization in VCSELs. Finally, different mechanisms for synchronization in SCLs are discussed and synchronization phenomena such as zero-lag synchronization, crowd synchrony and quorum sensing synchronization are presented.

Part II we present the results of our research. In Chapters 4 and 5 we study the interplay of polarization bistability, spontaneous emission noise and direct current modulation in VCSELs. In Chapters 6 and 7 we present results of the study of transient LFFs and synchronization in EELs.

Specifically, in Chapter 4 we present a novel method for the generation of sub-nanosecond optical pulses in directly modulated VCSELs via asymmetric triangular modulation of period of a few nanoseconds. We demonstrate the emission of pulses even when the laser operates, on average, below the cw threshold. For an optimal modulation asymmetry the effective threshold reduction is about 20%, the pulse amplitude is maximum and the dispersion of the pulse amplitude is minimum. We also show that stochastic resonance can be observed in this system for a realistic amount of spontaneous emission, maximizing the pulse amplitude and minimizing the amplitude dispersion. In Chapter 5 we demonstrate the phenomenon of logic stochastic resonance (LSR), by which the laser gives robust and reliable logic response to two logic inputs encoded in an aperiodic three-level signal directly modulating the laser bias current. We demonstrate that the probability of a correct response is controlled by the noise strength, and is equal to 1 in a wide region of spontaneous emission noise strengths.

In Chapter 6 we study the interplay between delay-induced multi-stability, chaotic transients, and noise, in the case of the low-frequency fluctuations of an EEL with optical feedback. The time delayed feedback renders the laser multi-stable, with a set of coexisting fixed points, and induces low-frequency fluctuations. The deterministic Lang-Kobayashi model predicts that, for a large range of realistic laser parameters, the LFFs are just a transient dynamics towards a stable fixed point. We analyze the

statistical properties of this transient LFF dynamics and investigate the influence of various parameters. We show that realistic values of the noise strength do not affect the average transient time or its distribution. On the other hand, nonlinear gain saturation has a strong effect: it increases both the duration of the LFF transients and the probability of noise-induced escapes from the stable fixed point. Our results suggest that the LFFs observed experimentally can be, at least in part, sustained by the interplay of noise and various nonlinear effects, which are phenomenologically represented by a gain saturation coefficient. Finally, in Chapter 7, we study a system of non-identical semiconductor lasers optically coupled to a central laser with a delayed star-type configuration. Our results show that, even though the lasers have different optical frequencies and the coupling is not instantaneous, zero-lag synchronization arises when the number of coupled elements is large enough. By changing a system parameter (namely, the lasers injection current), we can tune the synchronization transition (switch between a smooth and a sharp transition) which results in a common framework for crowd synchrony and quorum sensing. The dependence of the synchronization transition on the delay and coupling parameters is studied.

In Part III we summarize the main results presented in this Thesis and discuss the various possible future research lines. Finally in Part IV and Part V we list the bibliography and the publications and conferences where we presented our results.

The generation and control of different dynamics in lasers is still a topic of intensive research. We hope that this Thesis will contribute to the better understanding of the different stochastic and non-linear dynamics in semiconductor lasers and the constructive interplay that can sometimes occur between non-linearities and noise.

Part I

INTRODUCTION

Chapter 1

Introduction to semiconductor lasers

1.1 Historic overview and types of semiconductor lasers

From the first ideas of photons postulated by Planck in the early 20th century, the understanding of the light-matter interaction has attracted the interest of the scientific community not only because of the fundamental relevance of the processes involving photons and atoms but also because of the increasing number of applications that have appeared after each of the advances in this field. One of the most helpful devices for the progress of the science and technology in the last half century has been the laser.

Based on the stimulated emission mechanism suggested in 1917 by Einstein [1], the studies of Gordon, Zeiger and Townes in 1954 [2] demonstrated the amplification of microwaves in an ammonium media with a Fabry-Perot interferometer as a resonator. The invention was called the maser (microwave amplification by stimulated

emission of radiation) and a few years later was extended to the optical range, which led to the concept of **laser** (light amplification by stimulated emission of radiation). The laser was theoretically predicted by Schawlow and Townes [3] and Prokhorov [4] and later experimentally achieved by Maiman (1960) [5] in a ruby cylinder. A few years later, in 1964, Townes, Prokhorov and Basov were awarded the Nobel Prize “for fundamental work in the field of quantum electronics, which has led to the construction of oscillators and amplifiers based on the maser-laser principle”.

There are many types of lasers and they all share the following three features:

1. Pumping of energy that provides a large enough population of carriers in an excited state (the so-called population inversion).
2. Amplification of light that occurs when one photon interacts with an excited carrier and stimulates it to relax to a state of lower energy, emitting a photon identical to the original one.
3. Confinement of light inside a cavity is required to achieve large enough laser oscillation. The photons cross several times the active medium and are amplified until a threshold intensity is achieved.

Simultaneously with the appearance of the first lasers, von Neumann first [6] and Russell [7] and Basov *et al.* [8], a few years later, suggested the radiative recombination of electron-hole pairs in a semiconductor to amplify light. The first experimental laser light amplification based in semiconductor active medium was obtained in 1962 by three different groups [9, 10, 11]. The simple design of a p-n homo-junction (from a doped semiconductor material) required of high pump currents and cryogenic temperatures because of the absence of mechanisms of confinement for the carriers and for the optical field in the active region.

At this point, an endless race started to improve the characteristics of **semiconductor lasers** (SCL). In 1963, Kroemer [12] and Alferov and Kazarinov [13]

suggested the use of hetero-junctions (layers of semiconductors with wider band gaps clamping the active region) to increase the carriers lifetime. However, it was not until 1969 when Alferov *et al.* [14] implemented a SCL with hetero-junctions operating continuously and at room temperature. This marks the appearance of the first SCLs emitting light in the parallel direction to the active medium, the so called **edge-emitting lasers** (EELs), schematically displayed in Fig. 1.1. In the early 70's Nishimura *et al.* [15, 16] developed the first dynamic theory of SCLs.

In the following years, semiconductor materials that could provide long wavelengths sparked off a great interest. The reason was the discover of the window of low optical loss of wavelengths around $1.5 \mu\text{m}$ [17] and small or even zero dispersion at $1.3 \mu\text{m}$ [18] propagating in silica fiber optics and prepared the ground for the commercial optical fiber communications. In 1976 SCLs operating at $1.3 \mu\text{m}$ [19, 20] were built and in 1979 was achieved lasing at $1.55 \mu\text{m}$ [21, 22, 23, 24]. In 1977 the first live telephone traffic was sent through an optical fiber in Long Beach, California, and the first commercial compact discs (CDs) were distributed in 1979.

The use of periodic structures was proposed in 1972 by Kogelnik and Shank [25] for obtaining a single longitudinal mode amplification, by using distributed feedback (DFB) instead of mirrors to confine the field inside the cavity. From that moment the huge possibilities of periodic structures were exploited.

In 1978, Iga and coworkers suggested a different geometry for the SCLs [26], the **vertical-cavity surface-emitting lasers** (VCSELs) and the first VCSEL device was fabricated in 1979 [27]. As will be discussed later, VCSELs are characterized by a lasing emission perpendicular to the active region, displayed schematically in Fig. 1.3, and improve the EELs in many aspects [28]. The use of thin layers of active medium as well as the distributed Brag reflectors (DBRs) lead to a rapid progress in the improvement of the SCLs. The small size of the active layer ($< 50 \text{ nm}$) leads to the quantum confinement of the carriers (the so called quantum wells (QW) or multi-quantum wells (MQW) if there is more than one layer) that results

in an efficient gain section, and the high reflectivity of DBRs ($> 99\%$) increases drastically the lifetime of the photons inside the cavity. Koyama and coworkers in 1988 [29] reported the first VCSEL operating at room temperature and their further improving led to the progressive substitution of EELs for VCSELs in many commercial applications.

New types of semiconductor lasers are continuously being developed, for example lasers based in the technology of quantum dots [30, 31, 32]. These lasers use the three dimensional confinement of the carriers to produce a band structure similar to the atomic one. Long wavelength lasers based in the quantum cascade process were invented in 1994 [33] and have been improved to perform cw emission and high power at room temperature. Furthermore, lasers with shorter wavelengths are countinously developed since Nakamura invented the first violet and blue laser diodes [34, 35] and semiconductor lasers currently can be fabricated with in a wide range of wavelengths in the visible spectra.

In the so-called spin-vcseles the output polarization is controlled by the injection of spin-polarized electrons and offer the important advantage, in addition to enhanced polarization stability, of a reduced threshold current [36, 37].

Semiconductor ring lasers are a type of semiconductor laser in which the light is confined in a circular waveguide structure. As a result, they can generate light in two opposite directions and are receiving increasing attention as they are attractive light sources in photonic integrated circuits [38] Recently, semiconductor random lasers are being developed and fabricated. In these lasers the feedback for laser action is not provided by an external resonator, but by scatterers that result of growth imperfections and which are randomly distributed in the active medium, or which by themselves act as optical amplifiers [39].

Nowadays, lasers are common elements in our daily life and SCLs are broadly used in many applications. Actually, SCLs covered the 60% of the laser market in 2004 in terms of revenues [40]. The reasons for this success are their special

characteristics. Their low cost is an important advantage but, also the small size and packaging capability, their reliability and safety, the low power consumption and the wide range of wavelengths that they cover. Therefore, is not surprising that there are dozens of applications. Some of the most important are related with fiber-optics communications, without which the Internet could not have grown so rapidly, and the high density information storage provided by CDs, DVDs and more recently blue-ray disc players and recorders. They are also used in scanners, barcode readers, laser printers, laser pointers, or high precision sensors (e.g. in laser Doppler velocimetry).

In this thesis we have focused our attention in SCLs of two types: Edge-Emitting Lasers (EELs) and Vertical-Cavity Surface-Emitting Lasers (VCSELs). Both types are usually pumped electrically (although they can be pumped optically by an external light source), and the active medium is commonly built on MQW structures. Their main difference is in the geometry of the cavity. While EELs emit light in the direction parallel to the active medium, in VCSELs the light is emitted in the perpendicular direction to the active medium. High reflectivity mirrors are required in VCSELs which are provided by DBRs because of the short time that each photon spends inside the active region in a round trip. In the two following sections we will describe the main characteristics and differences between EELs and VCSELs.

1.2 Edge-Emitting Lasers (EELs)

Edge-emitting lasers are semiconductor lasers that emit in the parallel direction of the active region of the semiconductor p-n junction where the recombination of carriers (holes and electrons) takes place due to the high density of both. The carriers can be excited by an electric source applied in the metallic contacts at the ends of the device. When the photons propagate along the active region and interact with excited carriers, the radiative recombination of electron-hole pairs takes place

and stimulated emission occurs. If the population inversion in the active layer is large enough to overcome the losses, laser light is obtained.

The active layer in EELs has a typical length of 200-500 μm (Fig. 1.1). It provides a relatively long propagation time of the photons inside the active medium that enhances the probability of stimulated emission. The longitudinal length of an EEL is large compared with a VCSEL (but short compared with other lasers), providing a large gain that does not require a high carrier and photon confinement which simplifies the structure of the device. This characteristic of the EELs leads to a spacing of longitudinal modes of the order of 100-200 GHz, allowing the amplification of many longitudinal modes. Thus, frequently, the EELs are multi-longitudinal mode lasers.

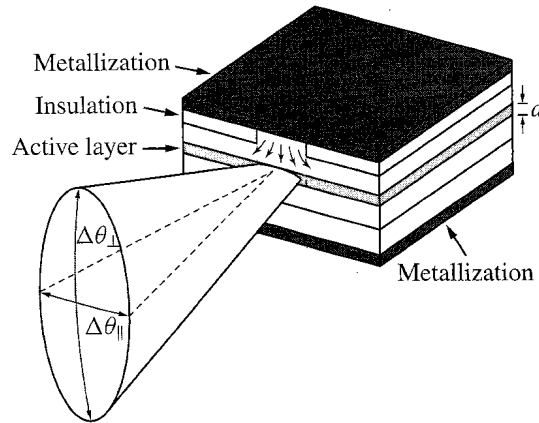


Figure 1.1: Schematic structure of an EEL. From [41].

In semiconductors, the carriers diffuse in the transverse direction of the junction surface, which reduces their density, so several mechanisms have been developed to improve their confinement. Carrier confinement can be achieved by using heterostructures, characterized by clamping the active region between layers of two oppositely doped semiconductors. This structure also improves the confinement of the electric field inside the cavity of the laser, due to the different refractive index

of the doped semiconductor layers. Furthermore, reducing the size of one of the metallic contacts or adding an insulator, enhances the population inversion in a reduced region of the active medium, leading to the so-called gain-guided structures. In index-guided structures, a semiconductor of a different refractive index is grown in the sides of the active medium and is used to act as a waveguide that provides a lateral confinement of the field. These restrictions allow the emission of a single transverse mode. The different lateral dimensions of the active region's cross section produce an asymmetric divergence that results in an elliptical profile of the emitted output beam that makes it difficult to couple to an optical fiber. Furthermore, the linear polarization of the electric field is selected by the structure of the cavity geometry.

The confinement of the electric field in the longitudinal direction is required in order to increase the amount of stimulated light. The relatively high gain of the EELs does not require large reflectivities for the amplification of the light. A reflectivity of $\sim 30\%$ provided by carefully polished facets of the cavity is usually enough for lasing in the so called Fabry-Perot SCLs. Other mechanisms are proposed to improve the characteristics of the emitted light such as distributed feedbacks (DFBs), characterized by a periodic structure in the active region, or distributed Bragg reflectors (DBRs), characterized by a grating in the refractive index outside the active region. These structures have the advantage of selecting a longitudinal mode with a frequency directly related with the periodicity of the structure.

The single- or multi-longitudinal mode performance of the laser are due to the amplification of the cavity modes inside the gain curve with a modal gain larger than the losses (Fig. 1.2(a)). Because the gain bandwidth is in the range of tens of THz, 10-20 longitudinal modes can be emitted in multimode lasers. As mentioned above, DFBs and DBRs are frequency-selective gratings that can be used to obtain a single mode emission (Fig. 1.2(b)) that is suitable for communications in single-mode optical fibers. Furthermore, DBRs allow to decrease the length of the cavity, as occurs in VCSELs, which will be described in the next section. In many of

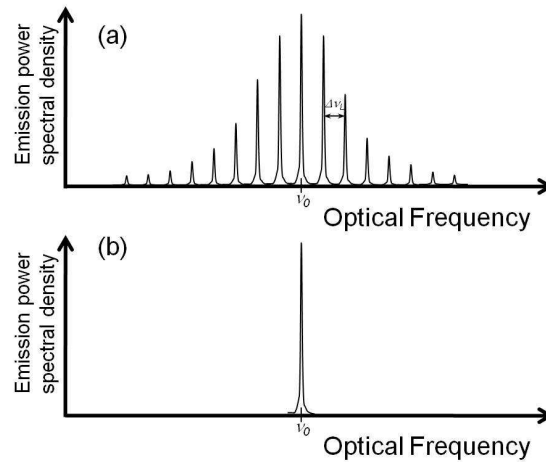


Figure 1.2: Optical spectra of an EEL. (a) In multi-longitudinal mode lasers the net gain bandwidth is larger than the spacing between modes, $\Delta\nu_L$, and several modes can be emitted. (b) In single-longitudinal mode lasers the cavity losses are such that only one mode at frequency ν_0 is emitted.

the applications where SCLs are used, the emitted light can be reflected by an external element, e. g. the surface of a CD or DVD or the coupling junction end of an optical fiber, acting as a mirror that reinjects the light again into the laser. Commonly, EELs are very sensitive to external perturbations such as feedbacks due to the high transmittivity ($\sim 70\%$) of their facets. The external mirror creates an external cavity that can produce undesirable destabilization of the output light. The external mirror allows the appearance of **external cavity modes** of a smaller spacing than the spacing of the laser cavity modes, increasing the linewidth [42] and inducing complex dynamics even in single mode lasers [43]. This dynamics was already reported in the 70's [44] and, in the last 40 years, many efforts have been devoted to investigate and control the output light of a SCL subjected to optical moderate feedback [45]-[51].

1.3 Vertical-Cavity Surface-Emitting Lasers (VCSELS)

The appearance of VCSELS was a revolution in optical communication technologies. Their innovative geometry provided specific characteristics for these devices. To better understand what does the VCSELS so particular we will describe their general features in detail.

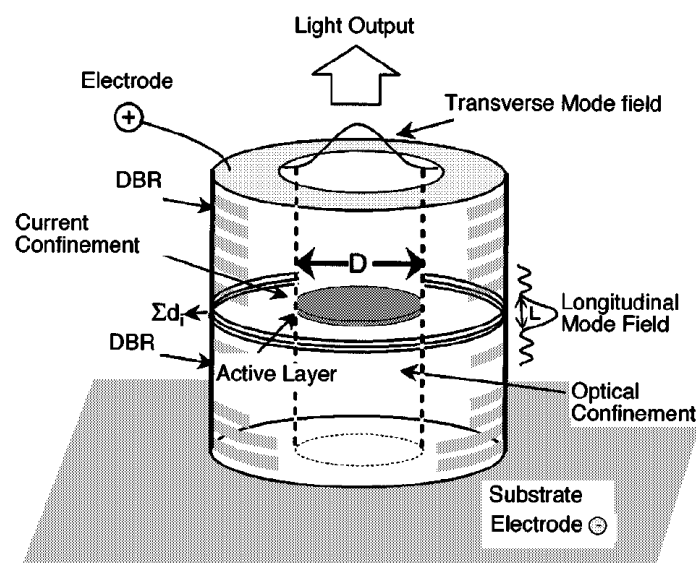


Figure 1.3: Schematic structure of a VCSEL. From [52].

As discussed in Sec. 1.1, the key idea was to reduce the size of the active layer by changing the direction of the light being amplified inside the cavity, making it perpendicular to the junction and the substrate, as shown in Fig. 1.3. The huge effective reduction of the size of the cavity compared with the EELs has important consequences in the laser threshold and efficiency, among others.

In commercial VCSELS the active region is usually a structure of one to four QW layers, each of 5 to 10 nm. The small thickness of the active region implies that on each roundtrip of the photons inside the cavity, the gain produced by the stimulated

emission is very low. To solve this, high reflective mirrors (with reflectivity $>98\%$) are required for cw emission at room temperature. The most commonly used mirrors are distributed Bragg reflectors (DBRs).

DBRs are index-modulation gratings of pairs of layers of doped semiconductor (or dielectric) materials with high and low refractive index where each pair has a length of $\lambda/2\bar{n}$, where \bar{n} is the averaged refractive index of the pair and λ is the reflected Bragg wavelength. By adding a large enough number of layers, it is possible to obtain reflectivities $>99\%$ due to the constructive superposition of the reflected light. Usually, DBRs of 99.9% are used for the mirror at the output of the VCSELs and DBRs of almost 100% reflectivity for the mirror at the bottom of the cavity, which requires a number of layer pairs that goes from less than 10 for dielectrics to 40 for semiconductors.

By construction, the confinement of the field inside the cavity produces a standing wave from the top DBR to the bottom one of a few λ 's. In order to optimize the efficiency of the stimulated emission, the active region is placed in the anti-nodes of the standing wave with a width limited to $\lambda/4n$, where λ and n are the wavelength and the effective refractive index inside the cavity.

The threshold current I_{th} is

$$I_{th} = SJ_{th} = \frac{eVN_{th}}{\eta_i\tau_N} \quad (1.1)$$

where S is the transverse section of the cavity, J_{th} is the threshold current density, e is the electron charge, V is the volume of the active region, N_{th} is the threshold carrier density, η_i is the injection efficiency, defined as the fraction of the injected current that actually contributes to the injected carriers in the active region, and τ_N is the recombination lifetime of the carriers. This equation shows that the threshold current is proportional to V , where $V = Sd$ with d the thickness of the active layer. In VCSELs d is comparable to that in EELs (Table 1.1). However, in VCSELs S can be reduced drastically because the gain, given by the overlap between the field inside the cavity and the carriers in the active layer, is independent of the cross section of

Table 1.1: Comparison of parameters between a conventional EEL and a VCSEL [41].

Parameter	Symbol	EEL laser	Surface Emitting Laser
Active layer thickness	d	$100\text{\AA}-0.1\mu\text{ m}$	$80\text{\AA}-0.5\mu\text{ m}$
Active layer area	S	$3\times 300\mu\text{ m}^2$	$5\times 5\mu\text{ m}^2$
Active volume	V	$60\mu\text{ m}^3$	$0.07\mu\text{ m}^3$
Cavity length	l	$300\mu\text{ m}$	$\simeq 1\mu\text{ m}$
Threshold current	I_{th}	$\gtrsim 1\text{ mA}$	$< 1\text{ mA}$
Longitudinal mode spacing	$\Delta\nu_L$	$100\text{-}200\text{ GHz}$	$>10\text{ THz}$

the cavity [41]. So, e.g. typically an EEL has an active volume of $\sim 60\mu\text{m}^3$ while a VCSEL, of $\sim 0.06\mu\text{m}^3$. This directly affects the threshold current of VCSELS that is of the order of a few mA or lower, while of EELs, it is of the order of several mA or higher. Furthermore, the so called power conversion efficiency can be larger than 50% in VCSELS [41].

In VCSELS the small cavity length (allowed by the use of DBR mirrors) enlarges the spacing between longitudinal modes of the cavity. The emission wavelength of the laser is given by the overlapping of the longitudinal modes of the cavity and the gain bandwidth of the semiconductor QW, which is smaller than the longitudinal mode spacing. Therefore, VCSELS are single-longitudinal-mode lasers by construction.

The control over the transverse geometry allows the use of a circular aperture, which gives an output beam with a circular intensity profile. This circular geometry makes the coupling of the laser to an optical fibers easy and efficient. However, the intensity profile depends on the pump current, among other parameters, resulting in different transverse modes. For low pump currents close to the threshold current, which is the parameter region explored in this thesis, only the fundamental transverse mode is emitted while far from threshold higher transverse modes can be

excited or emitted [53, 54, 55].

In summary, due to their improved design, VCSELs provide a number of advantages:

- Low threshold operation and power consumption.
- Single-longitudinal-mode operation.
- Circular beam for direct fiber coupling.
- Easy integrability in large-scale two-dimensional (2D) arrays.

The cylindrical symmetry of the VCSELs cavity has important consequences for the polarization of the emitted light. This geometry allows the emission of orthogonal linear polarizations that display a variety of dynamical phenomena, involving polarization fluctuations, as will be discussed in detail in Chap. 3. This is commonly considered a drawback of these devices and many efforts have been devoted to control their polarization [56, 57, 58, 59, 60].

However, anisotropies such as birefringence and dichroism, in the cavity and in the gain medium break the circular transverse symmetry, which results in the existence of two preferred linear orthogonal directions. The different gain-to-loss ratio in different directions of the crystal can be attributed to dichroism and considered as an amplitude anisotropy while the phase anisotropies are given by the differences in the refractive indexes associated with the linear birefringence.

Birefringence produces a splitting in the optical frequencies of orthogonal linear polarizations that can be of the order of a few GHz to tens of GHz. The birefringence can be related to the electro-optic effect [61] and to the elasto-optic effect [62]. The separation in frequencies can be observed in the optical spectra of the lasers. When two linear orthogonal polarizations are allowed, commonly referred as x for the mode with lower frequency and y for the mode with higher frequency, the optical spectra

shows peaks at different frequencies, one for each linear polarization (Fig. 1.4). In elliptically polarized light the two peaks are frequency-locked.

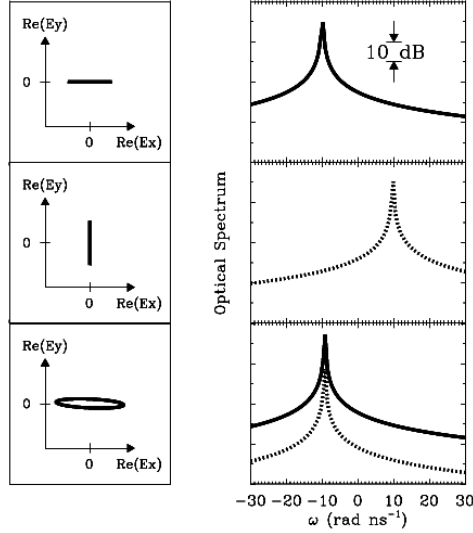


Figure 1.4: Basic polarization states. The optical spectra of the complex electric field amplitudes E_x (continuous line) and E_y (dashed line) is shown. The frequency splitting between the two linearly polarized modes is given by the linear birefringence. Top: x polarization and middle: y polarization. They frequency lock in the elliptically polarized state (bottom), but have different power strengths. From [63].

1.3.1 Polarization switching and bistability

A relevant feature of VCSELS is related to the stability of the two orthogonal linear polarizations. When the VCSEL begins to lase one linear polarization dominates, and, in many devices, when the injection current is increased above a certain value, it is observed that the emission switches to the orthogonal linear polarization. The relative intensity of the polarization peaks in the optical spectra changes abruptly, leading to the **polarization switching** (PS) effect. The dominant mode of polarization emitted at low currents turns off and the orthogonal mode turns on. Which

mode, x or y , dominates at low current levels depends on the specific device and is usually considered a consequence of the dichroism.

The PS phenomenon usually involves hysteresis, as when the current decreases the switch back occurs at a lower current value (Fig. 1.5 upper panel). The precise values of injection current at which the PS occurs, that define the boundaries of the **bistability region**, depends on several parameters and on the rate of variation of the injection current. If the current is continuously varied, dynamical PS occurs, as will be discussed in detail in Chap. 3. Stochastic polarization switching can also occur (Fig. 1.5, (lower panel)) and has been interpreted in terms of Kramers' hopping in an effective 1D double-well potential [65, 66].

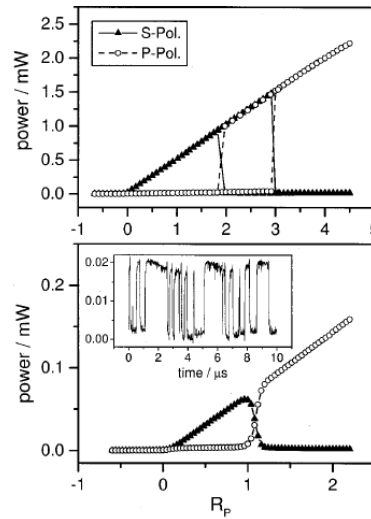


Figure 1.5: Polarization-resolved optical power as a function of the pump rate for two oxide confined single-transverse-mode VCSELs. VCSEL A (upper panel) displays polarization hysteresis while VCSEL C (lower panel) displays stochastic polarization switching. Inset: time series of the optical power of one polarization at the center of the switching region ($R_P = 1.1$). From [64].

Several physical mechanisms can be involved in the PS, and various explanations for this effect have been proposed. The different modal gain due to thermal effects,

the different optical frequencies in birefringent media, but also the combination of the birefringence and the spatial-hole burning have been described as a mechanisms that could lead to PS. In the first case [67], an increase of the pump current produces a self-heating of the device. A red-shift of the cavity mode frequencies occurs and a red-shift of the gain spectrum, which is larger than the red-shift for the cavity resonances. As a consequence, the mode with larger gain changes (Fig. 1.6(a)). A second explanation is proposed in [68, 69]. By considering frequency dependent losses, at low pump current one mode is suppressed because the cavity losses are larger than the material gain while the orthogonal mode has a positive net gain. At high pump currents, the PS occurs when the modes exchange the sign of the net gain (Fig. 1.6(b)). These explanations are intuitive and simple but do not explain some experiments involving hysteresis and PS at constant temperature [70, 71]. An alternative explanation for PS and hysteresis without considering thermal effects was proposed in [72, 73, 74] as a combined effect of birefringence and saturable dispersion associated with the α factor. The spin-flip model developed in Refs. [72, 73, 74] will be the model employed in this Thesis for describing the polarization of VCSELs.

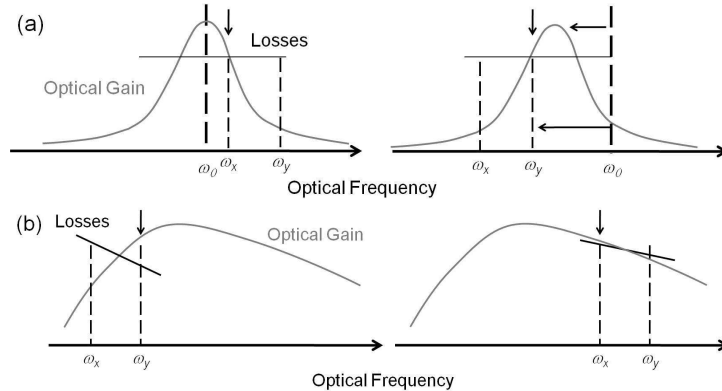


Figure 1.6: Schematic representation of the gain-to-loss ratio of the polarizations x and y . (a) Red-shift effect for small (left) and large (right) pump currents and (b) frequency dependent losses for small (left) and large (right) pump currents. Arrows show the lasing mode.

Chapter 2

Rate-equation models of semiconductor lasers

The rate equations that describe the dynamics of lasers can be derived for the semiclassical Maxwell-Bloch equations for the optical field, population inversion and material polarization [75]. These variables decay with different time scales, and when one decay rate is comparatively fast the corresponding variable adiabatically adjusts to the other variables. A general classification of lasers can be obtained in terms of the number of variables that can not be adiabatically eliminated [75]. Single-mode semiconductor lasers are class-B lasers, characterized by a fast relaxation of the polarization, thus only two equations, one for the optical field and another for the carriers, are required to describe their dynamics.

Semiconductor lasers can be modelled with different degrees of detail by using models with partial derivatives, the travelling wave models, microscopic models, etc. In this chapter, we discuss in detail the simple rate-equation theoretical models used in this thesis to describe the influence of optical feedback in EELs and current modulation in VCSELs.

2.1 Lang-Kobayashi model for an Edge-Emitting Laser with optical feedback

Many efforts have been devoted in last decades to study EELs and, nowadays, these lasers are very well understood theoretically. In this section we introduce the model of an EEL with **optical feedback** from an external mirror (Fig. 2.1). A simple modification of this model will give us the rate equations for an EEL with optical injection, which will be used in the study of coupled SCLs. In 1980 Lang

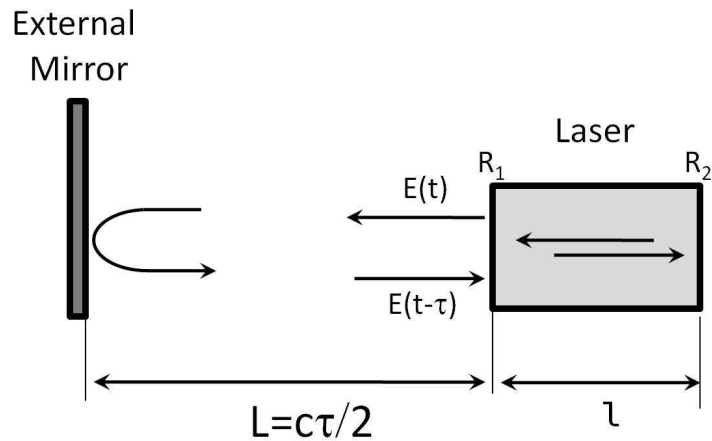


Figure 2.1: Schematic representation of a laser with optical feedback from an external mirror placed at a distance L from the laser. The electric field, E , reflected in the external mirror returns to the laser after a time τ . l is the length of the internal cavity of the laser and R_1 and R_2 are the reflectivities of the laser mirrors.

and Kobayashi proposed a model for an EEL with optical feedback [76], the so called **Lang-Kobayashi model** (or simply LK model), which had great success in describing the characteristics of dynamics induced by feedback from an external mirror. According to this model, the rate equations for a single mode EEL with optical feedback can be written in terms of the slowly-varying complex amplitude

of the optical field, E , and the carrier number, N , as

$$\frac{dE}{dt} = k(1 + i\alpha)(G(E, N) - 1)E + \kappa_{fb}E(t - \tau)e^{-i\omega_0\tau} + F_E(t), \quad (2.1)$$

$$\frac{dN}{dt} = \gamma_N(\mu - N - G(E, N)|E|^2) + F_N(t). \quad (2.2)$$

Both E and N are dimensionless variables, $|E|^2$ is proportional to the number of photons in the cavity and N is the carrier population in excess of its value at transparency normalized to the value of that excess at the lasing threshold. The function G is the optical gain, given by

$$G(E, N) = \frac{N}{1 + \varepsilon|E|^2}, \quad (2.3)$$

with ε being the gain saturation coefficient. This term is introduced phenomenologically and is specially important at high optical powers, because it represents nonlinear saturations such as the spatial hole burning and the carrier heating. The standing wave produced inside the cavity burns the carriers non-uniformly. The saturation of the gain occurs when the carrier diffusion is not fast enough to fill the holes of carriers left in the active region. On the other hand, carrier heating appears due to the self-heating of the active medium. It moves the excited carriers to higher energy levels that reduce the amount of carriers in the stimulated emission transition.

The linewidth enhancement factor, α , is characteristic of semiconductor lasers and describes the coupling between the amplitude and the phase of the electric field [77]. The refractive index of the active region changes when the carrier number varies. It produces an asymmetric enhancement of the linewidth of the laser, that affects the frequency chirp, and the response under modulation and under the action of an external feedback [78]. α can be modified by changing the relative position between the gain profile and the emission wavelength, as substantial changes in α can be obtained by tuning the emission wavelength far from the maximum gain without changing the gain profile [47, 79].

The field decay rate, k , takes into account the losses of the field inside the cavity. The light generated remains inside the cavity for a time τ_p , which is the time required for the intensity to decay a factor $1/e$ due to the losses of the mirrors. The field decay rate is $k = 1/2\tau_p$ being proportional to $\frac{1}{l} \ln(\frac{1}{R_1 R_2})$ in a Fabry-Perot resonator, where R_1 and R_2 are the reflectivities of the mirrors and l is the length of the cavity. So k can be reduced by increasing the reflectivity of the mirrors but decreased if the cavity length is reduced (which occurs in VCSELs).

The spontaneous carrier recombination rate is given by γ_N . This factor is the sum of the radiative and the non-radiative recombination rates, excluding the contribution from the stimulated recombination process. μ is the pump current normalized such that at threshold $\mu_{th} = 1$.

The amount of light reinjected in the laser is modeled with the feedback strength, κ_{fb} . Due to the finite velocity of the light, the optical field $E(t - \tau)$ is delayed a time τ , with τ being the round trip time of the external cavity in the case of the optical feedback. We are considering only one reflection at the external mirror which is a good approximation in the case of weak and moderate feedback strengths.

The spontaneous emission process is taken into account as a Langevin noise source in $F_E(t)$ as

$$F_E(t) = \sqrt{\beta_{sp} \gamma_N N} \xi(t) \quad (2.4)$$

where β_{sp} is the coefficient of spontaneous emissions, the spontaneous emission rate being $R_{sp} = 4\beta_{sp} \gamma_N N$ (i. e., the fraction of the spontaneously emitted photons that goes into the lasing mode), and $\xi(t)$ is an uncorrelated Gaussian white noise with zero mean and unit variance. Since above the laser threshold the carrier density is clamped, in (2.4) the carrier is often approximated as $N \sim N_0 = 1$ and the noise strength parameter is defined as $D = \beta_{sp} \gamma_N N_0$. $F_N(t)$ is also a Langevin noise source that takes into account the contributions from the spontaneous emission and shot noise to the carrier number. This quantity is usually small and it can be often neglected. From now on we will not consider this term in the equations. With these

simplifications, the model becomes

$$\frac{dE}{dt} = k(1 + i\alpha) \left(\frac{N}{1 + \varepsilon|E|^2} - 1 \right) E + \kappa_{fb} E(t - \tau) e^{-i\omega_0\tau} + \sqrt{D}\xi(t), \quad (2.5)$$

$$\frac{dN}{dt} = \gamma_N \left(\mu - N - \frac{N}{1 + \varepsilon|E|^2} |E|^2 \right). \quad (2.6)$$

The phase of the reinjected field is modified in a quantity $\omega_0\tau$ where ω_0 is the frequency of the solitary laser given by $\omega_0 = 2\pi c/\lambda_0$ (c is the speed of light and λ_0 the wavelength of the solitary laser). Due to the large value of $\omega_0\tau$, even a very small change in the length of the external cavity can induce a large variation in the phase of the optical reinjected field.

2.1.1 Steady state solutions of the Lang-Kobayashi model: the external cavity modes

From a mathematical point of view, the LK model is infinite dimensional due to the time delayed term. The complex dynamics that occurs for a large range of parameters can be highly dimensional and difficult to analyze in a finite dimensional phase space. However, the steady state solutions of the model (called the **external cavity modes**, ECMS) can be found and projected in a 2D phase space $(\Delta\omega\tau, N)$ or in a similar way $(\Delta\omega\tau, |E|^2)$, $\Delta\omega$ being the frequency variation with respect to the solitary laser frequency. The position and stability of the steady state solutions of the model gives important information about the dynamical evolution of the trajectories, however, the high dimensionality of the attractors explains that there are few analytical results.

The steady state solutions can be written as:

$$E(t) = E_s e^{i(\omega_s - \omega_0)t}, \quad (2.7)$$

$$N(t) = N_s. \quad (2.8)$$

Substituting in equations (2.5) and (2.6) we obtain the three equations that deter-

mine the values of E_s , N_s and ω_s

$$\omega_s \tau = \omega_0 \tau - \kappa_{fb} \tau \sqrt{1 + \alpha^2} \sin(\omega_s \tau + \arctan \alpha), \quad (2.9)$$

$$N_s = \frac{1 - (\kappa_{fb}/k) \cos(\omega_s \tau)}{(1 + \varepsilon)} + \frac{\mu \varepsilon}{1 + \varepsilon}, \quad (2.10)$$

$$|E_s|^2 = \frac{\mu - N_s}{N_s - (\mu - N_s) \varepsilon}. \quad (2.11)$$

When $\varepsilon = 0$ the ECMs fall in an ellipse that can be calculated with eqs. (2.9) and (2.10), resulting in

$$((\omega_s - \omega_0) - k\alpha(N_s - 1))^2 + (k(N_s - 1))^2 = \kappa_{fb}^2. \quad (2.12)$$

The solutions can be plotted in the phase space $(\Delta\omega\tau, N)$. The stable points are placed in the lower branch of the ellipse, while the saddle points are in the upper branch of Fig. 2.2. By increasing the feedback strength the ECMs are created in pairs in a saddle-node bifurcation, and the initially stable points lose their stability via a Hopf bifurcation. It has been demonstrated that at least one ECM, called the **maximum gain mode** (MGM), is stable [80]. The MGM is the mode with the highest intensity and the lowest carrier number, but several stable ECMs can exist in the vicinity of the MGM when the feedback strength is increased (Fig. 2.2(b)).

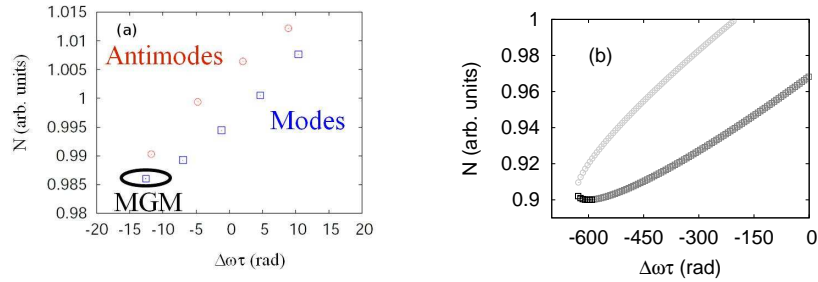


Figure 2.2: (a) Ellipse of steady states in the phase space of the carrier number, N , and the feedback phase, $\Delta\omega\tau$. The saddle points or anti-modes are represented by circles and the initially stable modes by squares. The stable ECMs are placed in the bottom left of the ellipse. The feedback strength is (a) $\kappa_{fb} = 0.3 ns^{-1}$ and (b) $\kappa_{fb} = 30 ns^{-1}$.

Figure 2.3 shows typical trajectories in the vicinity of the attractors for a small value of κ_{fb} in the $(\Delta\omega\tau, N)$ plane. When the initial conditions are chosen in the vicinity of a stable mode, the trajectory falls in the MGM (Fig. 2.3(a)) and remains there indefinitely if the noise strength is small or zero. When the initial conditions are in one of the unstabilized modes, the trajectory is repelled (Fig. 2.3(b)) and after a large enough time, it falls in a stable complex attractor (Fig. 2.3(c)). When the initial conditions are set for a carrier number just below the saddle point the trajectory relaxes back to the MGM.

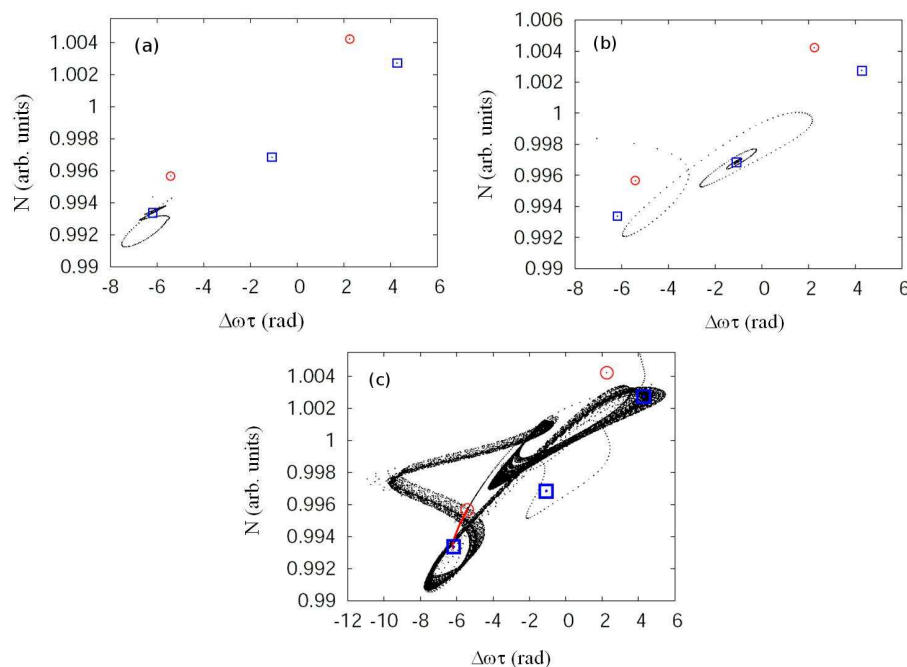


Figure 2.3: Deterministic trajectories (without noise) starting from different initial conditions in the phase space of the carrier number, N , and the feedback phase, $\Delta\omega\tau$. The saddle points or anti-modes are represented by circles and the modes by squares. (a) Trajectory starting in the vicinity of the MGM, (b) starting in the vicinity of an unstable ECM and (c) initial conditions just above an anti-mode produce a global trajectory in the phase space reaching a complex attractor. In (c) a trajectory that starts in the vicinity (just below) of an anti-mode, can reach the MGM.

2.2 SFM Model for a Vertical-Cavity Surface - Emitting Laser

As discussed in Chapter 1, the different characteristics of VCSELs as compared to EELs lead to the consideration of a different model to represent its dynamics. More precisely, the polarization dynamics that is fixed and thus not relevant in EELs is often important and has to be considered in models that describe VCSELs.

One of the most successful models for VCSELs was that proposed in 1995 [72]. This model incorporated the cavity and material properties of the quantum-wells and describes the dynamical properties of the phase of the optical field. It considers the emission of two circular polarized states in a four level model. Radiative recombination of carriers occurs between levels of energy with angular momentum $J_z = -1/2$ to $J_z = -3/2$ that is associated with right circularly polarized light and $J_z = 1/2$ to $J_z = 3/2$ is associated with left circularly polarized light as depicted in Fig. 2.4.

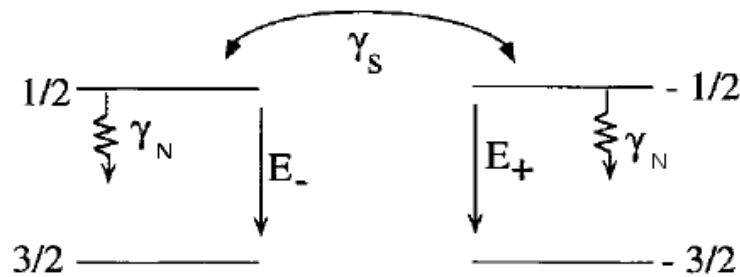


Figure 2.4: Four level model for polarization dynamics in QW VCSELs. Adapted from [73].

The original model in [72] was developed from the Maxwell-Bloch equations that describe the circular polarized optical field variables, associated with the radiative transitions between the four magnetic sublevels of the material, and was reduced

to a simpler form by considering rate equations. In [73] the authors included linear birefringence and dichroism in those rate equations, resulting in the so called **spin-flip model** (SFM). The model is defined in terms of the slowly-varying complex amplitudes, E_+ and E_- , for the orthogonal circular polarizations, the total carrier number, N , and the carrier difference, n

$$\frac{dE_{\pm}}{dt} = k(1 + i\alpha)[(N \pm n - 1)E_{\pm}] - (\gamma_a + i\gamma_p)E_{\mp}, \quad (2.13)$$

$$\frac{dN}{dt} = \gamma_N[\mu - N(1 + |E_+|^2 + |E_-|^2) - n(|E_+|^2 - |E_-|^2)], \quad (2.14)$$

$$\frac{dn}{dt} = -\gamma_s n - \gamma_N[N(|E_+|^2 - |E_-|^2) + n(|E_+|^2 - |E_-|^2)], \quad (2.15)$$

where the variable $N = N_+ + N_-$ represents the total carrier number, given by the sum of the carrier populations with opposite spin in excess of its value at transparency, normalized to the value of that excess at the lasing threshold. Here, n is defined as $n = N_+ - N_-$, which takes into account the difference of the carrier numbers of the two magnetic sublevels, and it is normalized in the same way as N . As discussed in Chapter 1, VCSELs usually emit one of two orthogonal linear polarizations due to the effect of linear anisotropies, so it is more convenient to rewrite the above equations in terms of the orthogonal linearly polarized optical fields. The projection of the circular polarized states over the linearly polarized states is given by:

$$E_x = \frac{E_+ + E_-}{\sqrt{2}}, \quad E_y = -i\frac{E_+ - E_-}{\sqrt{2}} \quad (2.16)$$

Thus, by substituting eq. (2.16) in the equations (2.13)-(2.15) we obtain the SFM equations in terms of the orthogonal linearly polarized slowly-varying complex amplitudes, E_x and E_y , the total carrier number, N , and the carrier difference, n [73]:

$$\begin{aligned} \frac{dE_{x,y}}{dt} &= k(1 + i\alpha)[(N - 1)E_{x,y} \pm inE_{y,x}] \mp (\gamma_a + i\gamma_p)E_{x,y} \\ &\quad + \sqrt{\beta_{sp}\gamma_N N}\xi_{x,y}, \end{aligned} \quad (2.17)$$

$$\frac{dN}{dt} = \gamma_N[\mu - N(1 + |E_x|^2 + |E_y|^2) - in(E_y E_x^* - E_x E_y^*)], \quad (2.18)$$

$$\frac{dn}{dt} = -\gamma_s n - \gamma_N[n(|E_x|^2 + |E_y|^2) + in(E_y E_x^* - E_x E_y^*)]. \quad (2.19)$$

The field decay rate, k , the linewidth enhancement factor, α , and the decay rate of the total carrier population, γ_N , have the same meaning as in the LK model (Sec. 2.1). μ is the injection current parameter, normalized such that the static cw threshold in the absence of anisotropies is at $\mu_{th,s} = 1$.

To characterize the mixing of populations with different spin, this model introduces the spin-flip rate γ_s as a phenomenological parameter. From the point of view of the origin of the parameter, the recombination of the carrier populations in the magnetic sublevels involves a large variety of processes such as scattering by defects and exchange interactions between electron-hole or exciton-exciton [63]. It is worth remarking that γ_s acts as a coupling between the two populations of carriers in each pair of levels. For a very slow mixing (i. e. $\gamma_s = \gamma_N$) equations (2.17)-(2.19) are decoupled in two sets of independent equations, one for E_+ , N_+ and another for E_- , N_- . In the limit of $\gamma_s \rightarrow \infty$, corresponding to an instantaneous mixing between the two populations, the orthogonal polarizations become independent of n and coupled through the same population N .

The anisotropies in the cavity are represented by the parameters γ_a and γ_p . The frequency splitting of the linearly polarized modes is modeled with the birefringence γ_p . Its value corresponds to the frequency detuning above and below a central frequency, so the frequency difference between the two modes x and y is given by $2\gamma_p$. γ_a is the dichroism that takes into account different gains for the polarization modes of the cavity, the asymmetric position of the modes in the gain-frequency curve and different asymmetric geometries of the cavity [63]. This parameter can be positive or negative depending on which mode has a larger gain-to-loss ratio.

As in the LK model, β_{sp} is the coefficient of spontaneous emission, and $\xi_{x,y}$ are uncorrelated Gaussian white noises with zero mean and unit variance.

VCSELs can be very different depending on their characteristics and can show a relatively large dispersion on their characteristic parameters. We show in Table 2.1 a range of values for typical VCSELs [81].

Table 2.1: Typical VCSEL parameters and values used in this thesis.

Parameter	Symbol	Range of values	Values used
Linewidth enhancement factor	α	2 to 5	3
Field decay rate	k	100 to 400 ns ⁻¹	300 ns ⁻¹
Total carrier decay rate	γ_N	0.5 to 2 ns ⁻¹	1 ns ⁻¹
Spin-flip rate	γ_s	1 ns ⁻¹ to 100 ns ⁻¹	50 ns ⁻¹
Amplitude anisotropy	γ_a	>-1 ns ⁻¹ to <1 ns ⁻¹	0.5 ns ⁻¹
Phase anisotropy	γ_p	1 to 150 ns ⁻¹	50 ns ⁻¹
Noise strength	D	10 ⁻⁶ ns ⁻¹ to 10 ⁻³ ns ⁻¹	10 ⁻⁶ ns ⁻¹

2.2.1 Steady state solutions of the SFM model

Different states of polarization can be found for different parameters of the model. Here we analyze two paradigmatic scenarios characterized by the positive or negative values of γ_a .

We can define the steady state solution for the orthogonal linear polarizations as

$$E_{x,y} = Q_{x,y} e^{i(\omega_{x,y}t + \Psi_{x,y}) + i\theta}, \quad N = N_0, \quad n = n_0 \quad (2.20)$$

where θ is an arbitrary phase that can be set to zero without loss of generality and Ψ is a relative phase between the polarizations.

By substituting eqs. (2.20) in (2.17)-(2.19) we obtain the solutions for the x

polarization

$$Q_x = \sqrt{\frac{1}{2} \frac{\mu - N_0}{N_0}}, \quad (2.21)$$

$$\omega_x = -\gamma_p + \gamma_a \alpha, \quad \Psi_x = 0, \quad (2.22)$$

$$N_{0,x} = 1 + \frac{\gamma_a}{k}, \quad n_0 = 0, \quad (2.23)$$

and for the y polarization is given by

$$Q_y = \sqrt{\frac{1}{2} \frac{\mu - N_0}{N_0}}, \quad (2.24)$$

$$\omega_y = \gamma_p - \gamma_a \alpha, \quad \Psi_y = 0, \quad (2.25)$$

$$N_{0,y} = 1 - \frac{\gamma_a}{k}, \quad n_0 = 0. \quad (2.26)$$

Analyzing these solutions we can observe that the amplitude anisotropy gives slightly different thresholds for the x and y polarizations. The mode with smaller threshold is selected at low pump currents, in such a way that for positive γ_a , the y mode turns on. When $\gamma_a < 0$ the lower threshold is for the x mode and this is the mode that will be emitted close to threshold. A detailed scenario can be obtained by calculating the boundary of stability for each polarization. The stability of the x and y polarizations, as obtained from a linear stability analysis of Eqs. (2.13)-(2.15) is shown in Fig. 2.5. Three regions of stability can be identified in Fig. 2.5: only the polarization x is stable, only the polarization y is stable or both polarizations are stable. A fourth region emerges outside the stability boundaries where neither x or y are stable and their intensities oscillate in time. In the bistable region both polarizations are stable and one of the two polarizations can be emitted depending on the initial conditions. Elliptically polarized steady-state solutions also exist.

An example of this bistable behavior can be found in the case of $\gamma_a > 0$ and $\gamma_p = 50ns^{-1}$ (Fig. 2.5(a), vertical line). When μ is set just above threshold the y polarization is slightly favored by its greatest gain and becomes stable to the detriment of the x . By further increasing μ , and around $\mu = 1.12$, the x polarization becomes stable but the VCSEL will keep emitting the y polarization. At $\mu \sim 1.16$,

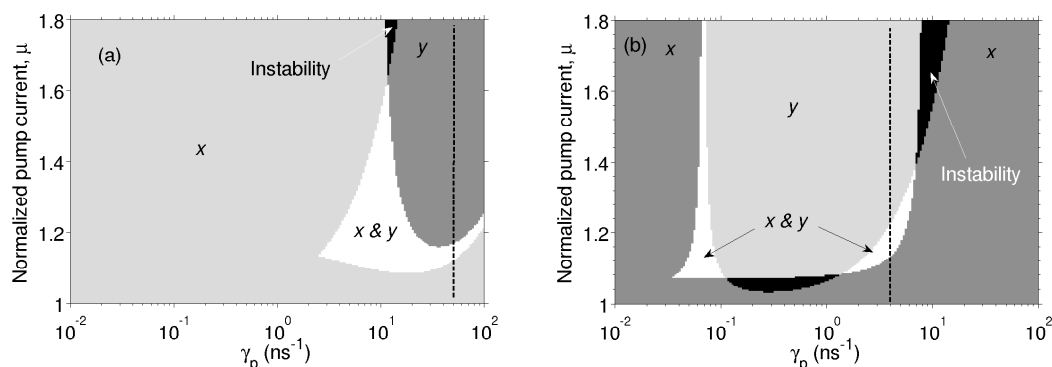


Figure 2.5: Polarization stability diagram in the parameter space (γ_p, μ) for (a) $\gamma_a = 0.5$ ns⁻¹ and (b) $\gamma_a = -0.2$ ns⁻¹. The vertical dashed line shows a change of stability crossing a bistable region.

the y polarization becomes unstable and the polarization turns to the x direction. At this point, if μ is decreased, the x mode will be on until its stability boundary (at $\mu = 1.12$). This hysteresis is the footprint of bistability. A similar behavior exchanging x 's and y 's can be seen in Fig. 2.5(b) if we consider $\gamma_a < 0$ and $\gamma_p = 4$ ns⁻¹.

The SFM model above described is a combination of phenomenological and detailed theoretical analysis of the light-matter interactions in VCSELs. However, the model has certain limitations that have to be considered. Several approximations have been made to obtain the model equations.

A first simplification is to consider that the dipole polarizations have a much faster relaxation rate than the other characteristic time scales of the system and can be adiabatically eliminated. Furthermore, we use the simplest version of the SFM model that does not take into account the transverse modes of the emitted light, thus we restrict our analysis to low pump currents not very far from the threshold, where the fundamental transverse mode dominates. The model also neglects the thermal effects in the carriers and gain. Finally, the amplitude and phase anisotropies are considered

parallels, i.e. in the same x and y axis, for simplicity, thus the contribution of both parameters can be expressed, in the model, as a function of the same polarization.

Chapter 3

Nonlinear and stochastic dynamics of semiconductor lasers

Semiconductor lasers have many important applications, and their study is important to improve the performance and characteristics of the next generation of SCLs. However, there is another important motivation for the study of these devices. Semiconductor lasers display a large variety of nonlinear dynamics also present in other nonlinear systems. Excitability [82, 83, 84], bistability [65, 66], low frequency fluctuations [85, 86], chaos [87] and nontrivial synchronization phenomena [88, 90, 91, 92] are some examples.

Due to the fact that these dynamics can be observed and controlled experimentally, semiconductor lasers are good devices for improving our understanding of the origin of these dynamics. In this chapter we will consider dynamics induced by modulating the injection current of the laser in section 3.1, by an external reflector in section 3.2 and by spontaneous emission noise in section 3.3. Finally, the dynamics of coupled lasers will be discussed in the framework of synchronization of networks of nonlinear oscillators in section 3.4, by focusing in two types of synchronizations transitions: the crowd synchrony and the quorum sensing.

3.1 Effects of the current sweep across a bifurcation point

In nonlinear systems, when a control parameter is varied in time and is swept across a bifurcation point, the phenomenon of **critical slowing down** occurs near the bifurcation point and results in dynamical hysteresis [93]. In semiconductor lasers this phenomenon has been demonstrated experimentally near a bifurcation, such as the laser threshold, and it produces a delay in the laser turn-on, as shown in Fig. 3.1. This delay depends on the pump current sweep rate and on the noise strength, among other parameters [93, 94, 95].

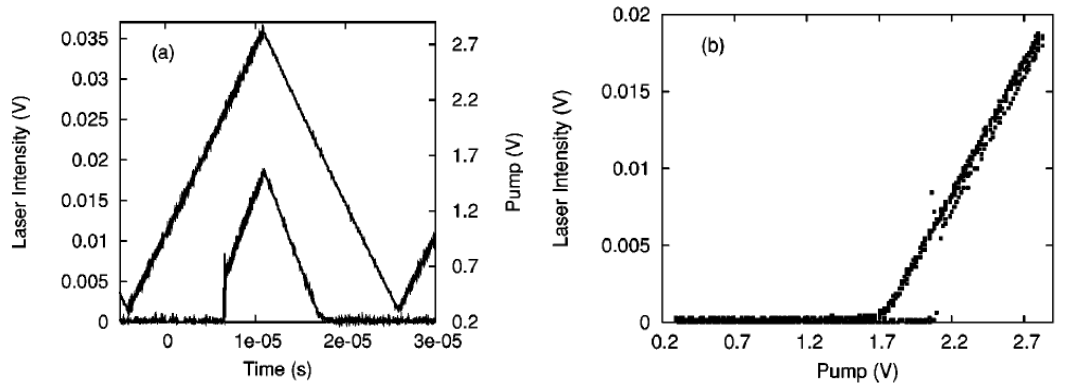


Figure 3.1: (a) Laser intensity and pump voltage as a function of time when a triangle wave of frequency 40 kHz is applied by the function generator. The laser switches on at a voltage V^* larger than the static threshold at $V_{th} = 1.78$, while the turn-off occurs at $V \approx V_{th}$ for decreasing pump. (b) A plot of the laser intensity as a function of pump voltage shows bistability in the interval $V_{th} < V < V^*$. The time traces, plotted with points to better highlight the effect, are slightly separated on the diagonal branch: the lower occurs for increasing pump, the higher for decreasing pump because of the speed at which the laser is driven. From [94].

The quasi-static intensity-current response is obtained with a very slow increase of the pump current, as that shown in Fig. 3.2(a), and is a good representation of the

polarization response of a VCSEL when the injection current variation is slower than the longest time scale of the laser. Figure 3.2(a) is as the static intensity-current obtained by increasing the pump current in small steps after the stationary state is reached. However, the stability scenario shown in Fig. 3.2(a) changes drastically when the injection current variation is not slow or quasi-adiabatic, as compared to the laser characteristic time-scales, and fails to describe the laser polarization with faster modulation.

The influence of current modulation near the laser threshold and PS points can be investigated numerically by simulating the SFM rate equations [96]. Figure 3.2(b) shows the polarization intensities vs. the pump current, when the current varies between $\mu_i = 0.95$ and $\mu_f = 1.4$ in 25 ns [note that in Fig. 3.2(a) the current varies between the same extreme values but in 40 μ s]. By comparing both figures one can observe that, with a faster current modulation:

- (i) The threshold is delayed to a higher current value, i.e., the dynamic lasing threshold is larger than the static one, $\mu_{s,th} = 1$ in the absence of anisotropies.
- (ii) The laser turns on with relaxation oscillations leading to pulses of intensity that relax to the dynamical stable state.
- (iii) The PS for increasing current is delayed to a higher current value.
- (iv) The PS for decreasing current is delayed to a lower current value and can even disappear (in Fig. 3.2(b) one can notice that the x polarization remains on until the laser turns off).
- (v) As a consequence of (iii) and (iv), the size of the bistability region increases, as compared to that predicted by both, the linear stability analysis and the simulations with quasi-static current variation.

The above-described phenomena near the polarization switching points, have been demonstrated experimentally in directly modulated VCSELs [97].

The multiple applications of VCSELs in optical communications have prompted

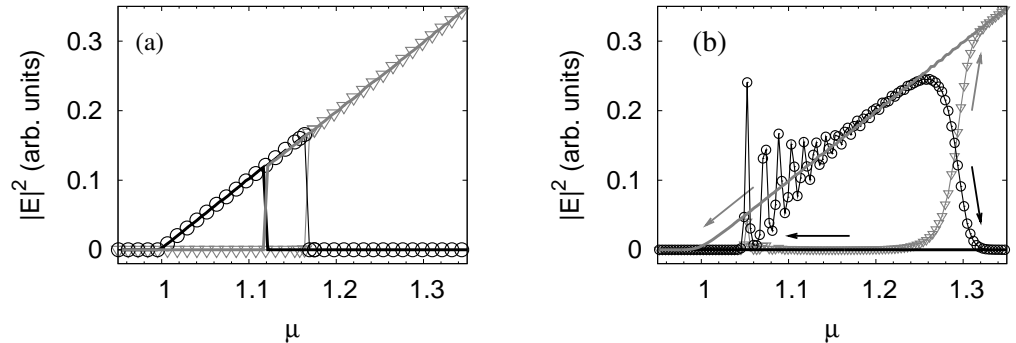


Figure 3.2: (a) Intensities of the x and y polarizations when the injection current increases and decreases linearly, from $\mu_0 = 0.95$ to $\mu_f = 1.4$ in $40 \mu s$. x polarization in gray for increasing (∇) and decreasing (gray solid line) current; y polarization in black for increasing (\circ) and decreasing (black solid line) current. (b) As panel (a), but the current varies from $\mu_0 = 0.95$ to $\mu_f = 1.4$ in $25 ns$. Other model parameters are shown in Table 2.1.

a large interest in the study of the response of these devices to current modulation. A signal of period equal to the period of the modulation can be transmitted and encoded as a logic signal in bits of high and low intensities. For this purpose, is necessary to use a laser that is capable of responding at high modulation frequencies.

VCSELs can be directly modulated at high speeds and a lot of effort has focused on achieving a wide small-signal modulation bandwidth. Under large amplitude current modulation, nonlinear effects arise (such as period doubling, chaos, multistability, etc. [98, 99, 100, 101]). In VCSELs, the polarization and transverse-mode competition greatly enhance the complexity of the nonlinear dynamics [102, 103, 104, 105, 106].

3.2 Optical feedback induced dynamics

When the light of a semiconductor laser is reflected in an external mirror and reinjected into the laser it may produce a destabilization of the laser output that is not

suitable for many applications. Even a small amount of reinjected light can induce large fluctuations in the intensity and a broad optical spectrum. This is the case of weak optical feedback. Especially sensitive to this feedback are the EELs, due to the relatively low reflectivity of their internal cavity mirrors. However, most of the dynamics observed in EELs can also be observed in other SCLs such as VCSELs [107]. In this section, we will analyze the influence of optical feedback from an external cavity in the dynamics of an EEL.

One of the important characteristics of a laser with feedback is related with the current-intensity curve (Fig. 3.3). The threshold condition can be determined from Eqs. (2.10) and (2.11) by imposing $|E_s|^2 = 0$. From this condition one can see that the optical feedback reduces the threshold current in a factor that is proportional to the feedback strength, κ_{fb} . By increasing the pump current in small steps, the laser with feedback turns on at a μ_{th}^{fb} smaller than the solitary laser threshold (i.e. without feedback) at $\mu_{th}^{sol} = 1$ and the intensity increases linearly with the pump current, as seen in Fig 3.3.

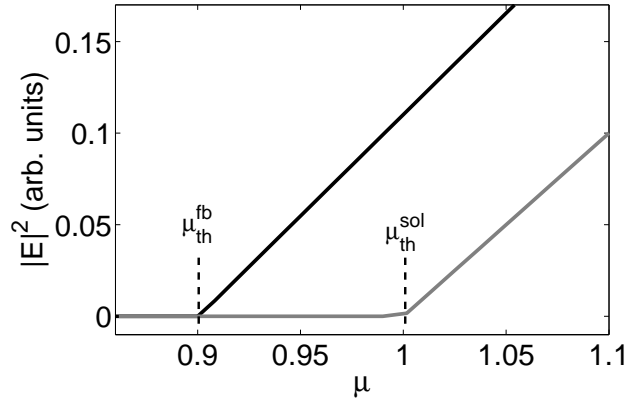


Figure 3.3: Intensity-current response of a solitary EEL (gray line) and of a EEL with optical feedback (black line). $\kappa_{fb}=30 \text{ ns}^{-1}$ and $k=300 \text{ ns}^{-1}$.

A rich variety of nonlinear dynamics appears when the different model parameters are varied. A simple classification can be done according to the behavior of

the output intensity that distinguish three domains (Fig. 3.4(a)): the steady-state regime, the low frequency fluctuations regime and the coherence collapse regime.

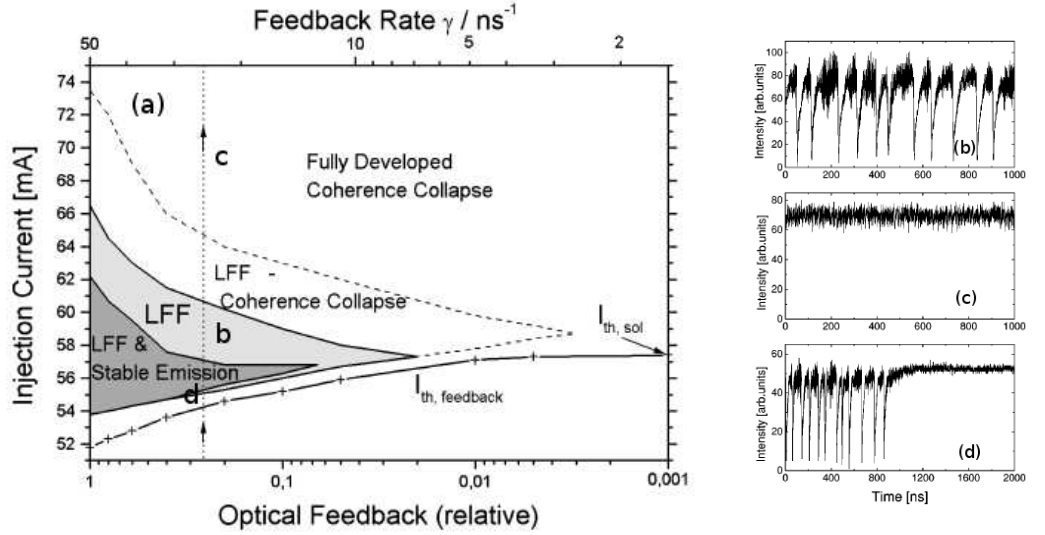


Figure 3.4: Dynamical regimes of a SCL with optical feedback. (a) Boundaries of the regimes in the injection vs. current-feedback strength phase space. Adapted from [47]. The time traces for the regimes labeled as b, c and d correspond to the panels (b), (c) and (d) respectively. (b), (c) and (d) Intensity time traces for the regimes of LFFs, coherence collapse and coexistence of stable emission and LFFs respectively. Adapted from [108].

For injection currents close to the threshold, the laser output becomes unstable and shows large fluctuations in the intensity and phase. A fast pulsed dynamics occurs in the range of ps with an irregular amplitude modulated by a slow envelope in the range of hundreds of ns [85]. In fact, experimental limitations in the time resolution may filter the fast dynamics and only the slow envelope can be observed. This slow envelope exhibits the so called **low frequency fluctuations** (LFFs). The LFFs are characterized by sudden dropouts of intensity followed by a slow recovery process, after which the intensity reaches a nearly constant value and remains there for a certain time before the occurrence of a new dropout (Fig. 3.4(b)).

The **coherence collapse** regime occurs for large enough pump currents and mod-

erate feedbacks [42, 83, 109] (Fig. 3.4(c)). In this regime, the relaxation oscillations are excited by the feedback and a chaotic dynamics of high dimensionality emerges. The high number of ECMs involved in this regime produces an enlargement of the linewidth that can be of the order of GHz, and the intensity fluctuations become completely irregular. When the relaxation oscillation frequency matches the external cavity resonance, a period doubling route to chaos can be found by increasing the feedback strength [110] while, when this condition is not satisfied, a quasiperiodic route to chaos can be observed [111, 112].

For low pump currents close to the threshold and moderate feedback strength, the stable steady-state regime can be observed, in a large range of parameters, alternated with periods of LFFs (Fig. 3.4(d)). In this regime called **coexistence regime**, groups of LFFs containing up to thousands of dropouts occur, followed by regions of constant intensity. When the trajectory in phase space reaches one of the stable ECMs, in the absence of noise or in the presence of a small amount of noise, the system remains there indefinitely, leading to noisy cw emission with a very narrow linewidth. A large enough perturbation, e.g. a fluctuation induced by noise, can induce escapes from the fixed-point attractor after which a new set of LFFs occurs. The probability of escape from the stable ECM has been described in terms of the Kramers problem in a potential well [107]. In these regimes both dynamics alternate in a coexistence between the stable emission and LFFs (Fig. 3.4(d)). The process by which the cw emission is reached is not fully understood yet and suggests the transient nature of the LFFs which has been observed numerically in the LK model [107].

The low frequency fluctuations regime in SCLs (Fig. 3.5(a)) was observed experimentally for the first time in 1977 [44], and progressively attracted attention. Different explanations have been proposed for the nature of the LFFs involving stochastic and deterministic processes. A first explanation was given by Henry and Kazarinov [113]. The authors used a potential well model where the laser leaves the steady state due to the spontaneous emission noise, and the system describes a

trajectory in the phase space by remaining in successive minima of potential wells. A generalization of this framework was published in [45] by introducing a multimode traveling wave model driven by noise that can be understood as a bistable system with a MGM and a temporally stable mode with lower intensity. In this model, even without noise, the authors observed LFFs and suggested the existence of a chaotic attractor as a mechanism for LFFs. The existence of a chaotic attractor was experimentally confirmed and interpreted as a time-inverted type II intermittency [114]. Another description of LFFs was proposed by Sano [115] based on the analysis of the deterministic LK model in the phase space of $(\Delta\omega\tau, N)$. According to this description, the trajectory in the phase space follows the locally chaotic attractors (around the **modes**, see Fig. 2.2(a)), drifting from a low-gain mode (low intensity) to a higher-gain mode (higher intensity), as depicted in Fig. 3.5 (label 1). The high gain modes are closer to the saddle-points (**anti-modes**), which increases the probability that the trajectory collides with one of the saddle-points (label 2). After the collision, the trajectory is repelled towards the lower gain modes (label 3) when the power dropout occurs and the process starts again. Subsequent experimental observations showed evidences of the stochastic nature for the initiation of dropout events by comparing the results obtained in a semiconductor laser with optical feedback with the escape of a Brownian particle from a metastable state [116].

A commonly used measure to characterize the statistical properties of the LFFs is the time interval between consecutive dropouts, T . Figure 3.6 shows typical probability distribution functions of the inter-dropout intervals obtained experimentally (Fig. 3.6 (a)) and numerically by integrating the LK model (Fig. 3.6 (b)).

Sukow *et al.* [117] studied the effect of the pump current in the inter-dropout average time and found a refractory time just after the dropout with a zero probability for the occurrence of a new event. They related this with the recovering of the intensity after the dropout. Depending on which parameter is changed, the inter-dropout time varies in a different way (Fig. 3.7). In particular, the average of the inter-dropout time, $\langle T \rangle$, decreases for increasing the injection current [117, 118] (Fig.

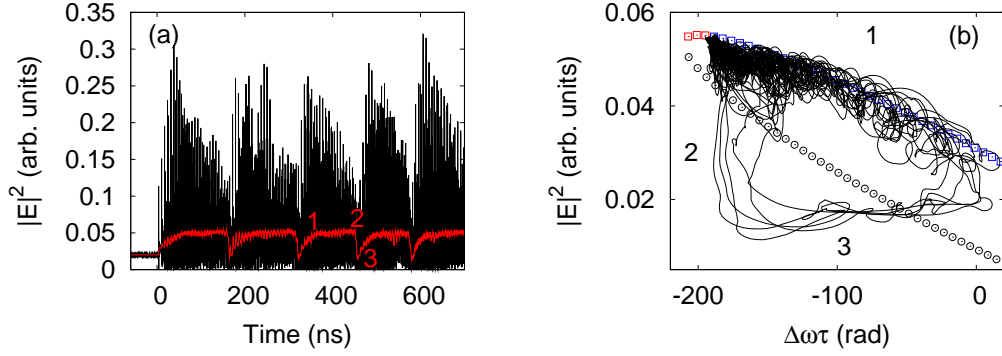


Figure 3.5: (a) Time trace of the laser intensity in the low frequency fluctuation regime. The fast picosecond dynamics (black line) has been filtered out at 120 kHz (red line). The laser is initially in the solitary steady state and at time $t=0$ the optical feedback is turned on. (b) The filtered time trace in the phase space $(\Delta\omega\tau, |E|^2)$. The squares and circles show the modes and the anti-modes respectively.

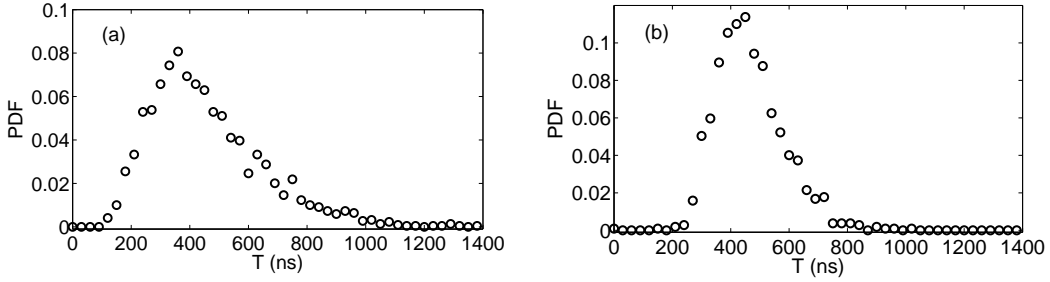


Figure 3.6: (a) Probability distribution function (PDF) of time between consecutive dropouts, T . Figure courtesy of J. Tiana-Alsina. (a) PDF obtained experimentally and (b) PDF obtained by integrating the LK model. The parameters used are: $\tau = 6$ ns, $\mu = 0.95$, $\kappa_{fb} = 30$ ns $^{-1}$, $\alpha = 5$, $\varepsilon = 0.07$, $\gamma_N = 1$ ns $^{-1}$, $k = 300$ ns $^{-1}$ and $D = 10^{-8}$ ns $^{-1}$.

3.7(a)). When the time delay is increased, $\langle T \rangle$ increases monotonically [119, 120] (Fig. 3.7(b)) which also occurs for increasing the feedback strength [118, 120] (Fig. 3.7(c)).

A good agreement between the model and experiments was found by including a noise in the LK model [83, 121, 122]. A novel interpretation of LFFs was reported

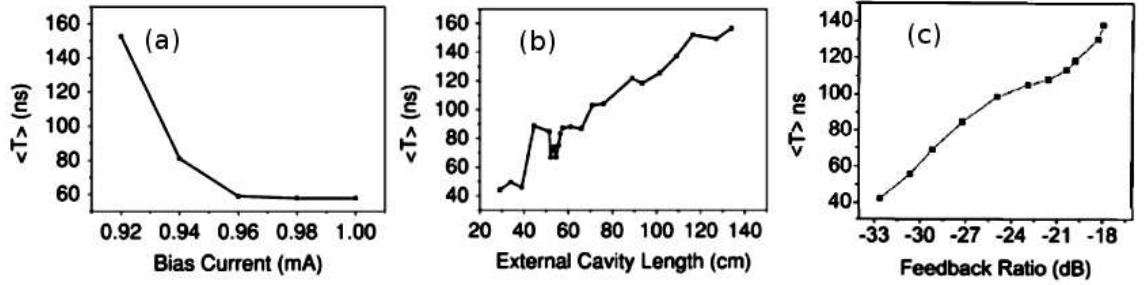


Figure 3.7: Averaged inter-dropout time as a function of (a) the bias current, (b) external cavity length and (c) the feedback ratio. (a) and (b) are adapted from [120] and (c) from [118].

experimentally and numerically in [123], based on the deterministic LK model, where the laser behaves as a deterministic chaotic self-excitable system.

Actually, the LK model has succeeded in the description of the LFF regime even in multi-mode lasers where the dynamics of total intensity is very similar to that of a single model laser. However, the interactions between modes require a generalization of the LK model and a discussion of the multimode extensions of the LK model is out of the scope of this thesis.

In some parameter regions, the LFFs show excitability [82, 83]. In these regions, a different model for the LFFs was proposed by Eguia, Mindlin and Giudici [124]. The authors considered a phenomenological model (the EMG model from now on) in which, after an Andronov bifurcation, a pair of fixed points (a node and a saddle) is created. The unstable manifolds of the saddle, S , are the stable manifolds of the node, N , as depicted in Fig. 3.8. The third fixed point is a repeller, R , inside the heteroclinic orbit with the unstable manifold being one of the stable manifold of the saddle.

An appropriate amount of noise produces escapes from the stable node and, eventually, the system can reach the unstable manifold of the saddle, describing a long excursion in the phase space. Due to the proximity between the stable manifolds

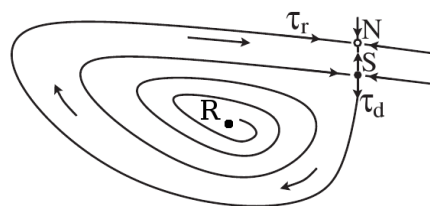


Figure 3.8: Schematic representation of the fixed points and manifolds describing phenomenologically the LFFs as proposed in [124]. Adapted from [127].

of the saddle and the node, the system can describe some oscillations around the repeller before falling into the node. Yacomotti *et al.* [125] associated the two parameters of the model to the bias current and the feedback strength, obtaining a good agreement in the distribution of the inter-dropout intervals, between the model and experiments. In 2005, Méndez *et al.* found that the excitable behavior in LFFs is present only in a subset of the region where LFFs can be observed [126] and, more recently [127], the existence of coarse grained variables, that describes the LFFs, was discussed in terms of the phase space of the EMG model. A similar trajectory in the phase space of the intensity and its derivative was also obtained experimentally and numerically, with the LK model.

3.3 Noise induced dynamics

Usually considered as a drawback, noise is present in many systems in nature, perturbing their evolution. The interaction of the system with different external factors not considered in the deterministic model may produce fluctuations difficult or even impossible to predict. The (large) number of degrees of freedom that describe these fluctuations, from e.g. a thermal bath, can be considered as noise. Thus, an intrinsic deterministic dynamics of the system becomes modified by stochastic fluctuations of the parameters or variables of the systems that can sometimes produce counter-

intuitive effects.

Semiconductor lasers have a main source of noise that comes from the **spontaneous emission** process. It occurs when an excited carrier decays spontaneously to a lower energy level emitting a photon. Those photons are emitted randomly in direction and phase, unlike what occurs with stimulated emission, where the emitted photons have the same direction and phase. The spontaneous emission rate is strongly influenced by the temperature of the device and the energy of the band gap and, in semiconductor lasers, is not negligible when working at room temperature [41]. It was demonstrated [128] that the effect of spontaneous emission in a semiconductor laser can be simulated numerically by using non-correlated Gaussian white noise terms added to the rate-equations for the real and imaginary parts of the complex electric field.

Spontaneous emission noise is not only present in the optical field but also in the carrier recombination. The consideration of the noise term in the equations for the optical field implies also a noise term in the carrier equation. Furthermore, small fluctuations in the electronics that control the pump current of the laser could also be considered as a noise term in the injection current. However, the carrier and current noise sources are, in general, small enough to be neglected, despite some dynamics can not be explained without the influence of carrier noise [129].

From the dynamical point of view, the spontaneous emission in SCLs induce perturbations that can trigger escapes from the stable steady states. In the case of a solitary laser after the perturbation the system returns to the fixed point describing relaxation oscillations around it.

Noise can often help a nonlinear system to find a new stable stationary solution. In many systems, when a control parameter is varied continuously, either periodically or not, across a bifurcation point, critical slowing down occurs as explained in section 3.1, for which the system remains in the initial state even above the static bifurcation point. Noise can help the system to reach the new stable state anticipating the

parameter value at which the dynamical transition occurs.

In semiconductor lasers with optical feedback, in certain parameter regions, noise can also induce important differences in the chaotic itinerancy organizing the dynamics, in such a way that the noise reduces the fluctuations of the trajectory around the ECMs and increases the time to collide with an anti-mode, i.e. increasing the inter-dropout time [122].

3.3.1 Stochastic dynamics in multi-mode semiconductor lasers

Nonlinear systems often display multi-stability, i.e., several stable attractors can coexist in the phase space and a large enough perturbation can induce jumps from one attractor to another. This is the case of a particle in a bistable system, such as a double well potential, under the influence of Gaussian white noise. The probability of transition from one well to the other decreases with the height of the potential and increases with the noise strength. The transition rate is given by the Kramers rate, $R_k \propto e^{-\Delta V/D}$ being ΔV the height of the potential barrier and D the noise strength [130].

As discussed in sections 1.3 and 3.1, VCSELs show bistability in the polarization of the electric field for an appropriate range of pump currents. Near the polarization switching (PS) points, stochastic, i.e. noise-induced, switching can also occur. It has been shown that, in spite of the potentially complicated polarization dynamics, key features of the PS (such as the distribution of residence times in each polarization state) can be well understood as stochastic hopping in an effective 1D double-well potential as shown in Fig. 3.9 [65, 66].

Time traces for three different pump currents are shown in Fig. 3.10(a)-(c) and the **effective potential** associated to the polarization switching scenario is displayed schematically in Fig. 3.10(d). In the low current region, labeled I, the laser can only emit the y polarization, which is represented as an effective potential with only one

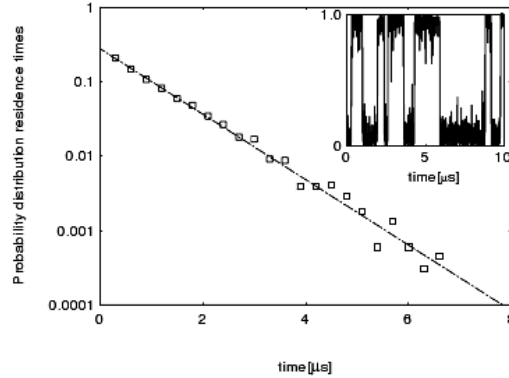


Figure 3.9: Experimental distribution of residence times of polarization switching in a VCSEL for a pump current that shows polarization bistability. The dashed dotted line shows an exponential fit. The inset shows part of the time trace used to calculate the distribution. From [65].

well. A typical time-trace of the two polarizations is shown in Fig. 3.10(a). For increasing pump there is a region of pump current values, labeled II, where there is bistability and a small probability of emission of the x polarization. The effective potential is a double-well potential, with a small right well. In this region of pump current values, if the laser emits the x polarization, a weak perturbation or a small amount of noise has a large probability to trigger a PS to the y polarization. On the contrary, if the laser emits the y polarization, there is only a small probability that a fluctuation will trigger a PS. As the pump increases the switching probabilities vary (Fig. 3.10(b)) and at the right boundary of the bistable region, label III, the most probable polarization is the x polarization. If the laser emits the y polarization, a weak perturbation or a small amount of noise can trigger a switch to the x polarization. In this region the effective potential is the double-well potential which has a small left well. Finally, for high pump current (region label IV), the laser emits the x polarization and the effective potential has only one well (Fig. 3.10(c)).

A periodic modulation of the pump current can periodically modify the stability of

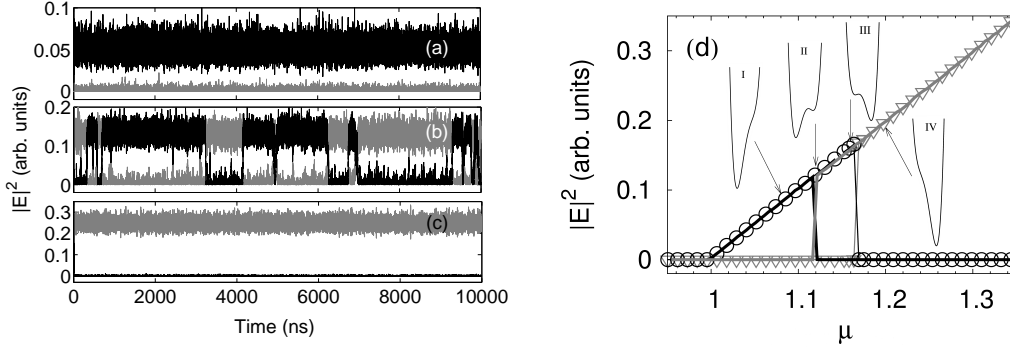


Figure 3.10: (a) Time trace for the x (gray) and y (black) polarizations for a pump current $\mu = 1.05$, (b) $\mu = 1.14$ and (c) $\mu = 1.25$. The noise strength is $D = 10^{-3}\text{ns}^{-1}$. (d) Averaged intensities of the x and y polarizations when the injection current increases and decreases linearly, from $\mu_0 = 0.95$ to $\mu_f = 1.4$ in $40 \mu\text{s}$. x polarization in gray for increasing (∇) and decreasing (gray solid line) current; y polarization in black for increasing (\circ) and decreasing (black solid line) current. The black curves are schematic representations of the effective one-dimensional potential at four pump current values, corresponding to labels I to IV. The noise strength is $D = 10^{-6}\text{ns}^{-1}$.

the above described potential wells. When an appropriate amount of noise is added to the system, the switching between one well to the other becomes synchronous with the modulation leading to the **stochastic resonance** effect (SR). The SR occurs when a nonlinear system amplifies a small periodic signal under the influence of an appropriate amount of noise [131]. This concept, first introduced as a possible explanation for the ice ages [132, 133], has been observed in a large variety of systems such as electronic circuits [134], bistable ring lasers [135], neuronal systems [136], in the inter-dropout time in SCL with optical feedback [137, 138] and in the PS in VCSELs [139, 140]. Different mechanisms for SR have been reported (see [131] and [141] for reviews).

However, it is not necessary a periodic modulation to observe an optimal response of the nonlinear system under the right amount of noise. In general, the SR can be characterized by the synchronous response between a weak input and the output of

the system when the desired output is not obtained without noise. This is the case of a new type of SR reported by Murali *et al.* in 2009 [142] in the framework of digital signal processing. Considering the relatively high level of noise that affects the small electronic devices, the authors proposed and demonstrated the reliability of a bistable electronic system acting as a logic gate under the influence of the right amount of noise, leading to the so called logic stochastic resonance that will be studied in more detail in Chapter 5.

3.4 Synchronization of nonlinear oscillators

Synchronization is a phenomenon that appears frequently in neuronal systems or networks, interacting cells and, from a more general point of view, in coupled oscillators [143, 144]. Synchronization is a general concept that can be summarized as an adjustment of rhythms of oscillating elements due to their interactions. Various forms of synchronization have been described such as identical synchronization, phase synchronization, lag synchronization, and generalized synchronization. This dynamics was described for the first time by Huygens in the XVII century when he observed that two pendulum clocks with slightly different periods hanged on the same beam synchronized [145]. Early examples of synchronization in natural systems with a large number of elements are found in swarms of bioluminescent insects as the glowworms or the fireflies that glow periodically at the unison despite the fact that their natural frequencies, without external stimulus, are different [146]. Another example, maybe more familiar to all of us, is the case of an applauding audience where we can hear a transition from noise (each person applauding at different rhythm and phase) to rhythmic or synchronously applause.

3.4.1 Synchronization phenomena in semiconductor lasers

One of the most intuitive and simple way to synchronize an ensemble of oscillators is by using a common driving signal. When a number of independent oscillators are influenced by the same external forcing, in a unidirectional coupling scheme, synchronization of all or almost all the oscillators will arise for large enough coupling strength. Synchronization can be achieved under the influence of a deterministic forcing but also under a stochastic one [144]. The driving signal determines the characteristics and dynamics of the synchronized elements which results in a transmitter-receiver configuration and can produce a rich variety of bifurcations and dynamics [147].

A practical application of synchronization by a common external signal can be found in the synchronization of a semiconductor laser array [148, 149]. SCLs can be manufactured in arrays of tens of lasers each of them emitting a small output power. Typically, the optical field of each laser is slightly different from the others due to inhomogeneities in the manufacturing process and because the phase of the electric field is randomly modified by spontaneous emission. Therefore, the laser array produces an output that is the sum of the output of each laser. Synchronization via an external signal, e.g. when they are injected by an external laser as schematically shown in Fig. 3.11(a), can be used to obtain large intensities with low power devices. An external single mode laser was used in [150] as a master laser to inject light on each laser of an array. This mechanism, known as injection locking, allowed obtaining outputs of 105 mW in the far-field beam at a single frequency with an array of 10 EELs of 3 mW each. Notice that this output is larger than the direct sum of the individual powers of the lasers of the array, since interference occurs in the electric field and the power depends on the square of the sum of electric fields.

The synchronization of a large number of uncoupled EELs (schematically represented by units 1 and 3 in Fig. 3.11(a)) driven by a common noise source (unit 2 in Fig. 3.11(a)), that can be obtained for example from the incoherent light emitted

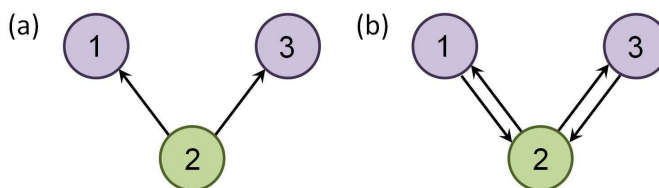


Figure 3.11: Schematic representation of unidirectional and bidirectional coupling schemes. (a) Unidirectional coupling where the laser 2 drives the lasers 1 and 3. (b) Bidirectional coupling in a chain of lasers. 1 and 3 are not directly coupled, thus they are coupled through 2.

by a laser pumped below threshold, is also possible and was theoretically studied in [151]. The author reported a synchronization transition, by increasing the coupling strength, when the α parameter is equal to zero. When a non-zero α factor is considered in the equations, there is a significant loss of synchronization for intermediate coupling strengths and for stronger external forcing a revival of synchronization was observed. This was described in terms of the destabilization of the synchronous solution via a stochastic bifurcation to chaos.

The synchronization transition changes significantly when bidirectional coupling is considered. When the common laser is also receiving the signal of the outer ones, it modifies its dynamics according to the other lasers acting as a communication relay [152]. The simplest coupling scheme for this scenario can be found in a chain of three bidirectionally coupled semiconductor lasers as shown schematically in Fig. 3.11(b). Two of the lasers (1 and 3) are coupled through the central one (2) that receives the input of the two outer lasers. If the lasers are different, for example if two lasers are pumped below the lasing threshold and the third one above the lasing threshold, the latter can induce dynamics to the other lasers acting as a master laser, which strongly determines the dynamics of the whole system. When the lasers are identical or similar enough, the system can be mutually synchronized in the sense that a master laser can not be clearly identified and the final states result from

the collective dynamics of the system. It was shown in [153, 154] that identical lasers, without intrinsic chaotic dynamics when they are not coupled, can show identical synchronization of chaotic dynamics between the outer lasers for moderate coupling strengths while the central one is not synchronized with the outer lasers. Differences in the synchronization can be observed when the oscillators are chaotic in the absence of coupling. Using the same coupling topology but in identical Chua circuits [155], identical synchronization was observed between the outer oscillators while the outer and the central oscillators show generalized synchronization.

When the time delay of the coupling, that is the time required for the signal to propagate from the emitter to the receiver laser, is much shorter than the characteristic time scales of the devices, it can be neglected. The coupling can be considered instantaneous if the lasers are separated short enough distances. However, when the delay is comparable or larger than the characteristic time scales, it has to be considered in the coupling with important consequences in the dynamics [156, 157, 158]. A nontrivial case of synchronization arises when two or more oscillators coupled with time delay synchronizes at zero-lag under the appropriate conditions [152]. Isochronal synchronization has been identified as an important mechanism in neuronal activity between distant regions of the brain [159] and can also be observed in coupled chaotic oscillators.

When considering the synchronization of two identical mutually coupled, i.e. bidirectionally coupled, chaotic oscillators with time delay and feedbacks, e.g. lasers with feedback or iterative maps, **zero-lag synchronization** can be found for certain ratios of coupling and feedback time delays [160, 161, 162]. In the case of only two bidirectionally coupled lasers without feedback, the identical synchronization has been found to be unstable when there are no detunings between their optical frequencies. When there is a small detuning the laser with higher optical frequency leads the dynamics [86, 163]. Furthermore, anticipated synchronization was observed in SCLs unidirectional coupled with time delay [89, 90] where the slave laser anticipates the chaotic dynamics of the master laser. These concepts were used in

[164] to design a mechanism of transmitter-mediator-receiver without time delay between the transmitter and the receiver signal.

A general and robust mechanism for isochronal synchronization can be achieved when two delay-coupled oscillators are only connected through a third mediating element [152]. By using semiconductor lasers, and numerically validated for other systems, identical zero-lag synchronization between the outer lasers is observed while, the central laser lags the dynamics a time equal to the time delay of the coupling as can be seen in Fig. 3.12.

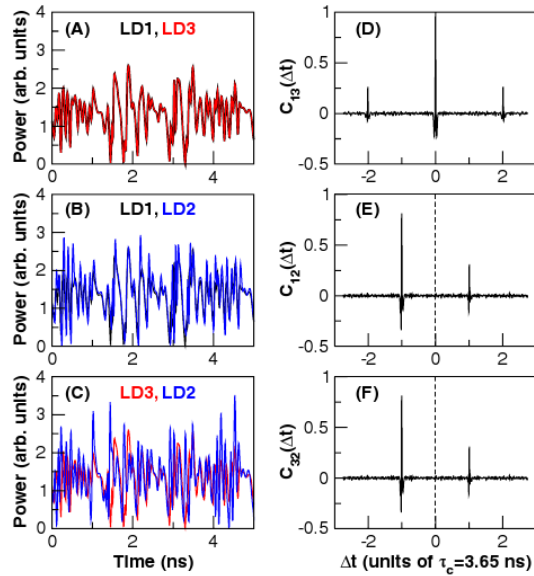


Figure 3.12: (A), (B) and (C) Pairs of time traces for the outer lasers LD1 and LD3 and the central laser LD2. The time trace for LD2 is shifted one time delay for better comparison. (D), (E) and (F) cross-correlations between those pairs of time traces. From [152].

This mechanism is still valid for mismatches in the parameters of the individual lasers in such a way that when the spectral detuning between lasers is of the order of 15 GHz correlations of the time traces larger than the 80% can be observed, and

identical synchronization can be achieved for large mismatches in the time delay but with a temporal shift equal to the difference between them.

3.4.2 Synchronization phenomena controlled by the system size

As it was previously discussed, coordinated activity can emerge spontaneously when there is not a clear leader of the dynamics and the resulting dynamics of the group can be different from the dynamics of its components. In these cases, the synchronization is the result of the contribution of each non-identical individual element and a consequence of the interactions of the group as was discussed for the case of three bidirectionally coupled SCLs.

An unexpected example of spontaneous collective synchronization occurred in the Millennium Bridge in London in 2000. Two days after its opening, the pedestrian bridge had to be closed because its excessive wobbling in the transverse direction. Subsequent investigations [165] revealed that the pedestrians, initially walking with different frequencies and phases, fell into step spontaneously when the number of pedestrians was large enough. That effect was modeled and understood a few years later in terms of the so-called **crowd synchrony**. The system was successfully described as a group of M independent Kuramoto oscillators, modeling the pedestrians, with a small dispersion in their frequencies, coupled through a weakly damped and driven harmonic oscillator as a common medium, representing the bridge [166, 167]. The authors found that below a critical number of pedestrians, each oscillator evolves almost independently, doing a null averaged force to the bridge (Fig. 3.13(a)). Above the critical value, the pedestrians become progressively synchronized (Fig. 3.13(b)) and the bridge oscillates with small amplitude while for large M almost all the pedestrians oscillate in phase (Fig. 3.13(c)).

Wobbling and synchrony emerge simultaneously at a value $M = M_c$ (Fig. 3.14(a))

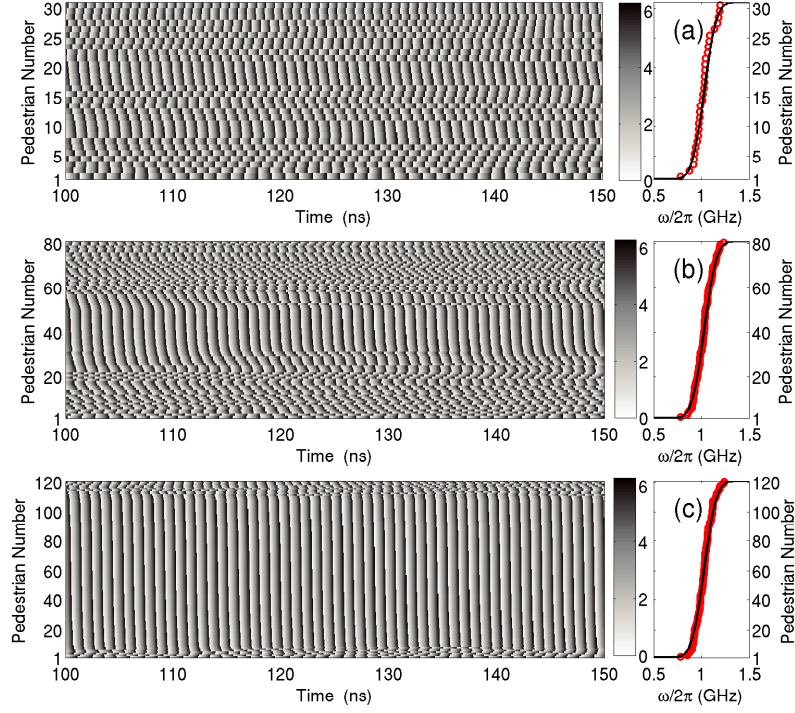


Figure 3.13: Left panel: time traces for the phase of the pedestrians in radians sorted by their solitary frequencies for (a) $M = 30$, (b) $M = 80$ and (c) $M = 120$. Right panel: the ideal Gaussian cumulative distribution (solid line) and the pedestrians' frequencies (dots).

and (b)) given in terms of the parameters of the model as

$$M_c = \frac{A}{GCP(\Omega_0)} \quad (3.1)$$

where A is a constant value that depends on the bridge characteristics, G is the maximum force imparted by each pedestrian, C is the sensitivity of the pedestrians to the bridge movement and $P(\Omega_0)$ is the density distribution of the pedestrian frequency at the bridge natural frequency Ω_0 .

Other examples can be found in the literature where a certain critical number of elements are required for the appearance of a collective behavior. First introduced in the framework of biology, **quorum sensing** is a mechanism of cell-cell communication which involves the production, release and community wide detec-

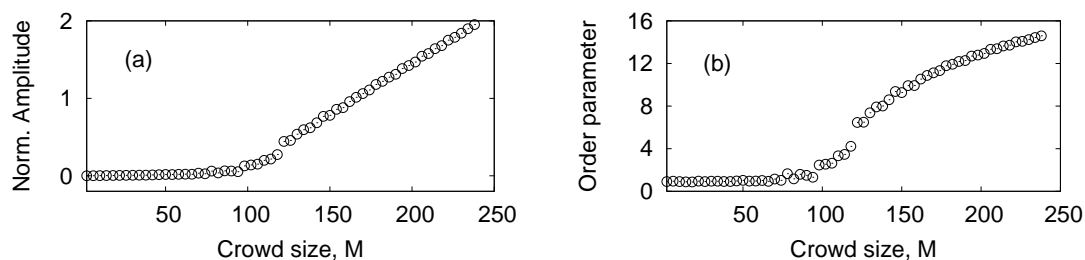


Figure 3.14: (a) Normalized amplitude of the bridge, defined as $A\sqrt{M}$, as a function of the crowd size. (b) Normalized order parameter, defined as $|\sum e^{i\phi}|/\sqrt{M}$ where ϕ is the phase of each pedestrian, as a function of the crowd size. From Eq. (3.1), $M_c = 112$.

tion of signaling molecules. When the number of cells and the conditions of the medium surrounding the cell, which contains the signaling molecules, are appropriated, each member of a population undergoes a sudden change in behavior with a supercritical increase in the concentration of signaling molecules in the extracellular solution, leading to the **quorum sensing transition** [168]. Quorum sensing has inspired research in other fields extending this behavior to whole organisms, chemical reactions and swarm robots [169, 170, 171]. Recently, it has been reported that chemical oscillators also show a transition to a synchronized state when the number of elements is above a certain number [170]. In that experiment, a large number of catalyst particles were introduced in a catalyst free Belousov-Zhabotinsky reaction mixture. The particles induce a periodic chemical reaction locally changing the color of the medium. While the period of the catalyst particles was slightly different due to their different sizes, a transition from no-oscillations or incoherent oscillations to coordinated behavior was found for a large enough number of catalysts in the surrounding. Furthermore, how the transition to the synchronized state occurs can be controlled by the exchange rate of chemical species, proportional to the stirring rate of the system, between the catalysts and the surrounding. For low stirring rates (Fig. 3.15(A)), a low density of particles leads to incoherent oscillations of them while above a certain density, more and more catalysts modify their periods

to oscillate synchronously, thus, a smooth transition to the coherent state occurs. For large stirring rates (Fig. 3.15(B)), oscillations are no longer supported for small densities but a sharp transition to the coherent state occurs above a critical density equivalently to what can be observed in the quorum sensing transition.

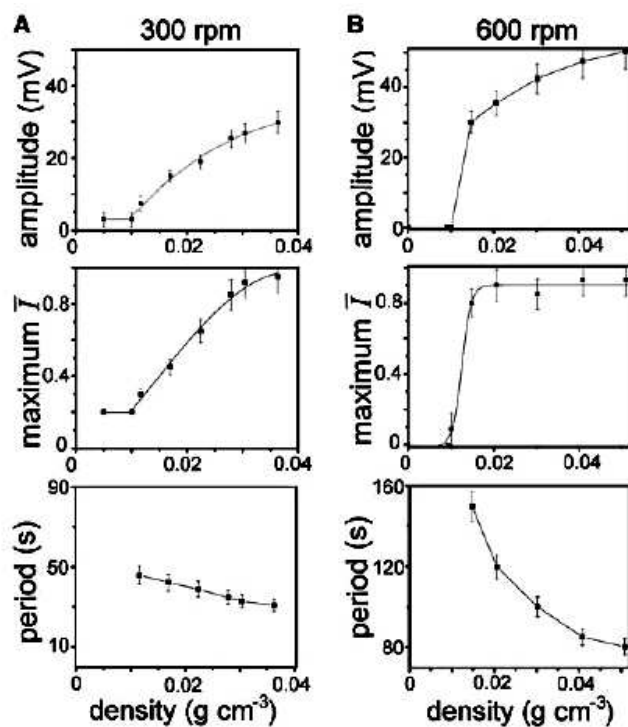


Figure 3.15: Transition to the synchronized state for (A) small stirring rate and (B) large stirring rate. From top to bottom: the voltage of the surrounding medium, the intensity of the color change and the period of the oscillations as a function of the catalyst density. From [170].

Part II

RESULTS

Chapter 4

Generation of optical pulses in VCSELs below the static threshold

In this chapter we will consider the dynamics induced by asymmetric modulation of the injection current of a VCSEL. The goal is to study if, by using a suitable asymmetric shape, optimal laser intensity pulses can be obtained. Different methods have been proposed for optimizing the performance of directly modulated semiconductor lasers [172, 173] by shaping the current input and exploiting the nonlinear and stochastic light-matter interactions. Appropriate square-shaped current inputs allow to control the laser time-evolution in the plane (photon density, carrier density). In [172] the aim was to avoid dynamical memory effects that arise because even if the observable intensity has returned to its stationary value after a current waveform was applied, the unobservable carrier density may not have reached its stationary value. By suppressing dynamical memory effects the laser output is not influenced by previously communicated information, which improves its performance in digital data communication systems. In [173] adequate square-shaped injection current inputs were demonstrated numerically and experimentally, to switch on a semiconductor laser without relaxation oscillations (first a large pump value was

applied to speed up the switch-on, followed by a lower value, temporarily below threshold, tailored to eliminate just the right amount of the accumulated carriers, whose excess would otherwise cause damped relaxation oscillations). The method presented in this chapter [174] for the generation of optimal pulses with low average injection current via asymmetric modulation is motivated by an experimental and theoretical study using a $\text{Nd}^{3+}:\text{YVO}_4$ diode-pumped laser [175], where asymmetric modulation was applied to the power delivered by the pumping diode laser. It was shown that an asymmetric triangular signal with a slow raising ramp can lead to the emission of pulses, even when the laser is operated, on average, below threshold. In contrast, a signal with a fast raising ramp and the same averaged value does not lead to pulse emission, the intensity remains at the noise level during all the modulation cycle. Here we show that a similar effect can be observed in VCSELs but with much faster modulating signals. We show that under suitable modulation parameters **subnanosecond pulses** on two orthogonal linear polarizations can be obtained even through the injection current is, on average, below the cw threshold. Additionally, we find a stochastic resonance phenomenon as an optimal amount of noise leads to maximum pulse amplitude accompanied by minimum amplitude dispersion.

4.1 Asymmetric triangular current modulation

As described in Section 2.2, the SFM model [73] successfully reproduces the polarization dynamics of a VCSEL and is a suitable model in order to study the response of a VCSEL under current modulation. Equations (2.17), (2.18) and (2.19) have been integrated using the explicit Euler method with a time step of 10^{-2}ps , short enough to ensure the convergence of the integration algorithm. The dynamics is studied in terms of the intensity for the two orthogonal polarizations, $|E_x|^2$ and $|E_y|^2$, and the total intensity as $|E_T|^2 = |E_x|^2 + |E_y|^2$.

The time dependent pump current, $\mu(t)$, is modulated with an asymmetric triangular signal of amplitude $\Delta\mu$, rising from μ_0 (which coincides with the minimum value of μ) a time interval T_1 , and falling back to μ_0 a time interval T_2 , as shown in Fig. 4.1. One modulation cycle is given by

$$\mu(t) = \mu_0 + \Delta\mu (t/T_1) \text{ for } 0 \leq t \leq T_1, \quad (4.1)$$

$$\mu(t) = \mu_0 + \Delta\mu[1 - (t - T_1)/T_2] \text{ for } T_1 \leq t \leq T_1 + T_2. \quad (4.2)$$

and according to these definitions the mean pump current is $\mu_m = \mu_0 + \Delta\mu/2$ and is independent of the modulation period, $T = T_1 + T_2$. The asymmetry of the modulation is characterized by the parameter $\alpha_a = T_1/T$ with $0 \leq \alpha_a \leq 1$, which is the ratio between the signal rising time and the modulation period.

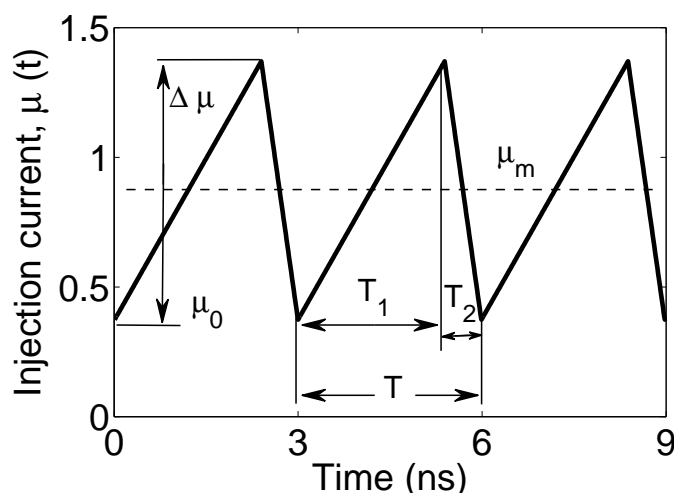


Figure 4.1: Time trace of the current variation and its characteristic parameters.

Equations (2.17), (2.18) and (2.19) were simulated with the typical VCSEL parameters shown in Table 2.1: $k = 300 \text{ ns}^{-1}$, $\alpha = 3$, $\gamma_N = 1 \text{ ns}^{-1}$, $\gamma_a = 0.5 \text{ ns}^{-1}$, $\gamma_p = 50 \text{ rad/ns}$, $\gamma_s = 50 \text{ ns}^{-1}$, and $D = 10^{-6} \text{ ns}^{-1}$ as . We chose these parameters not only because they are typically used in the literature [73], but also, because there is no polarization coexistence or elliptically polarized light, i.e., the laser emits

either the x or the y polarization for a constant pump current, and this gives the chance to show how the stability of these polarizations changes with the current modulation.

4.2 Characterization of optical pulses

As discussed in Sec. 3.1, when sweeping a control parameter slowly through a bifurcation point, the phenomenon of critical slowing down occurs and results in dynamical hysteresis [93]. In Fig. 4.2 we illustrate this effect at the laser threshold by plotting the time traces for a periodic and **asymmetric current modulation**, for a slow increasing and a fast decreasing of the pump current parameter, μ , and four different periods. In Fig. 4.2(a) the current is swept slowly through the cw threshold (at $\mu_{s,th} = 1$), and is progressively increased in Fig. 4.2(b)-(d), where the sweep is much faster. In the slow sweep, Fig. 4.2(a), when μ grows above the dynamic lasing threshold, the laser turns on with a few relaxation oscillations. If the sweep is faster the amplitude of those oscillations grows (Fig. 4.2(b)) and, eventually, the intensity falls to 0 before the second oscillation (Fig. 4.2(c)). If we now repeat periodically the linear increase and decrease of the pump current parameter with a period short enough, only one pulse per cycle is emitted due to the transition from the non-lasing to the lasing state through those relaxation oscillations, as shown in Fig. 4.2(d).

Therefore, a fast triangular current modulation (symmetric or not symmetric) crossing the cw threshold can result in the emission of short pulses of both orthogonal polarizations even when the current is, on average, below the static threshold, $\mu_{s,th}$ (Fig. 4.3(a)). Because of the presence of noise, which is crucial at threshold, these pulses are irregular, both in amplitude and in timing. The characteristics of these pulses depend on the shape of the triangular signal modulating the current, $\mu(t)$, that can be characterized in terms of the four parameters, μ_0 , $\Delta\mu$, T , and α_a described above.

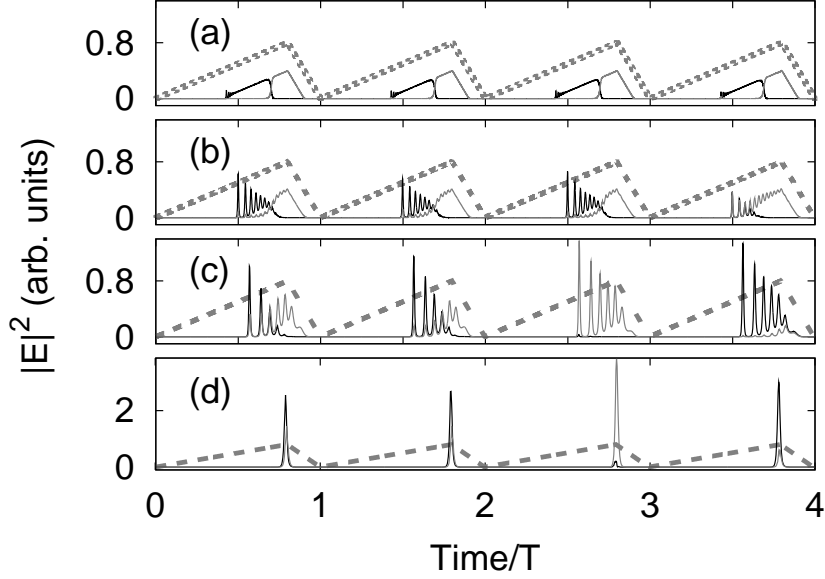


Figure 4.2: Time traces of the intensities of the orthogonal linear polarizations: $|E_x|^2$ (gray solid line), $|E_y|^2$ (black solid line), and the injection current as $\mu(t) - \mu_0$ (dashed) when the injection current increases and decreases linearly, from $\mu_0 = 0.6$ to $\mu_f = 1.4$ for different periods. (a) $T=100$ ns, (b) $T=20$ ns, (c) $T=10$ ns and (d) $T=3$ ns. For $\alpha_a = 0.8$.

The modulation period and amplitude are chosen such that the laser emits only one sharp pulse per modulation cycle, that is triggered at the end of the cycle. The emission starts when $\mu(t)$ is still above 1, as can be seen in Fig. 4.3(a). This is in good agreement with the observations of [175], and can be interpreted as due to the nonlinear interplay of the photons and the carriers in the VCSEL active region, as will be discussed later.

In Figs. 4.3(b)-(d) the dashed lines represent three different asymmetries: slow-rising and fast-decreasing ($\alpha_a = 80\%$), almost symmetric ($\alpha_a = 60\%$) and fast-rising and slow-decreasing ($\alpha_a = 20\%$). Those plots also show the resulting time traces of the intensities of the two linear polarizations, $|E_x|^2$ and $|E_y|^2$, for three values of the asymmetry parameter, α_a . For $\alpha_a = 80\%$ large pulses are emitted, Fig. 4.3(b). A detail of a pulse in Fig. 4.3(b) is shown in Fig. 4.3(a). For decreasing α_a , i.e.

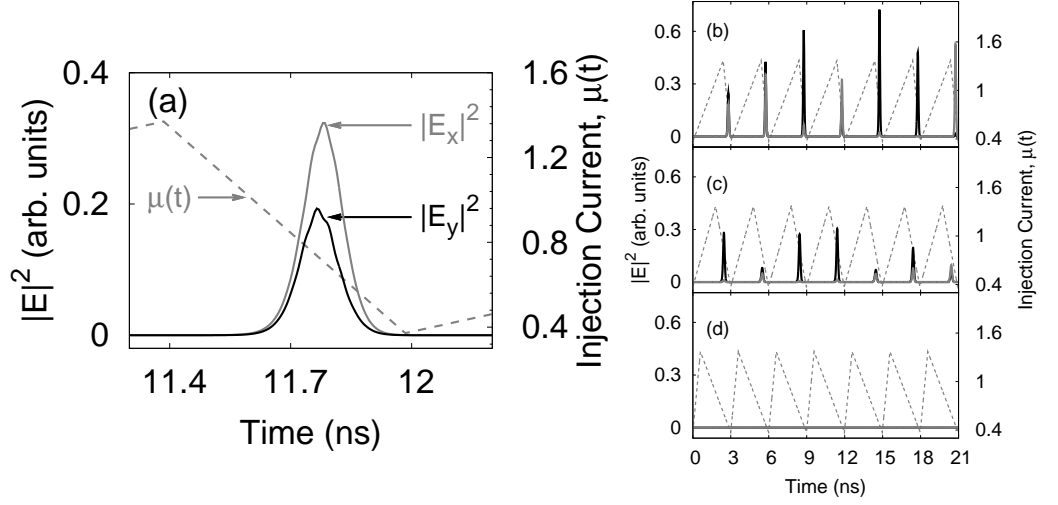


Figure 4.3: (a) In the left axis the time traces of the intensities of the orthogonal linear polarizations: $|E_x|^2$ (gray solid line), $|E_y|^2$ (black solid line), and in the right axis the injection current $\mu(t)$ (dashed) for a period $T=3$ ns. (b)-(d) As in (a), time traces of the intensities for an asymmetry parameter (b) $\alpha_a=80\%$, (c) 60% and (d) 20% . The modulation amplitude is $\Delta\mu=1$, the DC value is $\mu_0=0.37$ and $\mu_m = 0.87 < 1$. Notice that panel (a) is a detail of panel (b).

going to a more symmetric modulation, the pulse amplitude gradually decreases (see Fig. 4.3(c) where $\alpha_a = 60\%$). If we continue decreasing α_a (considering the opposite asymmetric shape, with a fast-rising and slow-decreasing ramp) the pulses become smaller and eventually there are no pulses as the intensities of the two polarizations remain at the noise level (see Fig. 4.3(d) where $\alpha_a = 20\%$).

Therefore, when the current modulation is asymmetric, there is a clear difference between the two asymmetry shapes: a slow-rising ramp followed by a fast-decreasing one and the opposite situation, a fast-rising ramp followed by a slow-decreasing one.

The effect of the asymmetry of the current modulation on the characteristics of the intensity pulses is presented in Fig. 4.4. Figure 4.4(a) displays the time averaged intensities of the two linear polarizations, $\langle |E_x|^2 \rangle$ and $\langle |E_y|^2 \rangle$, and the time averaged

total intensity, $\langle |E_T|^2 \rangle = \langle |E_x|^2 + |E_y|^2 \rangle$, vs. the asymmetry parameter, α_a . In Fig. 4.4(b) we display the time averaged pulse amplitudes given by the maximum intensity in a cycle for the x polarization, $\langle A_x \rangle$, for the y polarization, $\langle A_y \rangle$, and for the total intensity $\langle A_T \rangle$ (when there is more than one pulse per modulation cycle, we calculate the average amplitude of the largest pulse). The amplitudes are one order of magnitude larger than the intensities because the laser emits sharp pulses and is off during most of the modulation cycle. Figure 4.4(c) displays the dispersion of the amplitude of that pulses, characterized in terms of the standard deviation normalized to the mean amplitude. In all three measures there is an optimal modulation asymmetry $\alpha_a \cong 80\%$ for which the averaged intensity and pulse amplitude reach their maximum value, and for this asymmetry the dispersion of the pulse amplitude exhibits its minimum value.

The emitted pulses strongly depend on the initial conditions of the cycle which are given by the dominance of one of the following mechanisms: the spontaneous emission and the radiation left by the previous pulse. When the radiation left by the previous pulse is absorbed by the carriers during the fall part of the cycle, spontaneous emission is the dominant mechanism for triggering the next pulse in the next cycle. On the contrary, when the radiation left has not been completely absorbed, it dominates over spontaneous emission for triggering the next pulse. We interpret our results as in [175], where the authors found that for small asymmetries the spontaneous emission is the dominant mechanism while for large asymmetries dominates the radiation left by the previous pulse.

The averaged total amplitude of the pulses is shown in Fig. 4.4(d) as a function of α_a and μ_m for a fixed $\Delta\mu = 1$ [$\Delta\mu$ is the same as in Figs. 4.4(a)-(c), thus, Fig. 4.4(b) is an horizontal scan in Fig. 4.4(d)]. We have used μ_m instead of μ_0 to emphasize that the laser emission occurs with a pump current that is on average below $\mu_{s,th} = 1$. As the pump current is modulated, it is suitable to define an effective lasing threshold as the averaged pump current above which the laser turns on. The modulation reduces the effective threshold which depends on the asymmetry, giving the largest

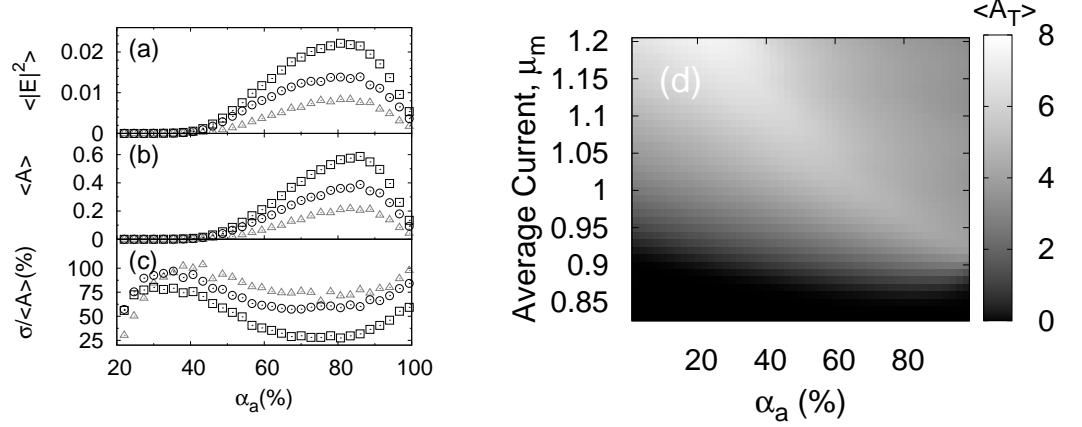


Figure 4.4: (a) Time averaged intensities, (b) pulse amplitudes, and (c) normalized standard deviation of the pulse amplitude as a function of the asymmetry parameter, α_a . In (a)-(c) x polarization (Δ), y polarization (\circ) and total intensity (\square). (d) Color plot of the average pulse total amplitude, $\langle A_T \rangle$ in the parameter plane for the asymmetry parameter, α_a , and the averaged pump current, $\mu_m = \mu_0 + \Delta\mu/2$. The modulation amplitude is $\Delta\mu=1$ and the period is $T=3$ ns. The DC value $\mu_0=0.37$ is fixed in captions (a)-(c) and is varied in (d).

threshold reduction and the maximum amplitude for an optimal $\alpha_a \sim 80\%$. For increasing μ_m the maximum amplitude moves to lower asymmetries, for which it has a fast rising ramp followed by a slow decreasing one.

The effective threshold depends also on the modulation parameters μ_0 and $\Delta\mu$. Figures 4.5(a)-(c) show the averaged intensities, $\langle |E_x|^2 \rangle$, $\langle |E_y|^2 \rangle$ and $\langle |E_T|^2 \rangle$, for $\alpha_a = 0.8$ and three values of $\Delta\mu$. In each caption $\Delta\mu$ and α_a are kept fixed while μ_0 varies, but in the horizontal axis we plot μ_m instead of μ_0 to show that, for large $\Delta\mu$ and small μ_0 , there is laser emission with $\mu_m < 1$. $\langle |E_T|^2 \rangle$ increases with μ_m , and for large $\Delta\mu$, Figs. 4.5(a) and (b), the relation is nonlinear; kinks appear which are due to the emission of additional pulses in each modulation cycle. Notice that the modulation of the current leads to emission of both polarizations even when the

x one is unstable for a constant injection current.

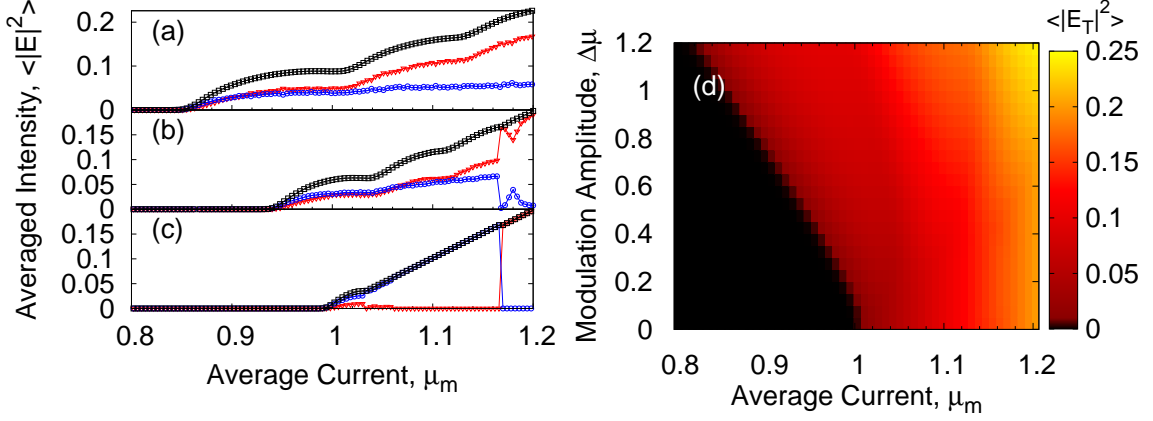


Figure 4.5: (a)-(c) Time averaged intensities [x polarization $\langle |E_x|^2 \rangle$ (red), y polarization $\langle |E_y|^2 \rangle$ (blue) and total intensity $\langle |E_T|^2 \rangle$ (black)] vs. average current, μ_m , for different modulation amplitudes (a) $\Delta\mu=1.0$, (b) 0.5, and (c) 0.15. (d) Color plot of $\langle |E_T|^2 \rangle$. The asymmetry parameter $\alpha_a=0.8$ and the period $T=3$ ns are fixed.

The variation of the effective threshold with both μ_0 and $\Delta\mu$ is illustrated in Fig. 4.5(d), that presents a color-coded 2D plot of $\langle |E_T|^2 \rangle$. Also here the horizontal axes displays μ_m instead of μ_0 , and Figs. 4.5(a)-(c) correspond to horizontal scans in 4.5(d). In the bottom-left corner of Fig. 4.5(d), $\Delta\mu$ and/or μ_0 are too small, the black color representing the intensity at the noise level, and the laser does not turn on. We observe a smooth turn-on: as $\Delta\mu$ and/or μ_0 increase, $\langle |E_T|^2 \rangle$ gradually increases.

Figure 4.6 displays the time averaged pulse amplitude, $\langle A_T \rangle$, for the same parameters as Fig. 4.5. It can be noticed that near the effective threshold $\langle A_T \rangle$ increases nearly linearly with μ_m , while for larger μ_m , $\langle A_T \rangle$ saturates but $\langle |E_T|^2 \rangle$ continues increasing with μ_m , as seen in Fig. 4.5. This is due to the fact that the laser emits more than one pulse per modulation cycle and the carriers that generate one short pulse for small μ_m now generate two pulses in a longer time interval.

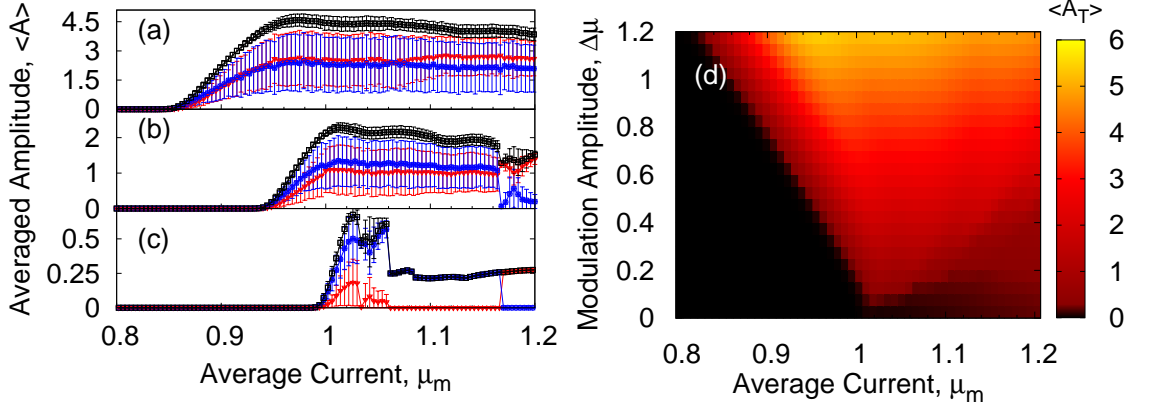


Figure 4.6: (a)-(c) Time averaged pulse amplitudes [x polarization $\langle A_x \rangle$ (red), y polarization $\langle A_y \rangle$ (blue) and total amplitude $\langle A_T \rangle$ (black)] vs. average current, μ_m , for different modulation amplitudes (a) $\Delta\mu=1.0$, (b) 0.5, and (c) 0.15. (d) Color plot of the average total intensity, $\langle A_T \rangle$. Parameters are as in Fig. 4.5.

4.2.1 Influence of noise in pulse generation

As previously discussed, near the lasing threshold noise plays a key role in the emission of the pulses and the interplay between the pump current modulation and the noise strength is expected to produce constructive effects enhancing the input signal.

In Fig. 4.7(a)-(c) we show the time traces of the intensities of the polarizations for a fixed modulation asymmetry, $\alpha_a = 0.8$, and three different noise strengths, D . Large spontaneous emission triggers the pulses at the end of the rising ramp, Fig. 4.7(a). An optimal noise strength $D \sim 10^{-3} \text{ ns}^{-1}$ produces pulses with the largest amplitude triggered at the very beginning of the falling ramp when the pump current reaches its maximum value, Fig. 4.7(b). For lower D values the pulses are emitted at the end of the falling ramp of the cycle and their amplitude gradually decreases to zero, Fig. 4.7(c).

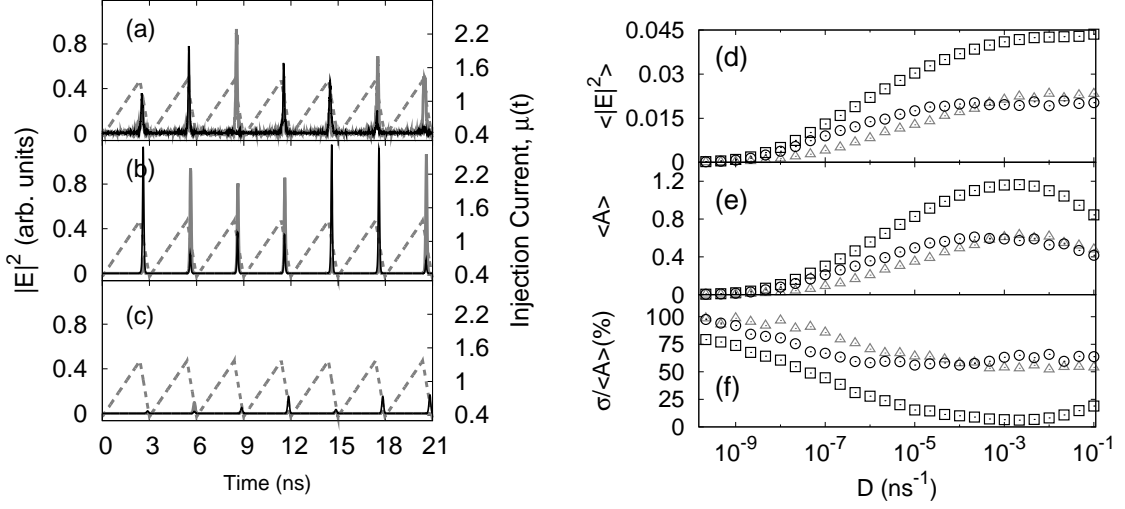


Figure 4.7: (a)-(c) Time traces of the intensities for fixed asymmetry parameter $\alpha_a = 0.8$ and three noise strengths (a) $D=10^{-1} \text{ ns}^{-1}$, (b) $D=10^{-3} \text{ ns}^{-1}$ and (c) $D=10^{-8} \text{ ns}^{-1}$. In the left axis the time traces of the intensities of the orthogonal linear polarizations: $|E_x|^2$ (gray solid line), $|E_y|^2$ (black solid line), and in the right axis the injection current $\mu(t)$ (dashed). (d) Time averaged intensities, (e) pulse amplitudes, and (f) normalized standard deviation of the pulse amplitude as a function of the noise strength. In (d)-(f) x polarization (Δ), y polarization (\circ) and total intensity (\square). The modulation amplitude is $\Delta\mu=1$, the DC value is $\mu_0=0.37$, the asymmetry parameter is $\alpha_a=0.8$ and the period is $T=3 \text{ ns}$.

In Figs. 4.7(d), (e) and (f) we show the time averaged intensities, pulse amplitudes and dispersion of the pulse amplitudes, respectively, as a function of the noise strength, D . While the intensity grows monotonically with the noise strength until it saturates, the amplitude of the pulses shows a maximum at $D \sim 10^{-3} \text{ ns}^{-1}$, which is accompanied by the minimum dispersion. This optimal emission for a finite noise strength is a hallmark of stochastic resonance [131] in our system. Here, the effect of the noise over the amplitude of the pulses is much more clear than in the period of the pulses which occurs almost synchronized with the current modulation.

The appearance of a stochastic resonance highlights the interplay between the

pulse triggering mechanisms. As we discussed before, the radiation left by the previous pulse dominates for large α_a . Thus, by increasing D we are enhancing the effect of the spontaneous emission in the triggering process. The turn-on occurs earlier, in a pump current modulation cycle, since the noise perturbation makes the system easier to reach the lasing state. On the other hand, the earlier pulse, the lower radiation left to the next pulse. The maximum amplitude in Fig. 4.7(e) gives the optimal noise intensity for which the radiation left is not too low and the noise is not too large.

4.3 Conclusions and discussion

The dynamics of a VCSEL driven by asymmetric triangular current modulation was studied numerically using the spin-flip model. When the injection current is on average below the cw threshold, irregular optical pulses in two orthogonal linear polarizations can be generated by using large amplitude modulation of period of a few nanoseconds. For an optimal modulation asymmetry, with a slow rising ramp followed by a fast decreasing one, the effective threshold reduction is about 20%, the pulse amplitude is maximum and the dispersion of the pulse amplitude is minimum. In contrast, when the averaged current value is above the static threshold, the optimal modulation asymmetry that leads to maximum pulse amplitude has a fast rising ramp followed by a slow decreasing one.

The pulsed dynamics can be optimized by modifying the noise strength. The system shows a stochastic resonance for a finite amount of noise that leads to the maximum pulse amplitude and the minimum dispersion of the amplitude.

Those results are interpreted in terms of the interplay between the two mechanisms triggering the emission of a pulse: the spontaneous emission and the radiation left by the previous pulse.

Chapter 5

Logical stochastic resonance in VCSELs

As discussed in the previous chapter, stochastic resonance [131] is a common effect in nonlinear systems. Recently, a new kind of stochastic resonance has been demonstrated, named **logical stochastic resonance** (LSR). In this chapter we demonstrate that LSR occurs in current-modulated VCSELs.

LSR uses the non-linear response of a bistable system to reproduce logical operations such as the AND and OR operations, under the influence of the right amount of noise. The main idea behind LSR is that the input levels can be chosen such that the probability of the switchings between two logical outputs is controlled by the noise strength [142]. In [142] the authors demonstrated that a two-state system with two adjustable thresholds, modeled by a 1D double-well potential, can act as a reliable and flexible logic gate in the presence of an appropriate amount of noise. LSR has also been numerically and experimentally demonstrated in a large variety of systems such as electronic circuits, tunneling diodes or chemical systems [176, 177, 178, 179, 180].

In the last years much research has been devoted to the study of optical devices

acting as logical operators, an application limited mostly to the electronic circuits so far. Specially interesting is the use of pump current or optical modulation as the input signal to generate a logical output when it is applied to a bistable laser. In this chapter we discuss the implementation of a VCSEL-based stochastic logical operator using an **aperiodic current modulation** and the linearly polarized light as the output signal. Here, we propose a novel method for exploiting polarization bistability in VCSELS, based on the interplay of nonlinearity, bistability and noise [181]. We performed numerical simulations of the spin-flip model and showed that VCSELS operating in polarization bistable regimes can display LSR, which can be used to realize VCSEL-based robust logic gates that give a reliable logic response to two logic inputs, even in the presence of a significant amount of noise. The two logic inputs are encoded in a three-level aperiodic signal directly applied to the laser bias current. Exploiting polarization bistability, one can consider that the laser response is a logic 1 if one polarization is emitted, and a logic 0 if the orthogonal polarization is emitted. Then, the truth table of the fundamental logical operators AND and OR (and their negations, NAND and NOR) can be reproduced and we show that the probability of a correct response is equal to one in a wide range of noise strengths and laser parameters.

5.1 Aperiodic current modulation

As in the previous chapter, we use the framework of the SFM model [73], as described in section 2.2, to describe the response of a VCSEL to aperiodic current modulation. Equations (2.17), (2.18) and (2.19) have been integrated using the explicit Euler method with a time step of 10^{-1} ps, short enough to ensure the convergence of the integration method. The dynamics is studied in terms of the intensity for the two orthogonal polarizations, $|E_x|^2$ and $|E_y|^2$, and the total intensity as $|E_T|^2 = |E_x|^2 + |E_y|^2$.

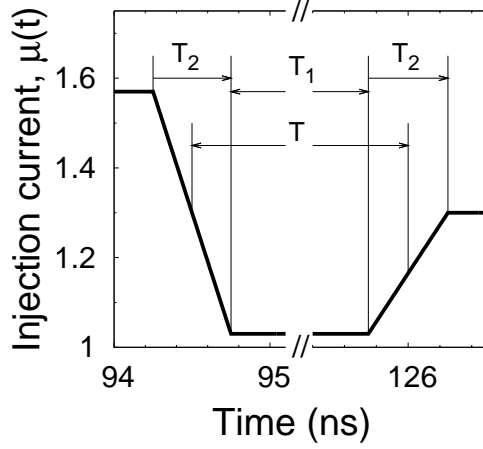


Figure 5.1: Time trace of the current variation within a bit

The shape of the three-level signal applied to the time dependent laser pump current, $\mu(t)$, is shown in Fig. 5.1. Within each modulation bit, the current is constant during a time interval T_1 , referred to as the step time, then, there is a ramp (up or down) to the current level encoding the next bit. The time required for the signal to change from one value to the next (the rise time or the fall time depending on the bit sequence), T_2 , is such that $T_2 \ll T_1$. Each bit begins at the middle of one ramp and finishes at the middle of the next one, as indicated in Fig. 5.1, and thus the length of the bit is $T = T_1 + T_2$. As will be discussed in the next section, the value of T_1 strongly influences the reliability of the VCSEL logic gate, but the value of T_2 does not affect significantly the operation, as long as $T_2 \ll T_1$.

The model equations were simulated with the parameters shown in Table 2.1: $k = 300 \text{ ns}^{-1}$, $\alpha = 3$, $\gamma_N = 1 \text{ ns}^{-1}$, $\gamma_a = 0.5 \text{ ns}^{-1}$, $\gamma_p = 50 \text{ rad ns}^{-1}$ and $\gamma_s = 50 \text{ ns}^{-1}$, unless otherwise specifically stated. As will be discussed later, the operation of the VCSEL-based stochastic logic gate (SLG) is robust and does not require fine tuning of the parameters. In the following we focus on the logic OR operation and, unless otherwise specifically stated, we use the following parameters for the three-

level aperiodic signal: $\mu_m = 1.3$, $\Delta\mu = 0.27$, $T = T_1 + T_2 = 31.5$ ns, $T_1 = 31$ ns, and $T_2 = 0.5$ ns. When the time duration of the bit T is varied, T_1 and T_2 are varied such that their ratio is kept constant.

5.1.1 Encoding scheme of the VCSEL logical response

In this section we analyze how two logic inputs can be encoded in a three-level aperiodic modulation directly applied to the laser pump current, and how to define the laser logical response.

Let us consider that the pump current parameter, $\mu(t)$, is the sum of two aperiodic square-waves, $\mu(t) = \mu_1(t) + \mu_2(t)$, that encode the two logic inputs. Since the logic inputs can be either 0 or 1, we have four distinct input sets: (0, 0), (0, 1), (1, 0), and (1, 1). Sets (0, 1) and (1, 0) give the same value of μ , and thus, the four distinct logic sets reduce to three μ values. Then, it is more convenient to introduce as parameters the mean value, μ_m , and the amplitude of the modulation, $\Delta\mu$, which, without loss of generality, determine the three current levels as $\mu_m - \Delta\mu$, μ_m , and $\mu_m + \Delta\mu$.

The laser response is determined by the polarization of the emitted light. We chose parameters such that the laser emits either the x or the y polarization (parameter regions where there is anti-correlated polarization coexistence or elliptically polarized light are avoided). The laser response is considered a logical 1 if, for instance, the x polarization is emitted, and a logical 0, if the y polarization is emitted. Which polarization represents a logic 1, and which a logic 0 can depend on the logic operation, as will be discussed latter.

In this way, the polarization emitted at the three current levels, encoding the four possible combinations of the two logic inputs, allows to implement the operations OR, AND, NOR, NAND, according to Table 5.1. One should notice that by detecting one polarization one obtains a logic response and, by detecting the orthogonal

Table 5.1: Relationship between the two inputs and the output of the logic operations.

Logic inputs	AND	NAND	OR	NOR
(0,0)	0	1	0	1
(1,0)/(0,1)	0	1	1	0
(1,1)	1	0	1	0

polarization, one obtains the negation of that logic response. In the following we focus only on the non-negation operations AND and OR.

There are two ways to associate the four possible logic inputs, (0,0), (1,0), (0,1), (1,1), to three current levels. The first one is schematically illustrated in Fig. 5.2. In the presence of a right amount of noise, the levels μ_I , μ_{II} , μ_{III} can lead to the operation AND, and levels μ_{II} , μ_{III} , μ_{IV} , to the operation OR.

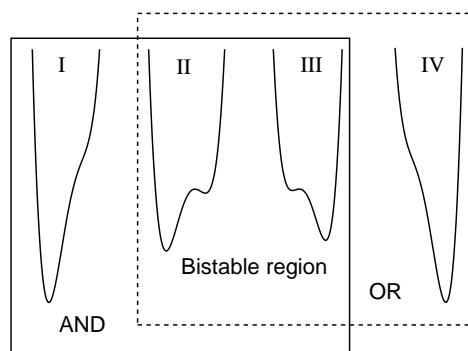


Figure 5.2: Schematic representation of the effective potential at four different pump current values, corresponding to labels I to IV in Fig. 3.10(d). The solid square indicates the three values that can be used for implementing a logic AND; the dashed square indicates the three values that can be used for implementing a logic OR (see text for details).

Let's explain the idea by first considering the operation AND. Assuming that x represents a logical 1 and y represents a logical 0, and assuming that the laser is emitting the y polarization, only the current level μ_{III} , representing the logic input

Table 5.2: Encoding scheme I: Relationship between the logic inputs, the encoding current levels, the output polarization and the logic output for the AND and OR operations.

Logic inputs	AND:			OR:		
	Current	x/y	Logic output	Current	x/y	Logic output
(0,0)	μ_I	y	0	μ_{II}	y	0
(1,0)/(0,1)	μ_{II}	y	0	μ_{III}	x	1
(1,1)	μ_{III}	x	1	μ_{IV}	x	1

(1,1), will induce a switch to the x polarization; however, the probability of this switch will be controlled by the noise strength.

Let's now consider the operation OR: if the laser is emitting the y polarization, the current levels μ_{III} and μ_{IV} , representing the inputs (0,1), (1,0) and (1,1), will both induce a switch to the x polarization. The main idea behind LSR is that the current levels can be chosen such that the probability of the switchings is controlled by the noise strength.

Table 5.2 summarizes the relationship between the logic inputs, the current levels encoding these inputs, the expected laser polarization and its associated logical output. A main advantage of this scheme is that it allows to switch from AND to OR and vice versa, just by changing the cw value of the injection current, μ_m , while the modulation amplitude, $\Delta\mu$, can be kept constant. In other words, an appropriate choice of $\Delta\mu$, allows switching from regions (I, II, III) represented schematically in Fig. 3.10(d), that implement the AND operation, to regions (II, III, IV), that implement the OR operation, by changing μ_m only. A main drawback is that, for the AND operation, it does not allow very fast modulation. This is due to the fact that, as discussed previously in relation to Fig. 3.2(b), under fast modulation the PS for decreasing injection current disappears, and thus, there might be no level μ_I for which the y polarization turns on when the current decreases from levels μ_{II} or

Table 5.3: Encoding scheme II: Relationship between the logic inputs, the encoding current levels, the output polarization and the logic output for the AND and OR operations.

Logic inputs	AND:			OR:		
	Current	x/y	Logic output	Current	x/y	Logic output
(0,0)	μ_{IV}	x	0	μ_{II}	y	0
(1,0)/(0,1)	μ_{III}	x	0	μ_{III}	x	1
(1,1)	μ_{II}	y	1	μ_{IV}	x	1

μ_{III} to μ_I .

Table 5.3 illustrates the second encoding possibility. Here the current levels employed for the AND and for the OR operation are the same (they are those described for the OR operation previously). It should be noticed that for the AND operation the definition of the laser logic response changes: now a logic 0 is assigned if the x polarization is emitted, and a logic 1 if the y polarization is emitted. Also the encoding criterion changes, in the sense that the lower current level μ_{II} encodes the input (0, 0) for the OR operation, while it encodes the input (1, 1) for the AND operation; the highest current level μ_{IV} encodes the input (1, 1) for OR and encodes (0, 0) for AND; the middle level μ_{III} encodes (1,0) and (0, 1) for both operations. Because the AND and OR operations are implemented with the same three current levels, this scheme has the advantage of allowing fast modulation in both AND and OR operations, by preventing the drawback that at level μ_I the PS disappears for decreasing current, as discussed previously in section 3.1. In the following we will focus on the OR operation implemented with the encoding scheme described in Table 5.3 as the results apply also for the symmetric AND operation.

5.2 VCSEL-based stochastic logic gate via polarization bistability

Figures 5.3(a)-5.3(c) display the laser response for the same logic input and three values of the noise strength. The three current levels are such that the laser emits one polarization (x) for two of them, while for the third one, it can switch to the orthogonal polarization (y), in the presence of the right amount of noise. Figures 5.3(d)-5.3(f) display a detail of the dynamics to show the effects of the noise and the current modulation in the PS. With weak noise the PS is delayed with respect to the current modulation (Fig. 5.3(a) and 5.3(d)); with too strong noise, both polarizations are emitted simultaneously within the same bit (Fig. 5.3(c) and 5.3(f)). Therefore, the operation of the VCSEL as a logic gate depends on the noise strength, in good agreement with [142]. For an intermediate amount of noise (Fig. 5.3(b) and 5.3(e)), PS occurs a short time after the beginning of a bit while the noise is not strong enough to stimulate the emission of large intensities on both polarizations.

5.2.1 Analysis of the reliability of the stochastic logic gate

To evaluate the **reliability** of the VCSEL-based stochastic logic gate we calculate the success probability, i. e., the probability to obtain the desired logic output. For the two logic inputs we generate two random uncorrelated sequences of $N \geq 2^{10}$ bits and compute the success probability, P , as the ratio between the number of correct bits to the total number of bits. We define that a bit is correct, as follows. When x is the “right” output polarization (according to Table 5.3), we count a bit as correct if a given percentage (say, 80%) or more of the emitted power is emitted in the x polarization; if x is the “wrong” polarization, we count a bit as correct if a given percentage (say, 20%) or less of the emitted power is emitted in the x polarization.

Figure 5.4(a) displays P as a function of the noise strength, for three success criteria: 80%-20%, 90%-10% and 70%-30%. One can notice that there is a range of noise

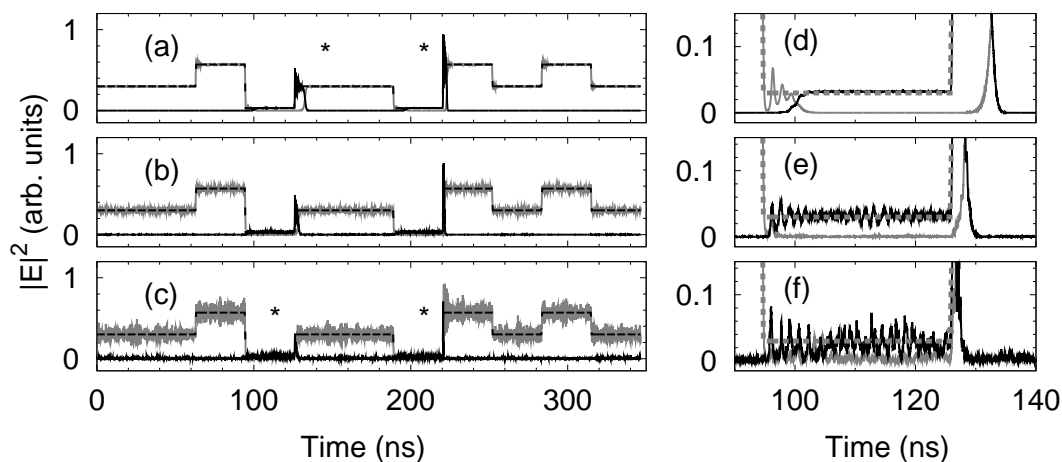


Figure 5.3: Laser response under aperiodic three-level current modulation. Time traces of the x polarization (gray), y polarization (black), and the injection current $\mu - 1$ (dashed) for different noise intensities: (a), (d) $D = 5 \times 10^{-7} \text{ ns}^{-1}$, (b), (e) $D = 4 \times 10^{-4} \text{ ns}^{-1}$ and (c), (f) $D = 6 \times 10^{-3} \text{ ns}^{-1}$. (d)-(f) display a detail of (a)-(c) to show the main errors in a bit. The asterisks mark the wrong bits.

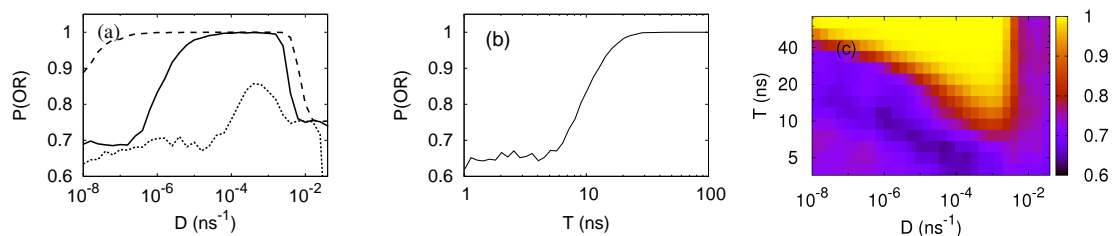


Figure 5.4: (a) Success probability P as a function of the noise strength, D , keeping fixed the bit time $T = 31.5 \text{ ns}$ and using a success criterion of 80%-20% (solid line), 90%-10% (dotted line) and 70%-30% (dashed line). (b) Success probability as a function of the bit time T for fixed noise strength $D = 4 \times 10^{-4} \text{ ns}^{-1}$. (c) Log-log color plot of the success probability P as a function of the noise intensity, D , and the the bit time, T . Other parameters as in Fig. 5.3.

strengths in which $P = 1$, and this noise range decreases (increases) when choosing a restrictive (a permissive) threshold for the emitted power in the x polarization. Within this noise range there is optimal noise-activated polarization switchings (the “inter-well” dynamics in the double-well potential picture) and optimal sensitivity to spontaneous emission in each polarization (the “intra-well” dynamics in the double-well potential picture). In the following we fix the success criterion to 80%-20%. It should be noticed that $P = 1$ occurs for noise strengths D that do not have to be unusually small, on the contrary, they are realistic values for semiconductor lasers, which typically have $D \sim 10^{-4} \text{ ns}^{-1}$.

The success probability depends strongly on the bit time, T , as shown in Fig. 5.4(b). Short bits ($\lesssim 5 \text{ ns}$) prevent logical operations because of the finite time needed for the polarization switching. For increasing T , the success probability grows monotonically until it saturates at $P = 1$ for long enough bits, for which the PS time is $\ll T$.

The interplay between the duration of the bit and the noise strength is illustrated in Fig. 5.4(c) and can be interpreted as follows. The time needed to escape from a potential well decreases with increasing noise [131]. Then, for weak noise, as D increases the escape time decreases and the probability of a correct response grows. On the other hand, too strong noise results in spontaneous emission in both polarizations and thus, for large enough noise, the power emitted in the “wrong” polarization grows above the threshold for detecting the response as correct, and thus, above a certain noise level the success probability decreases monotonously. The dependence of the success probability on the noise strength is due to the interplay of noise-induced escapes (inter-well stochastic dynamics) and spontaneous emission noise in the two polarizations (intra-well stochastic dynamics).

Figure 5.5(a) displays the success probability in the plane (D, μ_m) , for constant bit length and modulation amplitude. It can be seen that for small μ_m logic operations can not be obtained for any noise strength. Above $\mu_m \sim 1.27$, there is a noise range

in which P suddenly grows to 1. This value of μ_m is such that $\mu_{II} \geq \mu_{th,s} = 1$, i. e. the lasing threshold. As μ_m increases the noise region where $P = 1$ decreases until it disappears, due to the fact that for large μ_m the x polarization is stable in the three current levels, and switches to the y polarization are rare.

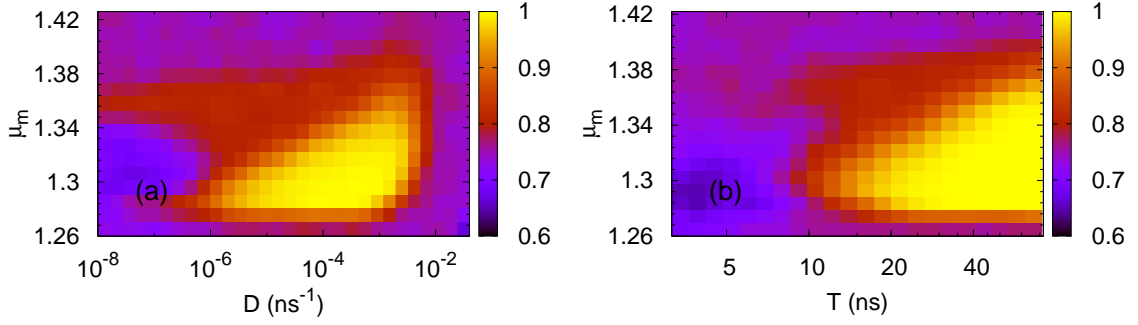


Figure 5.5: (a) Color plot of the success probability P as a function of the noise intensity, D , and the cw current value, μ_m , for fixed bit length $T = 31.5$ ns and modulation amplitude $\Delta\mu = 0.27$. (b) Color plot of the success probability P as a function of the bit time, T , and the cw current value, μ_m for fixed noise strength $D = 4 \times 10^{-4}$ ns $^{-1}$ and modulation amplitude $\Delta\mu = 0.27$. Other parameters are as in Fig. 5.3.

Figure 5.5(b) displays the success probability in the (T, μ_m) plane, keeping fixed the noise strength and modulation amplitude. It can be seen that $P = 1$ occurs when T is long enough and μ_m is within a range of values that depends on T . As discussed in relation to Fig. 5.5(a), if μ_m is too small the current level μ_{II} is at the lasing threshold or below and the y polarization turns-on slowly or does not turn on at all, depending on the modulation speed (if T is too small the y polarization does not turn on); on the other hand, if μ_m is too large, then the x polarization is stable in the three current levels and the y polarization rarely turns on.

Next, let us consider the influence of the modulation amplitude, $\Delta\mu$. Figure 5.6(a) displays the success probability in the $(D, \Delta\mu)$ plane, keeping constant the bit length and the modulation cw value. If $\Delta\mu$ is small the laser emits the same polarization

in the three current levels and the success probability is small, regardless of the noise strength. As $\Delta\mu$ increases there are polarization switchings and P increases, allowing for the correct logic response in a finite range of noise strengths. For large $\Delta\mu$, P decreases abruptly to small values, and this is again because the lowest current level is at threshold or below threshold [one can notice the similarities between Figs. 5.5(a) and 5.6(a)]. Similar considerations can be done in relation to Fig. 5.6(b), which displays the success probability in the $(T, \Delta\mu)$ plane, keeping constant the noise strength and the modulation cw value.

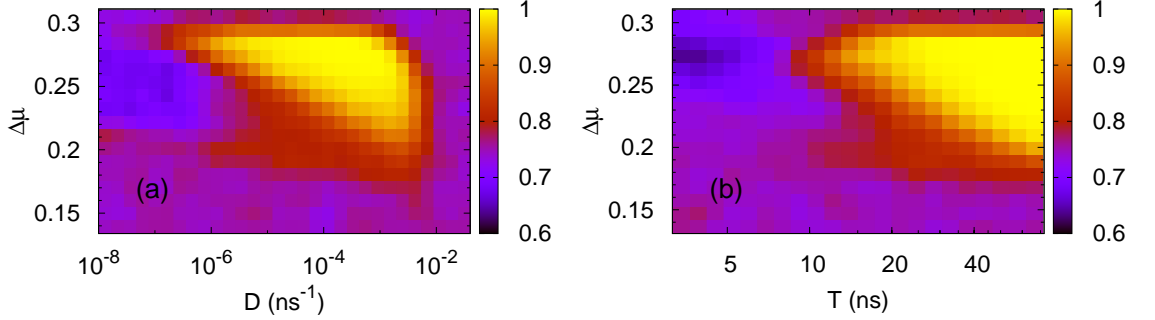


Figure 5.6: Color plot of the success probability P (a) as a function of the noise strength, D , and the current modulation amplitude, $\Delta\mu$, for a fixed $T = 31.5$ ns and (b) as a function of the bit time, T , and the current modulation amplitude, $\Delta\mu$, for a fixed $D = 4 \times 10^{-4}$ ns $^{-1}$. Other parameters are as in Fig. 5.3.

The step time, T_1 , and the rise/fall time, T_2 , are important parameters to obtain a correct logic response. In Fig. 5.7(a) we show the probability of success as a function of T_1 and T_2 . $P = 1$ requires that $T_1 \gg T_2$ (notice the doubly logarithmic scale). Furthermore, exist a minimum value of $T_1 \sim 10$ ns above which the probability of success grows to 1.

In practical applications, a VCSEL is often submitted to unwanted optical feedback due to external reflections. If the laser is sensitive enough, even a weak amount of reflected light can induce instabilities. To test the reliability of the LSR under

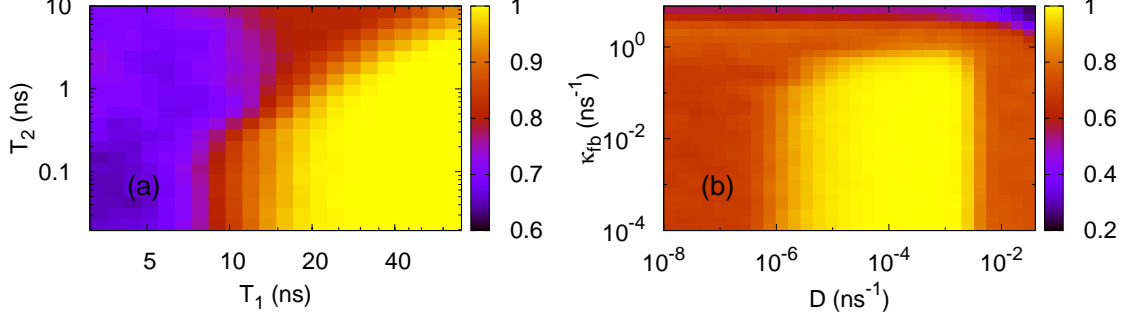


Figure 5.7: (a) Color plot of the success probability P as a function of the step time, T_1 , and the rise/fall time, T_2 , the noise level is $D = 4 \times 10^{-4}$ ns $^{-1}$. (b) P as a function of the noise strength, D , and the feedback strength, κ_{fb} . The bit time is $T = 31.5$ ns, the time delay is 3 ns. Other parameters are as in Fig. 5.3.

the influence of a weak external reflection, we included optical isotropic feedback in the model equations as in [182], and in Fig. 5.7(b) we present the results. By plotting the success probability in the parameter space (feedback strength, noise strength) we can see that the logic response is robust for weak feedback but the optimal response decreases progressively for increasing feedback strength.

We conclude this section with a discussion of the influence of various laser parameters. As it was previously mentioned, the logic stochastic resonance is a robust phenomenon in the sense that it occurs in parameter regions where the polarization switching is abrupt, and does not display polarization oscillations or coexistence. Figure 5.8(a) displays the success probability in the plane (γ_p, γ_a) . For negative or low linear dichroism, γ_a , only the x polarization is emitted. A probability equal to 1 is achieved in a region of positive γ_a values, and in a broad range of birefringence values, γ_p . Figure 5.8(b) displays the success probability in the plane (γ_s, γ_p) , and it can be seen that there is a wide region in which the success probability is equal to 1, provided that $\gamma_s \leq 100$. For large spin-flip rate, γ_s , only the polarization y is emitted and for small γ_s both polarizations are emitted simultaneously. Finally, Fig.

5.8(c) displays the success probability in the plane (γ_s, γ_a) where also a parameter region can be seen where $P = 1$.

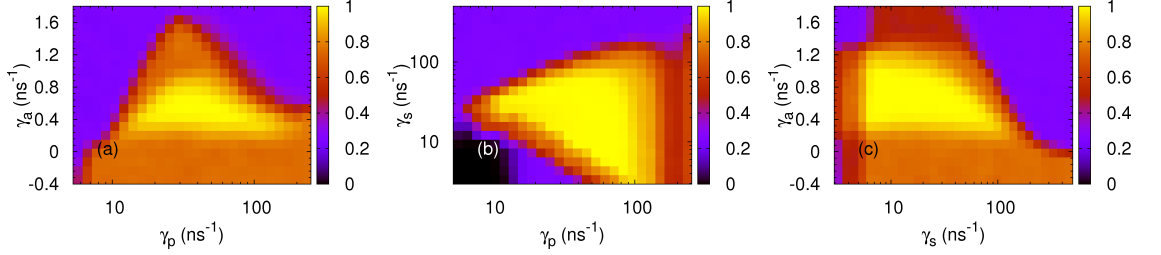


Figure 5.8: Influence of various model parameters. (a) Success probability in parameter plane (γ_a, γ_p) , for $\gamma_s = 50 \text{ ns}^{-1}$; (b) P in the parameter plane (γ_s, γ_p) , for $\gamma_a = 0.5 \text{ ns}^{-1}$; P in the parameter plane (γ_a, γ_s) , for $\gamma_p = 50 \text{ rad ns}^{-1}$. Other parameters are as in Fig. 5.3.

5.3 Conclusions and discussion

To summarize the results presented in this chapter, we have shown that a VCSEL can operate as a logic gate with a success probability equal to 1 in a wide region of noise strengths, which makes the VCSEL logic gate attractive for applications in systems subjected to noisy backgrounds.

The phenomenon is based on logic stochastic resonance (LSR) and can be well understood in the framework of the simple effective double well potential model for the two orthogonal polarizations emitted by the laser in a certain range of injection currents. The three levels of the pump current aperiodic signal that encode the four possible combinations of the two logic inputs are chosen such that the laser emits one polarization for two of them, while for the third one, it can switch to the orthogonal polarization, in the presence of the right amount of noise. Thus, the successful operation of a VCSEL as a stochastic logic gate is associated with optimal noise-activated polarization switchings (the “inter-well” dynamics) and optimal sensitivity

to spontaneous emission in each polarization (the “intra-well” dynamics) leading a range of optimal noise strength.

Our study has been based on the “bare” spin-flip model, which does not take into account several mechanisms that could be very relevant for the efficiency of current modulation to induce polarization switching (e. g., thermal effects, the excitation of higher-order transverse modes, carrier diffusion, etc. [183, 184]). The spin-flip model was recently extended to take into account temperature variations [185], and the study of the interplay of temperature and transverse spatial effects, based on the extended spin-flip model, is a natural continuation of the present work, that is left for future work. We think that these effects will not change the main conclusions of this work, but, since thermal effects are slow, they will probably increase the minimum bit time needed for achieving successful polarization switchings.

The mechanism underlying LSR has some similarities with that proposed in Ref. [186] for localizing a Brownian particle in one well of a symmetric bistable potential through the simultaneous action of two periodic inputs (one tilting the minima and the other one modulating the barrier height), and a random input. In Ref. [186] it was shown that the nonlinear mixing of these zero-mean signals was capable of localizing a Brownian particle in one well, and this could be a mechanism for controlling the polarization state of the light emitted by a VCSEL.

LSR also resembles the aperiodic stochastic resonance phenomenon, by which there is noise-assisted transmission of binary information [187, 188], and the information transmission, measured by the bit-error rate, exhibits a resonant-like behavior as a function of the noise strength.

The constructive role of noise in optical systems is nowadays a hot topic of research. Nonlinear self-filtering and amplification of noisy images, the with amplification occurring at the expense of noise through nonlinear coupling, was recently demonstrated in a self-focusing photorefractive medium [189]. The underlying mechanism (the energy exchange between the signal and the noise via nonlinear mixing),

depends on the system parameters and thus noise-assisted image recovery represents a novel type of dynamical stochastic resonance.

Our proposed implementation of a stochastic logic gate via a polarization-bistable VCSEL provides yet another example of the nontrivial and constructive role of noise in nonlinear optical systems. An attractive advantage of the VCSEL stochastic logic gate for practical applications is the relatively short bit time needed to produce the correct operation with probability equal to 1 (in our simulations, about 30-40 ns). In addition, the VCSEL stochastic logic gate is robust to stochastic external perturbations, in the sense that there is a wide range of realistic noise strengths in which the device gives a reliable and correct logic response. Moreover, its operation is also robust to variations of the laser parameters, in the sense that it does not require fine tuning of the parameters, but rather, there is a wide region of parameter values where the laser gives the correct logic response with $P = 1$.

Chapter 6

Transient LFFs in a semiconductor laser with optical feedback

The aim of this chapter is to characterize the statistical features of the transient LFF regime of a semiconductor laser with optical feedback. The **transient** time required for a dynamical system to evolve from initial conditions to a stable attractor can be due to, depending on the dynamical system, simple relaxation oscillations as in the damped oscillator or more complex (even chaotic) dynamics. A pioneer study of the **chaotic transients** that results from the collision of a chaotic attractor and an unstable fixed point or unstable periodic orbit was done by Grebogi, Ott and Yorke [190]. The chaotic attractor changes suddenly and the sustained chaotic dynamics becomes unstable in such a way that the system eventually reaches a stable steady state or a stable attractor. In many cases, the chaotic attractor keeps its appearance before and after the collision but its stability changes. In this chapter we study this type of phenomenon in a laser with optical feedback.

As discussed in Section 3.2, a well known optical feedback-induced instability is the so-called low frequency fluctuation (LFF) regime in which the laser intensity displays fast picosecond pulses. These pulses, when observed with a low-pass filter

(as occurs in experiments, where photodetectors have a limited bandwidth), are seen as a sequence of sudden dropouts followed by a gradual recovery.

Many studies in the literature, discussed in detail in Sec. 3.2, have tried to address the question of whether the initiation of LFF dropouts, and the subsequent recovery, are deterministic or stochastic processes. In this chapter we study in detail the statistical features of the **transient LFF dropouts**, and the underlying unstable chaotic attractor [191, 192]. With this aim, we simulate the laser turn-on by choosing *random* initial conditions in the vicinity of the solitary laser steady state, and integrate numerically the resulting trajectory. The LFF lifetime, T_{LFF} , is defined as the time taken by the intensity fluctuations to decrease below a chosen threshold, which occurs when the trajectory falls into the basin of attraction of one of the stable ECMs. We find that typical noise levels do not significantly affect the average transient time nor its probability distribution function (PDF): both the deterministic model, with no noise source included in the rate equations, and the stochastic model, with typical values of the spontaneous emission noise strength, predict similar $\langle T_{\text{LFF}} \rangle$ and PDF. Strong enough noise, however, induces escapes from the stable ECM, leading the laser output to display coexistence of LFFs and stable emission, similar to experimental observations [47].

We also show that the nonlinear gain saturation coefficient, ε , which is included phenomenologically in the LK model to represent a variety of saturation mechanisms such as carrier heating, carrier diffusion and spatial hole burning, is a key parameter in determining the duration of the LFF transient: when increasing ε both the average transient time $\langle T_{\text{LFF}} \rangle$ and the probability of noise-induced escapes from the stable ECM increase. Therefore, our results suggest that the LFFs observed experimentally can be, at least in part, sustained by the interplay of noise and the various nonlinear effects which are phenomenologically represented by the gain saturation coefficient.

Some characteristics of the LFF dynamics, in particular, the statistical properties of time intervals between power dropouts, can be explained by a rate-equation model

proposed by Eguia, Mindlin and Giudici (EMG model) [124], which supports the scenario that the laser behaves as an excitable system and that the LFFs are induced by noise. The dependence of the shape of the PDF of inter-dropout intervals on the pump current or the feedback strength were shown to be equivalent to variations produced by the two parameters of the EMG model [125]. Moreover, in [193] the periodic “spike” patterns generated experimentally under external periodic forcing were compared with the solutions of the EGM model, and it was shown that the topological organization of the experimentally observed periodic orbits was equivalent, in the parameter region explored, to the one displayed by the model solutions. The limits of the excitable LFF behavior, and thus, the region of validity of the EMG model, was studied in [126], where it was shown that excitability deteriorates in the parameter region where there is a high probability of stable emission; in this region of “coexistence” the laser dynamics can be separated into stable and bursting states.

The EMG model is low-dimensional, and thus it offers a good control to test the influence of the delay-induced high-dimensionality of the LK model on the statistics of the LFF transient time. Thus in this chapter we also investigate the transient dynamics predicted by the EMG model with parameters in the excitable region. We show that by choosing appropriate initial conditions, a qualitatively good agreement is found with the features of the transient dynamics predicted by the LK model. However, in this case noise does affect the shape of the PDF of LFF transient times, which indicates the importance of the high-dimensionality of the unstable chaotic attractor of the LK model in determining the transient time statistics.

This chapter is organized as follows: Section 6.1 describes the LK model and discusses the initial conditions chosen for the simulations. Sections 6.1.1 and 6.1.2 present the numerical results, and discuss the statistical features of the LFF transient lifetime in terms of various parameters. Section 6.1.3 presents the results of the control simulation of the low-dimensional EMG model. Finally, Section 6.2 contains a summary of results and the conclusions.

6.1 Transient Low Frequency Fluctuations in the LK model

We first describe the dynamics of a single-mode semiconductor laser with optical feedback by means of the well-known Lang-Kobayashi (LK) delay-differential rate equations according to the description in section 2.1 for the slowly-varying complex amplitude of the electric field, E , and the carrier number, N . To integrate the model, rate equations (2.5) and (2.6) we have to specify the initial conditions, which we choose to correspond to the steady state of the solitary laser plus a small random term:

$$E(t) = E_s e^{i\phi_0} + \eta \xi(t), \quad -\tau \leq t \leq 0 \quad (6.1)$$

$$N(0) = N_s + \rho \zeta, \quad (6.2)$$

where E_s and N_s are the stationary solutions of the system, which correspond, for a normalized injection current μ below the solitary laser threshold, to the off state, $E_s = 0$ and $N_s = \mu$, while if $\mu > \mu_{th}$ they correspond to $E_s = \sqrt{\mu - 1}$ and $N_s = 1$ (that can be obtained from eqs. (2.10) and (2.11) by considering $\kappa_{fb} = 0$ and $\varepsilon = 0$) and ϕ_0 which is a random initial phase.

Alternatively, one could always choose as initial condition the off state of the laser, regardless of the value of the injection current. As discussed below, we find that the results are robust with respect to the specific choice of the initial condition. Unless otherwise explicitly stated, we integrated the LK model with the parameter values given in Table 6.1, using the stochastic Heun method with an integration time step of 0.8 ps. The simulations were verified using smaller integration steps and the Euler integration method, with which we obtained similar results.

Table 6.1: Typical parameter values of the LK model described by Eqs. (2.5) and (2.6).

Description	Symbol	Value
Linewidth enhancement factor	α	3
Field decay rate	k	300 ns ⁻¹
Feedback strength	κ_{fb}	30 ns ⁻¹
External round-trip time	τ	6.667 ns
Feedback phase	$\omega_0\tau$	0 rad
Carrier population decay rate	γ_N	1 ns ⁻¹
Normalized injection current	μ	1.02
Gain saturation coefficient	ε	0
Spontaneous emission noise strength	D	10 ⁻⁴ ns ⁻¹
Noise intensity (field initial condition)	η	10 ⁻³
Noise intensity (carriers initial condition)	ρ	10 ⁻³

6.1.1 Probability distribution of the stochastic transient time

As discussed in Sec. 3.2, simulations of the LK model show that close to the solitary laser threshold and with moderately strong optical feedback, the laser intensity displays fast picosecond pulses, which when subject to a low-pass filter (as occurs in experiments, where photodetectors have a limiting bandwidth), transform into a collection of sudden dropouts, characteristic of the LFF dynamics, as shown in Fig. 6.1. All through this section a filter with a cutoff frequency of 120 MHz will be applied to the intensity time trace, given by $|E(t)|^2$.

With initial conditions such that the laser is emitting on the stable state without feedback, at $t = 0$ the optical feedback is turned on. As a result the laser begins to experience intensity dropouts during a certain time interval $0 < t < T_{\text{LFF}}$, as shown in Fig. 6.1(a). For $t \geq T_{\text{LFF}}$ the laser output is stable, since the trajectory

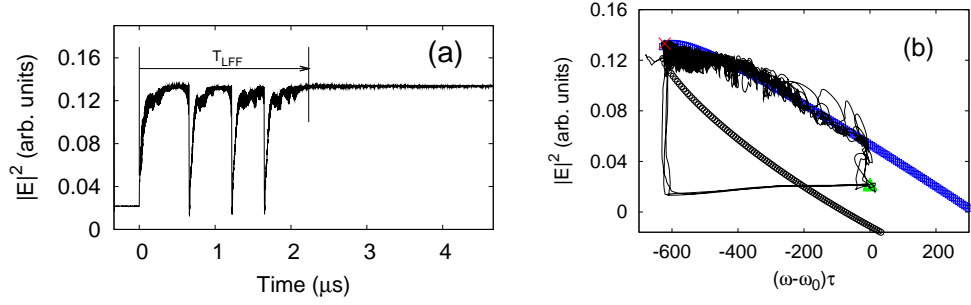


Figure 6.1: (a) A typical time trace for the filtered intensity, displaying three LFF dropouts. A filter with a cut-off frequency of 120MHz is used to obtain this time trace. (b) Filtered global trajectory in the phase space of intensity, $|E|^2$, and phase difference of the optical field, $(\omega - \omega_0)\tau$, for the trajectory shown in (a); squares are the modes (upper branch of the ellipse) and circles are the anti-modes (lower branch of the ellipse). The triangle and the cross mark the initial conditions and the final state respectively.

falls into the basin of attraction of one of the stable ECMs [fixed points given by Eqs. (2.9)-(2.11)], and remains trapped there provided the noise strength is not too large.

The final state of the laser is given by one of the coexisting ECMs. These ECMs are shown in Fig. 6.1(b) in the phase space of intensity and phase difference. A typical global trajectory in this phase space begins at $(\omega - \omega_0)\tau = 0$ (the triangle in Fig. 6.1(b)). Then the trajectory is attracted to the stable ECMs for low values of the phase difference and high values of the intensity, but in this region the system can reach the vicinity of one of the unstable ECMs (anti-modes) and it can be ejected towards the phase-space region of low intensities, after which the process starts again. The LFF dropout dynamics ends when the system's trajectory finds one of the stable ECMs (the cross in Fig. 6.1(b)).

The **lifetime** of the transient LFF dynamics, T_{LFF} , is defined as the time interval during which the intensity fluctuations, measured as the standard deviation calcu-

lated in a time window ΔT , are above a certain threshold, chosen here to be 2% of the average intensity. To make sure that the system has reached an asymptotic behavior (in the vicinity of a fixed point), we use a time window $\Delta T = 1800$ ns, much larger than the characteristic time scale of the fast intensity pulsations. The total integration time is of the order of 10-100 ms, which thus correspond to the longest transient times that we can compute.

The duration of the LFF transient depends on the specific realization of the random initial condition, and can strongly deviate from its mean value. Figure 6.2(a) displays the probability distribution function (PDF) of the transient time, T_{LFF} . The shape of this distribution can be understood as follows: the system has a zero probability of finding a stable ECM in a very short transient time T_{LFF} , due to the finite amount of time it takes to go from the initial condition (near the solitary laser's steady state) to the phase space region where the stable ECMs are located. The largest peak in the PDF corresponds to this single-rise travel time, which we refer to as T_1 (typically, $T_1 < 1 \mu\text{s}$ depending on parameters). We show this trajectory in the top trace of Fig. 6.2(b). Note that there is a large probability that the system finds a stable ECM the first time it is in the region of the phase space where the stable ECMs are located. The secondary maximum of the PDF (T_2) corresponds to trajectories in which the system finds a stable ECM during its second visit to the area near it. In this case the transient dynamics contains one dropout, as shown in the bottom trace of Fig. 6.2(b).

In between T_1 and T_2 the system has a small probability of finding a stable ECM because it is in another region of the phase space (i.e., in the recovery process after the dropout). For larger values of T_{LFF} the PDF decays exponentially, as is expected in chaotic transients [190]. The inset of Fig. 6.2(a) plots the PDF in both the presence and absence of noise. The two distributions overlap, which suggests that the average transient time, $\langle T_{\text{LFF}} \rangle$, is not affected by noise. We verify this fact in Fig. 6.3(a), which shows the average duration of the transition from LFFs to a stable output as a function of the noise strength, D , for different values of the

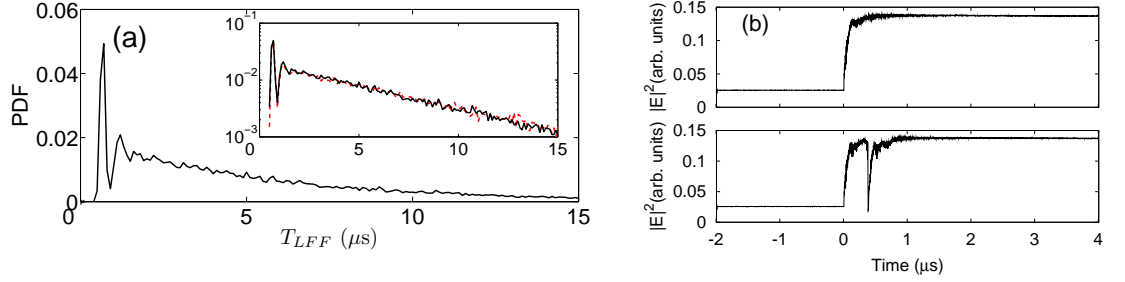


Figure 6.2: (a) Probability distribution function (PDF) of the transient time T_{LFF} calculated from 30000 realizations of the stochastic initial condition. Inset, PDF with vertical logarithmic scale to show the exponential tails with noise (solid line) and without noise (dashed, red). (b) Intensity time traces corresponding to the two maxima of the PDF shown in (a).

injection current and feedback strength. In all cases the average transient time is not significantly affected by noise, and is approximately equal to the noise-free case.

The transient can be understood as a sequence of N_{LFF} dropouts that are spaced at an average time $\langle T \rangle$. These values are shown in the Fig. 6.3(b), where we plot both the average time between dropouts per transient ($\langle T \rangle$, left axis) and the average number of dropouts per transient ($\langle N_{LFF} \rangle$, right axis). For large enough number of dropouts, the product of these two quantities corresponds to the average transient time, i.e. $\langle T_{LFF} \rangle = \langle N_{LFF} \rangle \langle T \rangle$ which suggests that the two variables are independent. It can be seen in Fig. 6.3(b) where neither $\langle N_{LFF} \rangle$ nor $\langle T \rangle$ depend on the noise intensity.

It will be shown below that the T_{LFF} distribution strongly depends on the other laser parameters α and ε , besides μ ; therefore, it could be expected that for different values of these parameters the T_{LFF} distribution is not so insensitive to noise. To check this point we performed extensive simulations for other values of α and ε , and we present in Fig. 6.4(a) and (b) two examples of the results. Again, it can be observed that the average duration of the transient time does not significantly change with noise strength. Therefore, at least in the parameter region explored,

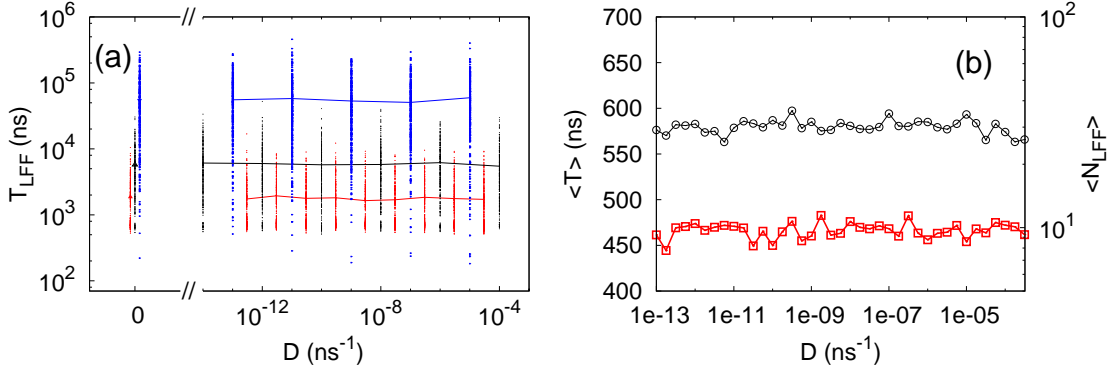


Figure 6.3: (a) Transient time (dots) and average transient time, $\langle T_{\text{LFF}} \rangle$ (solid lines) for 300 realizations of the stochastic initial conditions as a function of the noise intensity for different values of the injection current and the feedback strength. $\varepsilon = 0.0$, $\alpha = 3$, and additionally, from top to bottom: $\mu = 1.02$, $\kappa_{fb} = 15 \text{ ns}^{-1}$ (blue); $\mu = 1.02$, $\kappa_{fb} = 30 \text{ ns}^{-1}$ (black); $\mu = 0.98$, $\kappa_{fb} = 30 \text{ ns}^{-1}$ (red). Other parameters are as in Table 6.1. (b) Average time interval between consecutive dropouts (circles, left axis) and average number of dropouts per transient (squares, right axis) as a function of the noise intensity for $\mu = 1.02$, $\kappa_{fb} = 30 \text{ ns}^{-1}$ (black); note the logarithmic scale in the right axis.

we can conclude that the duration of the transient dynamics is not qualitatively affected by random fluctuations. It is important to remark that we have limited ourselves to explore the parameter region where the average transient time is not too long; for larger values of μ , α or τ the simulations require too long and unpractical computational times. Therefore, we cannot exclude that for larger values of μ , α or τ the noise has an effect on the transient time.

6.1.2 Effect of the parameters of the LK model on the stochastic duration of the LFF transient

To investigate how the LFF lifetime depends on the parameters of the system, we computed the average transient time, $\langle T_{\text{LFF}} \rangle$, for varying values of different pa-

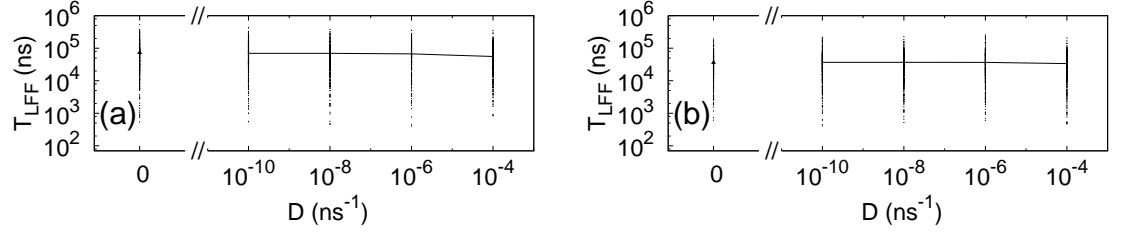


Figure 6.4: Transient time (dots) and average transient time, $\langle T_{LFF} \rangle$ (solid lines) for 300 realizations of the stochastic initial conditions as a function of the noise intensity for different values of the gain saturation and the α . (a) $\varepsilon = 0.06$, $\alpha = 3$, $\mu = 1.02$, $\kappa_{fb} = 30$ ns $^{-1}$. (b) $\varepsilon = 0.1$, $\alpha = 2.6$, $\mu = 1.02$, $\kappa_{fb} = 30$ ns $^{-1}$. Other parameters are as in Table 6.1.

rameters, classified in terms of laser parameters (ε , α and μ) and optical feedback parameters (τ , κ_{fb} and ω_0).

An interesting effect is provided by the gain saturation coefficient, ε . When increasing ε in a realistic range the average transient time $\langle T_{LFF} \rangle$ increases three orders of magnitude, as shown in Fig. 6.5(a). In fact, nonlinear gain saturation acts as a coupling between the field and the phase in a way similar to the linewidth enhancement factor, α , whose effect is displayed in Fig. 6.5(b).

Recently, Torcini *et al.* [107] analyzed the relationship between the stability of the ECMs and the length of the LFF transient, and derived an analytical expression for estimating the transient time in relation to the eigenvalues of the stable ECMs. In the specific range of parameters examined in [107], $\mu < \mu_{th}$ and $\alpha < 4$, a periodic variation of $\langle T_{LFF} \rangle$ with α was found [see the inset in Fig. 6.5(b)], which was well understood in terms of the analytical expression derived. However, the agreement worsens for bias currents above the solitary threshold, which is the parameter range examined here.

Plots (c) and (d) in Fig. 6.5 represents the contributions of the average dropout number, $\langle N_{LFF} \rangle$, and the average inter-dropout time, $\langle T \rangle$, to the transient time. The figure shows that $\langle N_{LFF} \rangle$ increases monotonically with both laser parameters

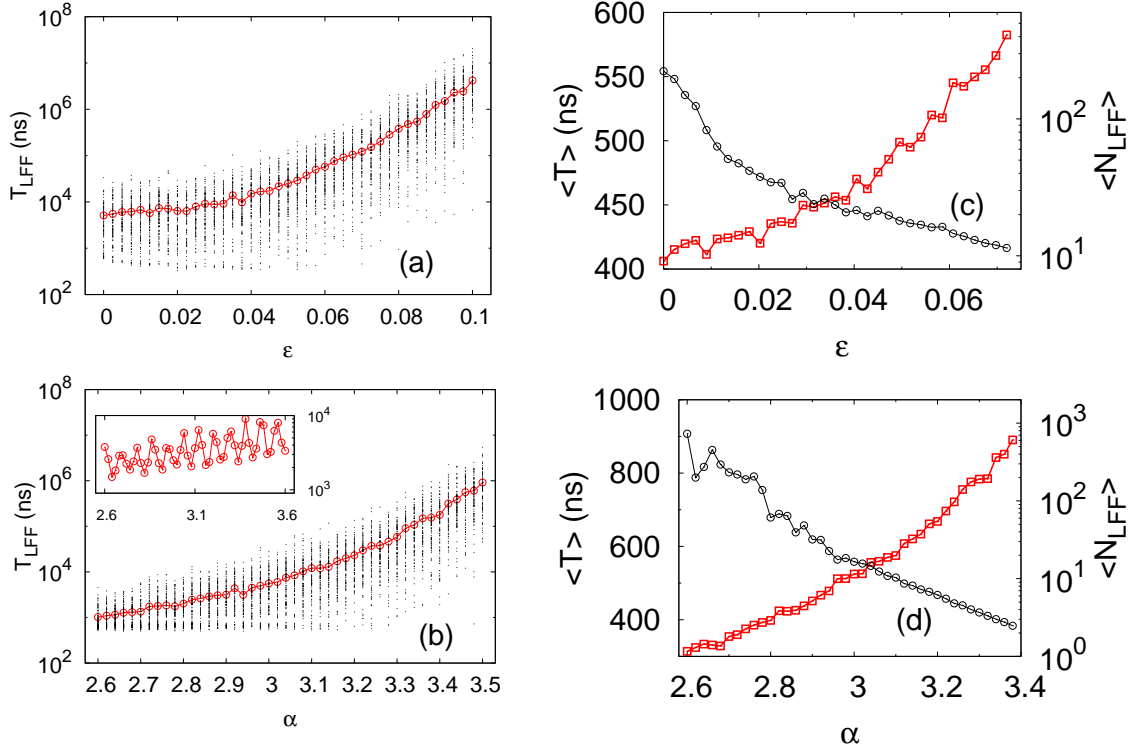


Figure 6.5: Transient time (dots) and average transient time, $\langle T_{LFF} \rangle$ (red circles), for 100 random realizations of the initial conditions, as a function of (a) the gain saturation coefficient with $\alpha = 3$ and $\mu = 1.02$, (b) the linewidth enhancement factor with $\mu = 1.02$ and $\epsilon = 0$. In the inset on figure (b), we show results for the same parameters as in [107]. (c) and (d) The panels on the right column show the dependence of the average time interval between consecutive dropouts (circles, left axis) and average number of dropouts per transient (squares, right axis) on the same laser parameters as in (a) and (b); note the logarithmic scale in the right axis. Other parameters are $\kappa_{fb} = 30 \text{ ns}^{-1}$, $\tau = 6.667 \text{ ns}$ and $D = 10^{-4} \text{ ns}^{-1}$.

considered, while $\langle T \rangle$ decreases. Note that even though the two contributors to $\langle T_{LFF} \rangle$, i.e. $\langle N_{LFF} \rangle$ and $\langle T \rangle$, behave complementarily, their trends do not cancel out since the increase of $\langle N_{LFF} \rangle$ is supra-exponential for the three parameters, while $\langle T \rangle$ decreases only linearly [cf the different scaling of the left and right y-axes in

Figs. 6.5(c) and (d)].

The influence of the injection current parameter, μ , is displayed in Fig. 6.6(a), which shows that the transient time $\langle T_{\text{LFF}} \rangle$ also increases with μ . Our results are consistent with those in [107], where it was shown that the transient time increases with both α and μ . These figures also show the existence of a minimum transient time, as discussed previously in relation to Fig. 6.2(a).

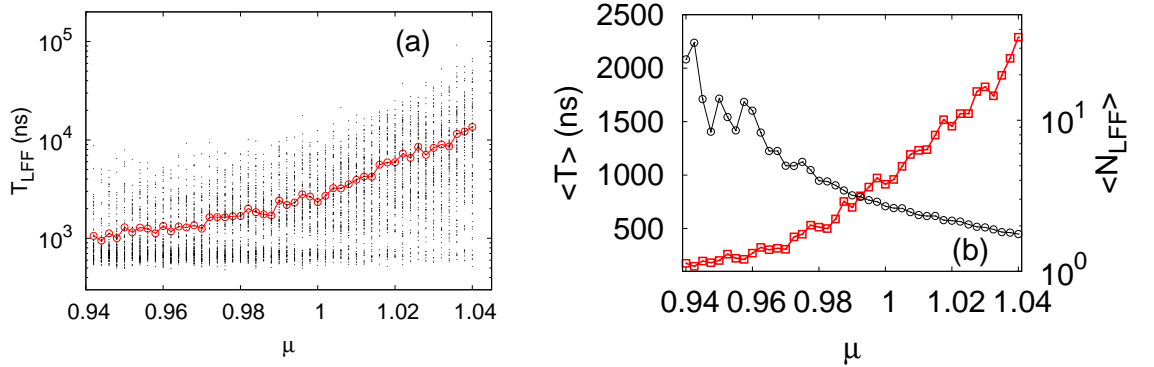


Figure 6.6: (a) Transient time (dots) and average transient time, $\langle T_{\text{LFF}} \rangle$ (red circles), for 100 random realizations of the initial conditions, as a function of the injection current with $\alpha = 3$ and $\varepsilon = 0$. (b) Dependence of the average time interval between consecutive dropouts (circles, left axis) and average number of dropouts per transient (squares, right axis) on the same laser parameters as in (a); note the logarithmic scale in the right axis. Other parameters are $\kappa_{fb} = 30 \text{ ns}^{-1}$, $\tau = 6.667 \text{ ns}$ and $D = 10^{-4} \text{ ns}^{-1}$.

The same discussion done for Fig. 6.5(c) and (d) can also be applied to Fig. 6.6(b). In particular, the decrease in the time interval between consecutive dropouts, $\langle T \rangle$, for increasing injection current μ agrees qualitatively well with the well-known behavior observed experimentally in the sustained LFF regime [117, 120] also shown in Fig. 3.7(a).

The influence of the delay time τ is depicted in Fig. 6.7(a). For small delays the dynamics is not chaotic and all realizations of the stochastic initial conditions lead to almost the same transient time. As we increase τ , the average transient time $\langle T_{\text{LFF}} \rangle$

increases nearly exponentially up to the maximum delay studied. This behavior is a consequence of the nearly exponential increase of $\langle N_{LFF} \rangle$ [Fig. 6.7(c)] and is reinforced by $\langle T \rangle$, which in this case also increases monotonically with the feedback delay time. This latter effect is in qualitatively well agreement with Refs. [119, 120] (see Fig. 3.7(b)).

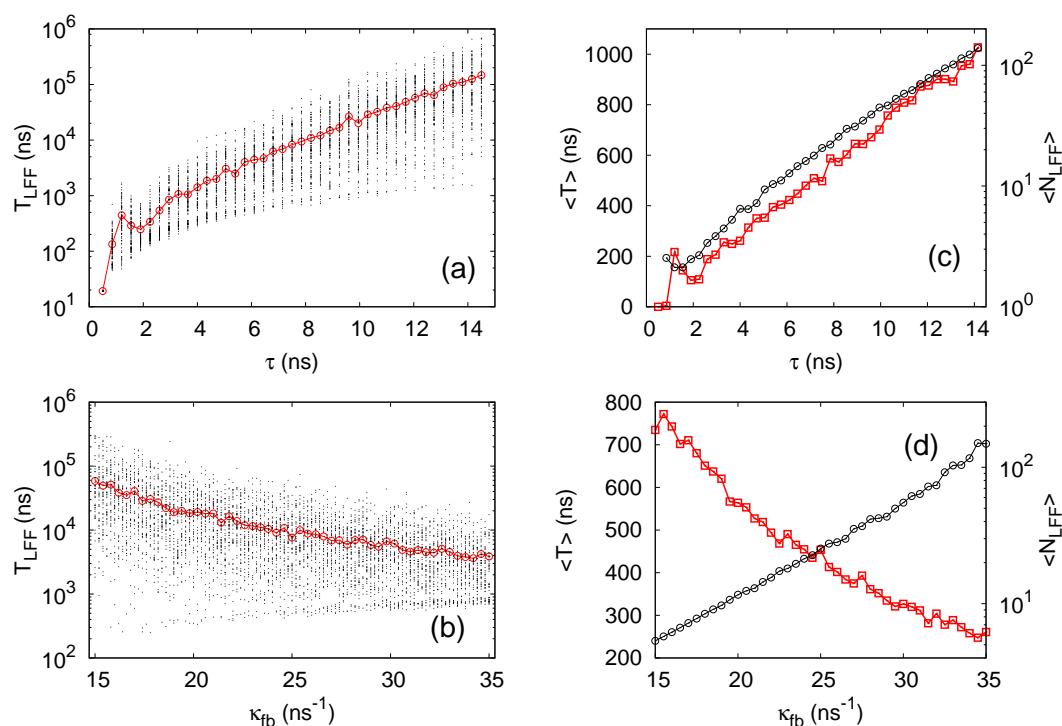


Figure 6.7: Transient time (dots) and average transient time, $\langle T_{LFF} \rangle$ (circles) for 100 stochastic realizations of the initial conditions, as a function of (a) delay time with $\kappa_{fb} = 30 \text{ ns}^{-1}$ and $\omega_0\tau = 0$, (b) the feedback strength with $\tau = 6.667 \text{ ns}$ and $\omega_0\tau = 0$. The panels on the right column show the dependence of the average time interval between consecutive dropouts (circles, left axis) and average number of dropouts per transient (squares, right axis) on the same laser parameters as in (a) and (b); note the logarithmic scale in the right axis. Other parameters are $\varepsilon = 0$, $\alpha = 3$, $\mu = 1.02$ and $D = 10^{-4} \text{ ns}^{-1}$.

For increasing feedback strength, κ_{fb} , the duration $\langle T_{LFF} \rangle$ of the transient decreases, as depicted in Fig. 6.7(b). Although the parameter region is different, it is

interesting to compare this result with [194], where the authors show that for low feedback levels, i. e. for a small number of ECMs, sustained and transient dynamics alternate for increasing κ_{fb} .

Analyzing $\langle N_{LFF} \rangle$ and $\langle T \rangle$ in Fig. 6.7(d) we see that these quantities depend on κ_{fb} oppositely to the laser parameters (Fig. 6.5 and 6.6). However, $\langle N_{LFF} \rangle$ still dominates the behavior of the transient time, since for increasing feedback strength it decreases nearly exponentially, while $\langle T \rangle$ increases nearly linearly. The latter behavior is in qualitative good agreement with Refs. [118, 120] also shown in Fig. 3.7(c).

Another delay parameter is the feedback phase, $\omega_0\tau$. Increasing $\omega_0\tau$, pairs of modes and anti-modes are created far from the chaotic attractor, and they are destructed in the region of phase space where the stable ECMs are. Varying $\omega_0\tau$ also changes the stability of the ECMs with periodicity of 2π . Then it could be expected that at least one of the ECMs collides with the chaotic attractor and it may be reflected in $\langle T_{LFF} \rangle$ with the same periodicity. Figure 6.8 shows that varying $\omega_0\tau$ does not change the average transient time in a significant way (neither $\langle T \rangle$ or $\langle N_{LFF} \rangle$ change significantly). This result indicates that the stabilities of the LFF dynamics and of the ECMs are not directly related, at least for the parameter values examined here, for which there are global trajectories in phase space.

Even after the laser has settled around the stable ECM once the chaotic transient has finished, strong enough noise can lead the trajectory to eventually escape and display another set of LFF dropouts, as shown in Fig. 6.9(a). The ensuing transient LFF regime is similar to the one studied above, in which the laser was off at $t = 0$, when the feedback was turned on. These two situations only differ in the choice of initial conditions, which as discussed above lead to the same distribution of LFF durations. Noise-induced escape of the basin of attraction of the stable ECMs was studied in [107] for large enough noise and interpreted in terms of the Kramers rate. This provides the system with two time scales that can be tuned separately and

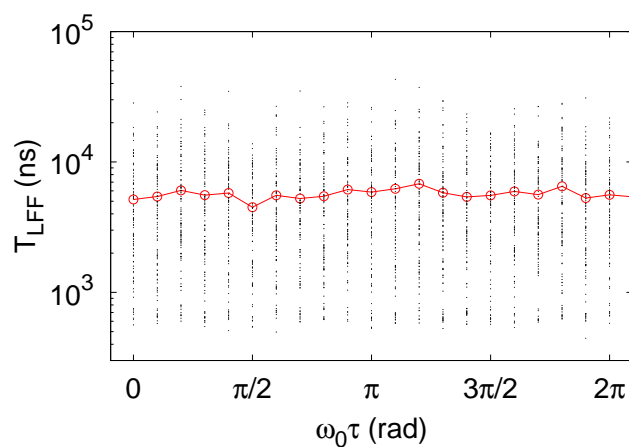


Figure 6.8: Transient time (dots) and average transient time, $\langle T_{\text{LFF}} \rangle$ (circles, red) for 100 stochastic realizations of the initial conditions, as a function of the feedback phase with $\tau = 6.667$ ns and $\kappa_{fb} = 30$ ns $^{-1}$. Other parameters are $\varepsilon = 0$, $\alpha = 3$, $\mu = 1.02$ and $D = 10^{-4}$ ns $^{-1}$.

could lead to resonant effects such as stochastic or coherent resonance. One of these time scales (the excursion duration) is deterministic, as shown in Fig. 6.3, and the other one (the escape time) is stochastic, as shown in [107].

Finally, we note that if nonlinear gain saturation is included in the simulations, the probability of noise-induced escape away from the stable ECMs substantially increases, as shown in Fig. 6.9(b).

6.1.3 Transients in a low-dimensional phenomenological model

Eguia, Mindlin and Giudici proposed a phenomenological model (EMG model) that describes the dynamics of the *time-averaged* laser intensity, i.e., not the fast picosecond pulses but the slower dropouts [124]. The model is defined by the following set

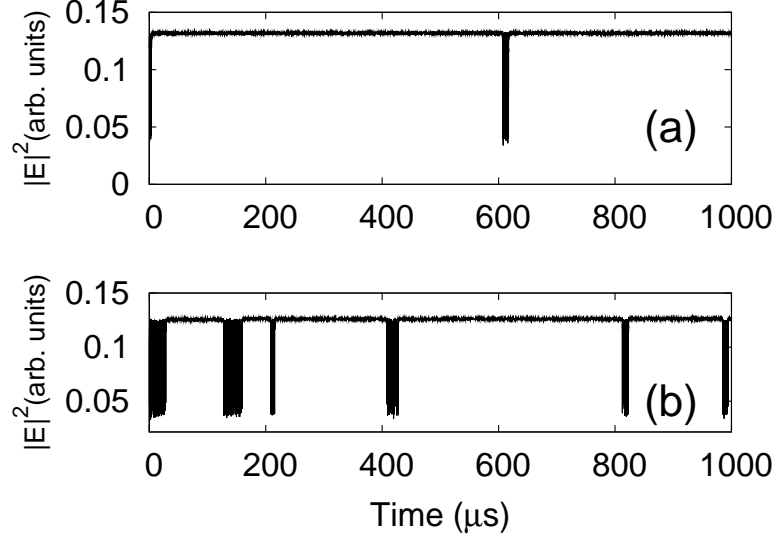


Figure 6.9: (a) Intensity time trace for relatively large noise strength ($\epsilon = 0$, $D = 10^{-2}$ ns $^{-1}$). (b) Same as in (a) with $\epsilon = 0.05$

of ordinary differential equations:

$$\frac{dx}{dt} = y + \sqrt{d}\xi(t), \quad (6.3)$$

$$\frac{dy}{dt} = x - y - x^3 + xy + \epsilon_1 + \epsilon_2 x^2, \quad (6.4)$$

where ϵ_1 and ϵ_2 are two control parameters, d is the noise strength and $\xi(t)$ is a Gaussian white noise.

We choose parameters for which the model operates in an excitable regime, with three fixed points (x_s, y_s) with $y_s = 0$ and x_s being a solution of the third order equation $x - x^3 + \epsilon_1 + \epsilon_2 x^2 = 0$. The three fixed points are a stable focus, a saddle point, and an unstable focus (repeller), shown as symbols in Fig. 6.10(a). In a previous work, Yacomotti *et al.* [125] associated the parameter ϵ_1 to the bias current and ϵ_2 to the feedback strength. Exploiting this similarity we chose the initial conditions as similar as possible to the ones described in the previous Sections. Specifically, we chose random initial conditions for $\epsilon_2 = 0$ inside the region limited

by the stable manifold of the saddle point and the repeller:

$$x(t = 0) = x_0 + r\xi \quad (6.5)$$

$$y(t = 0) = y_0 + r\zeta \quad (6.6)$$

where $x_0 = 0.4$, $y_0 = 0$ and $r = 0.25$. ξ and ζ are uncorrelated Gaussian random numbers.

We integrated the EMG model using the stochastic Heun method with an integration time step of $8 \cdot 10^{-3}$ arbitrary units. Some characteristics of the LFF dynamics can be satisfactorily reproduced by the EMG model. In particular, the transient regime can be reproduced approximately, as shown in Fig. 6.10(b).

The distribution of transient times obtained in this case is plotted in Fig. 6.11, and shows a qualitative agreement with the results found in the LK model above. In this case, however, noise does play an important role, changing qualitatively the shape of the distribution for large transient times, as shown in the inset of Fig. 6.11. In order to understand how this distribution function arises and why noise plays a more important role in this case, we have examined the dependence of the transient time on the initial conditions for the deterministic model. This dependence is shown in color coding in Fig. 6.10(a).

The results presented in this figure reveal that the initial conditions leading to a given transient time have a well-defined structure in phase space, with the transient time being larger the closer the initial conditions are to the stable manifold of the saddle (white dashed line in the figure). In that case, a substantial slowdown is experienced by the trajectory as it passes nearby the saddle, leading to the exponential time in the transient time distribution. Noise seems to increase the probability that trajectories encounter this area of phase space, thus increasing the fraction of large transient times. Thus, in this region, the transient time depends strongly on the noise fluctuations, and unlike in the LK model [Fig. 6.2(a)], long transient times are induced by noise.

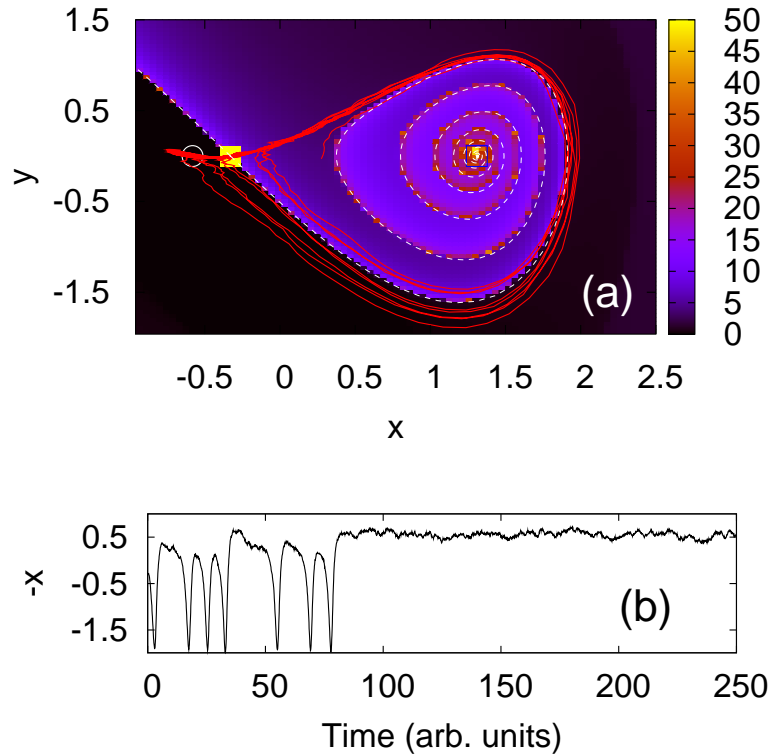


Figure 6.10: (a) Phase space portrait of the EMG model. For the parameters chosen the system is in an excitable regime, exhibiting a stable node (green circle), a saddle point (yellow full square) and a repeller (blue open square). The background color represents the transient time of a trajectory starting at that point in phase space in the absence of noise. The white dashed line represents the stable manifold of the saddle point, and the red solid line shows a typical trajectory with noise. (b) Time trace of the EMG model corresponding to the red trajectory shown in plot (a), for the variable $-x(t)$. The minus sign is chosen to compare with Fig. 6.1. Noise intensity is $d = 2 \cdot 10^{-3}$, and the deterministic parameters of the model are $\epsilon_1 = 0.25$ and $\epsilon_2 = 0.4$.

6.2 Conclusions and discussion

We have studied numerically the transient LFF dynamics of a semiconductor laser with optical feedback using the well known Lang-Kobayashi model. We defined the

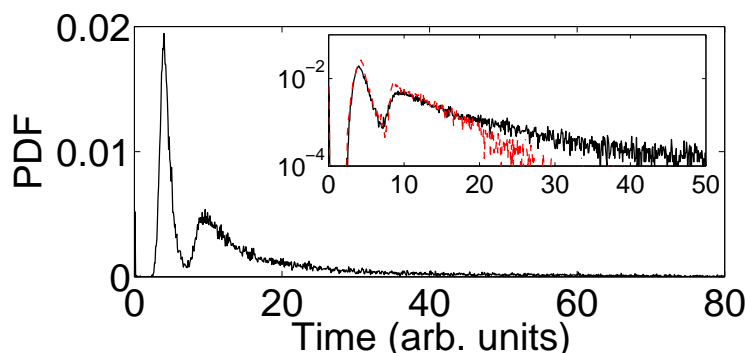


Figure 6.11: Probability distribution function for the transient time for the EMG model. Parameters are as in Fig. 6.10. Inset, the same plot with vertical logarithmic scale with noise (solid) and without noise (red dashed).

transient time as the time taken by the intensity fluctuations to decrease below a chosen threshold, which occurs when the system leaves the chaotic LFF attractor and falls into one of the stable fixed points (the so-called external cavity modes, ECMs). The probability distribution function (PDF) of the transient time has an exponential tail that is characteristic of chaotic transients, and there is a minimum transient time due to the finite amount of time needed to go from the fixed point of the solitary laser to one of the stable ECMs of the laser with feedback.

We found that in the LK model noise does not significantly affect the average transient time or its distribution for realistic parameter values. This demonstrates that the transient LFFs is mainly a deterministic phenomenon, its duration being determined by the various model parameters that affect the time needed to go from the fixed point of the solitary laser to a stable ECM. We have also shown that sufficiently large values of the noise strength can induce escapes from the stable ECM, leading to regimes of power dropouts alternating with intervals of stable steady-state emission. This behavior provides evidence that transient LFFs are excitable due to the effect of noise.

We presented an in-depth analysis of the statistical properties of this transient

dynamics, and investigated the influence of different parameters. Our results show that the chaotic attractor of the transient LFFs has statistical properties similar to those of the experimentally observed stationary LFF regime. We also show that the nonlinear gain saturation coefficient, which represents various gain saturation effects, plays a key role in determining the duration of the LFF lifetime: a small variation of the saturation coefficient results in a drastic increase of the duration of the LFF transient. Nonlinear gain saturation also increases the probability of noise-induced escapes, and therefore, our results suggest that the LFFs observed in experiments can be, at least in part, sustained by various nonlinear light-matter interactions in the laser active medium.

Finally, we have compared the behavior of the delay-differential LK model with that of a phenomenological ODE model [124] operating in the excitable regime and with appropriate initial conditions. This comparison shows that noise plays an important role in the transient dynamics when the dimensionality of the system is low, but not when it is large (due to the explicit delay in the LK model).

Chapter 7

Quorum sensing and crowd synchrony in delay-coupled semiconductor lasers

In this chapter we study the phenomena of crowd synchrony and quorum sensing in a star-type network of mutually delayed-coupled non-identical semiconductor lasers [195].

As discussed in Chapter 3, studies of crowd synchrony and quorum sensing to date have considered the coupling with the medium to be instantaneous [166, 167, 170, 196, 197]. This naturally results in synchronous behavior with zero time lag between any pair of elements in the system. However, in many situations the transmission of the coupling signal takes an amount of time that is non-negligible with respect to the characteristic time scales of the system components. This is the case e.g. in systems of technological importance such as optically coupled semiconductor lasers. When these devices are separated distances on the order of centimeters, they are subject to coupling delays on the order of the characteristic time scales of solitary lasers (shorter than nanoseconds).

In recent years much effort has been devoted to understand the synchronization of semiconductor lasers. This is important for technological reasons, i.e., to achieve large output powers, but also for increasing our knowledge of how generic dynamical systems synchronize. Semiconductor lasers are low-cost, versatile, and many of the commercial lasers are well-described theoretically. They show a large variety of non-linear dynamics as discussed in Chapter 3. However, most studies of coupled lasers so far have considered a small number of elements. Thus, how to achieve synchronization for a large number of coupled non-identical lasers is still an open question.

Isochronal synchronization is relevant in both technological [198] and biological [199] contexts. In this chapter we show that M semiconductor lasers coupled through a central laser exhibits zero-lag crowd synchronization. Here the central laser operates in a passive regime (below threshold), and plays the role of a coupling medium analogous to the bridge structure in pedestrian synchronization [166], and to the reaction medium in chemical synchronization [170]. Our results show that the general properties of both the crowd synchrony and the quorum-sensing transition are readily reproduced with this setup.

7.1 Modeling framework

A collection of M semiconductor lasers bidirectionally coupled through a central laser is schematically represented in Fig. 7.1 with the same coupling topology as in the cases of the Millennium Bridge [166] and the chemical oscillators in [170] but with a time delay τ in the coupling.

The equations describing this coupling scheme is a generalization of the case of two identical oscillators coupled through a third central element [153, 154, 155, 152, 164, 200]. In our scheme the central laser is emitting an amount of light that is injected to each of the outer lasers. The slow envelope of the complex electric field

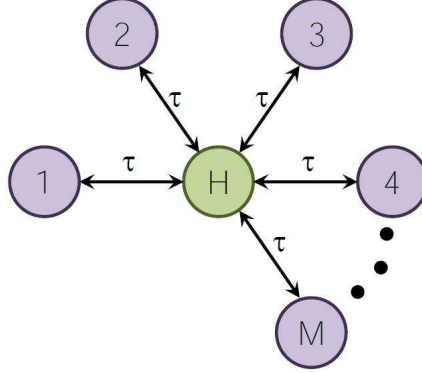


Figure 7.1: Scheme of M star-coupled lasers with a central laser, H , with a time delay of τ .

E and the carrier number N for the M lasers and the central laser are [152]

$$\begin{aligned} \dot{E}_j &= i\omega_j E_j + k(1 + i\alpha)(G_j - 1)E_j + \kappa E_H(t - \tau)e^{-i\omega_0\tau} \\ &\quad + \sqrt{D}\xi_j(t) \end{aligned} \quad (7.1)$$

$$\begin{aligned} \dot{E}_H &= i\omega_H E_H + k(1 + i\alpha)(G_H - 1)E_H + \kappa \sum_{j=1}^M E_j(t - \tau)e^{-i\omega_0\tau} \\ &\quad + \sqrt{D}\xi_H(t) \end{aligned} \quad (7.2)$$

$$\dot{N}_{j,H} = \gamma_N (\mu_{j,H} - N_{j,H} - G_{j,H}|E_{j,H}|^2) \quad (7.3)$$

where

$$G_{j,H} = \frac{N_{j,H}}{1 + \varepsilon |E_{j,H}|^2}, \quad (7.4)$$

and the subscripts H and j denote the central (hub) laser and j th outer (star) laser, respectively. In this context, all the parameters have the same meaning as in section 2.1. The field and carrier decay rates are k and γ_N , respectively, α is the linewidth enhancement factor, ε is the gain saturation, ω_0 is the optical frequency and ω_H and ω_j are the detuning of the hub and the star lasers with respect to the reference frequency ω_0 . The coupling is characterized by its strength κ and delay τ , both of which are assumed equal for all lasers. $\mu_j = \mu$ and μ_H are the pump currents of the

star and hub lasers, respectively. Finally, $\xi_j(t)$ and $\xi_H(t)$ are uncorrelated complex Gaussian white noises, with D being the noise strength. The model was integrated with the stochastic Heun algorithm with a time step of 0.8 ps, using parameter values typical for semiconductor lasers: $k = 300 \text{ ns}^{-1}$, $\gamma_N = 1 \text{ ns}^{-1}$, $\alpha = 3$, $D = 10^{-5} \text{ ns}^{-1}$, $\omega_0 = 2\pi c/\lambda$ (where c is the speed of light and $\lambda = 654 \text{ nm}$). $\omega_H = 0$ without loss of generality, and ω_j is chosen from a Gaussian distribution with zero mean and standard deviation σ . In what follows we neglect nonlinear gain saturation ($\varepsilon = 0$), since it does not affect the results obtained as discussed later. Unless otherwise stated $\sigma = 20\pi \text{ rad/ns}$, corresponding to $\Delta\lambda = 0.014 \text{ nm}$, and $\tau = 5 \text{ ns}$.

7.2 Zero-lag synchronization of a network of coupled lasers

Figure 7.2 shows the stationary emitted intensity for varying number of star lasers when the star-lasers are pumped above threshold. For small M [Fig. 7.2(a)] the lasers oscillate independently. By increasing M , synchronized emission at near zero-lag occurs for lasers with similar frequencies, forming clusters with similar dynamics as shown in Fig. 7.2(b). The number of synchronized lasers in those clusters grows as M increases [Fig. 7.2(c)], with an emission characterized by short pulses of irregular amplitudes with a repetition period around 2τ . Those characteristics become more evident for large M , where almost all the lasers emit synchronously at zero lag [Fig. 7.2(d)], with emission pulses taking place simultaneously in most of the lasers. This situation is reached provided the pump current of the hub laser is set below the solitary lasing threshold, i. e. $\mu_H < \mu_{th} = 1$. In the case that the hub laser is pumped above the solitary threshold, $\mu_H > \mu_{th}$, the synchronized state emerges progressively but without clustering, as a direct consequence of the intrinsic dynamics of the hub.

When the star-lasers are pumped below threshold, i. e. all the lasers including the hub are below threshold, the synchronization arises sharply so only a small increase

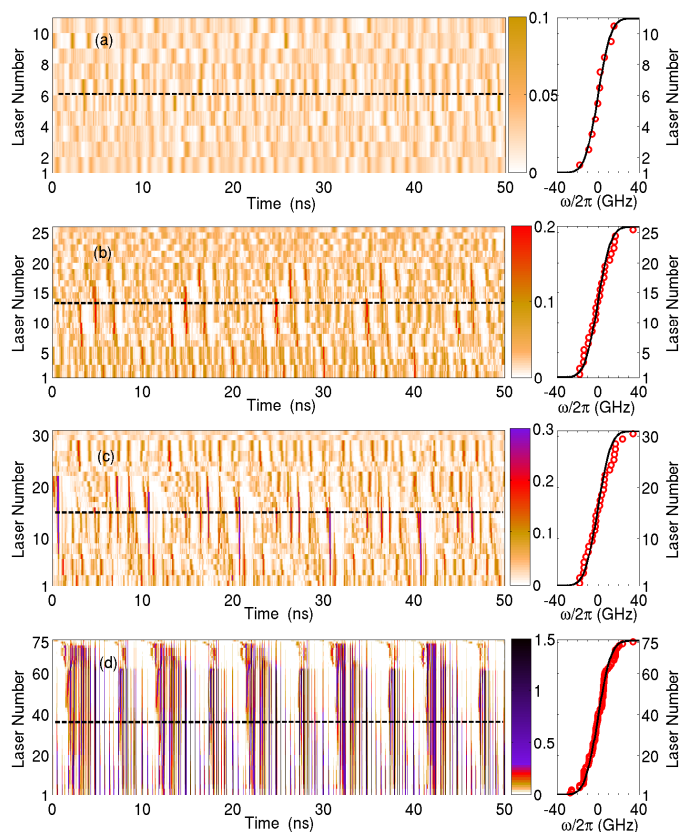


Figure 7.2: Synchronization of star-coupled semiconductor lasers for increasing number of elements, M . The color coding shows the intensity for each star laser as a function of time. In the vertical axis the lasers are sorted by their solitary frequency, ω_j , with number 1 corresponding to the most negative detuning. The black dashed line shows the laser for which $\omega = 0$. (a) $M = 10$, (b) $M = 25$, (c) $M = 30$ and (d) $M = 75$. The right column shows the frequency $\omega_j/2\pi$ of the lasers (dots), in relation with the normalized cumulative Gaussian distribution (solid line). The pump currents are $\mu = 1.02$ and $\mu_H = 0.4$, and the coupling strength $\kappa = 30 \text{ ns}^{-1}$.

in the number of coupled lasers is required in order to synchronize their outputs (Fig. 7.3). Notice that in this case the synchronized dynamics is completely different to the previous case with the outer lasers above the solitary threshold. When pumped below the solitary injection current threshold the coherent dynamics is characterized by a mostly constant intensity with small periodic fluctuations, also with a period of 2τ , as shown in Fig. 7.3(b) that decreases in amplitude when M increases. It can be observed that not all the lasers have the same output intensity, reaching higher intensities the lasers with negative detuning frequency which is a direct consequence of the asymmetry in the frequencies introduced by the α factor.

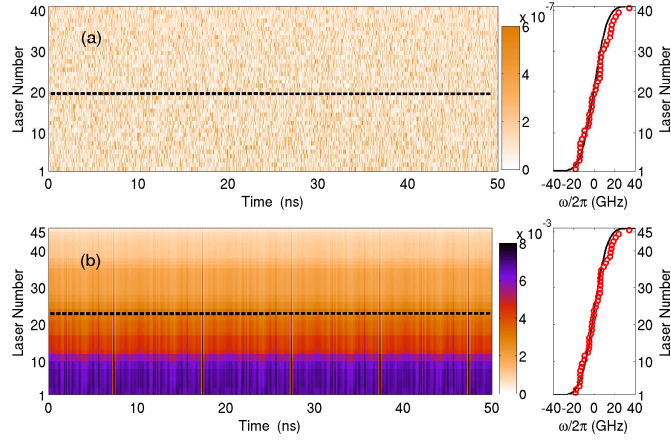


Figure 7.3: Same as in Fig. 7.2 for a pump currents of $\mu = 0.7$ and $\mu_H = 0.4$. (a) $M = 40$ and (b) $M = 45$.

In order to quantify the level of zero-lag synchronization, we calculated the total coherent intensity of the star lasers as

$$I = \left| \sum_{j=1}^M E_j(t) \right|^2. \quad (7.5)$$

Figure 7.4 compares the dynamics of this quantity with that of the intensity $|E_H|^2$ of the hub for increasing number of lasers. For increasing values of M , Fig. 7.4 shows

the emergence of large intensity pulses in the total coherent intensity, corresponding to strongly synchronized activity in Figs. 7.4(b-d). The hub laser reproduces these dynamics after a time τ . This is reflected in a large peak at time $-\tau$ in the cross-correlation function between $|E_H|^2$ and I , shown in Figs. 7.4(e-h). Thus, the hub laser lags behind the star lasers in the synchronized state.

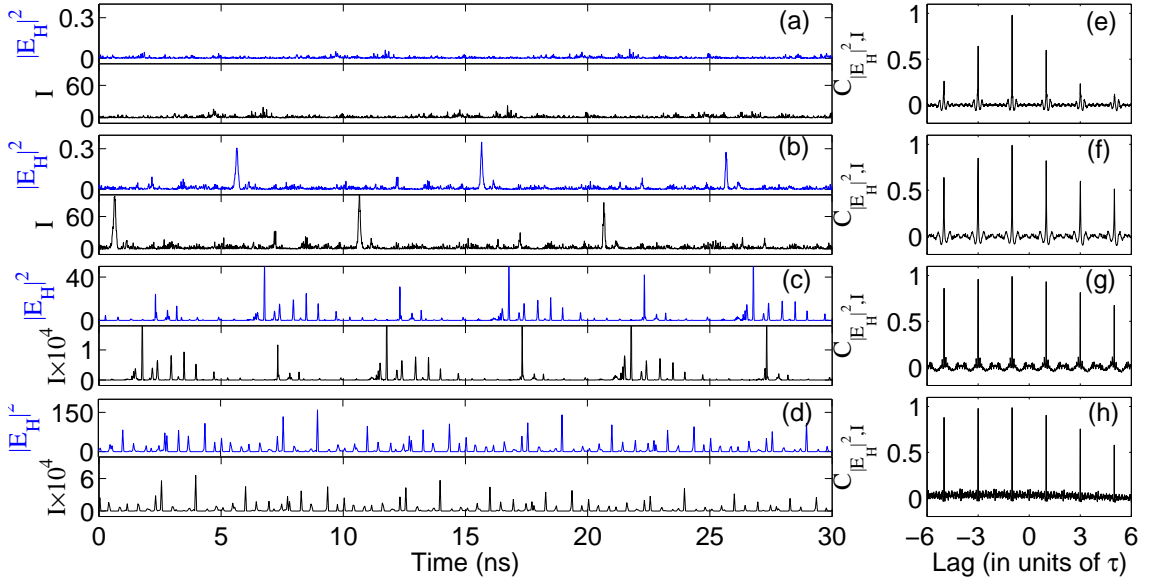


Figure 7.4: (a-d) Time trace for the intensity of the hub laser, $|E_H|^2$ (top trace, blue), and for the coherent intensity, I (bottom trace, black). (e-h) Cross-correlation function between $|E_H|^2$ and I . The number of lasers is $M = 25$ (a,e), $M = 30$ (b,f), $M = 75$ (c,g) and $M = 100$ (d,h). The parameters are the same as in Fig. 7.2.

7.2.1 Transition to the synchronized state

To investigate the transition to the synchronized state, we use as order parameter the time-averaged total coherent intensity of the star lasers $\langle I \rangle$, where $\langle \cdot \rangle$ is the average over a time window of length $T = 4 \mu\text{s}$, calculated in the stationary state. In the absence of synchronization $\langle I \rangle$ grows linearly with M , while when synchronization

arises this linear dependence is lost.

Figure 7.5(a) shows the average coherent intensity as a function of the number of star lasers for different coupling strengths and pump currents. When the star lasers are pumped above the solitary threshold and for small coupling, $\langle I \rangle / M$ is approximately constant, corresponding to the case of the absence of synchronization. For moderate values of κ , on the other hand, the system becomes gradually synchronized as M increases. The transition to synchronization occurs for a critical number of coupled lasers M_c , which we quantify as the number of lasers for which the growth rate of $\langle I \rangle$ with M changes abruptly. For even larger κ the critical number of lasers needed for synchronization decreases.

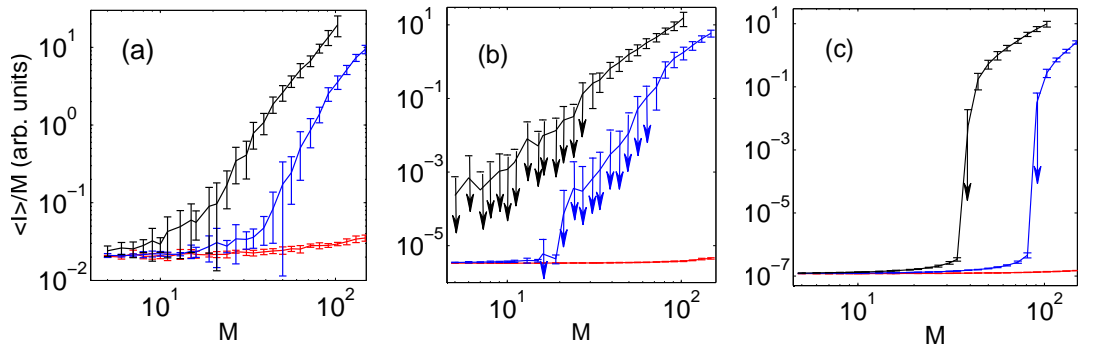


Figure 7.5: Ratio between the averaged coherent intensity $\langle I \rangle$ and the number of star lasers M , as a function of M itself and for different coupling strengths: $\kappa = 10 \text{ ns}^{-1}$ (red), $\kappa = 20 \text{ ns}^{-1}$ (blue) and $\kappa = 30 \text{ ns}^{-1}$ (black). (a) $\mu = 1.02$, $\mu_H = 0.4$. (b) $\mu = 0.99$, $\mu_H = 0.4$. (c) $\mu = 0.7$, $\mu_H = 0.4$. Each point is averaged over 10 to 40 different initial conditions and detuning frequencies. The arrows mark errorbars out of the axis limits.

The qualitative character of the synchronization transition can be changed by tuning the pump current μ of the star lasers below the laser threshold. When μ is well below threshold [Fig. 7.5(c)], the transition to synchronization is very sharp, in contrast with Fig. 7.5(a) above, provided coupling is large enough. Note that in this case both the star and hub lasers are pumped below their solitary threshold,

but are effectively above threshold due to coupling, and they turn on due to their spontaneous emission. The transition takes place when the star lasers are pumped at their solitary threshold [Fig. 7.5(b)], which shows the beginning of a sharp transition for intermediate κ (blue line) when the star lasers are pumped only slightly below threshold. We also note that this behavior requires that the hub laser be pumped below threshold, i. e. $\mu_H < \mu_{th} = 1$, otherwise the critical behavior is lost.

7.2.2 Minimum number of lasers for stable synchronization

One of the characteristic features of crowd synchronization is the scaling of the critical number of elements with the degree of diversity in the population and with the coupling coefficient [166]. In our case diversity is caused by the different frequencies ω_j of the lasers. Figures 7.6(a) and (b) show the dependence of the critical number of lasers on the width σ of the frequency distribution and on the coupling strength κ . The results show that M_c increases linearly with σ , while the dependence with κ follows a power law with negative exponent, as occurs in [166]. As expected, the larger σ the more different the lasers, and more lasers are required to generate the synchronized state. A broad frequency distribution leads to a reduction in the size of the clusters of lasers with similar ω_j showed in Fig. 7.2(b), and a corresponding decrease in the coherent intensity. On the other hand, the larger the coupling strength the smaller the minimum number of lasers required to synchronize the system [Fig. 7.6(b)].

We have also considered the effect of the coupling delay τ on the transition to the synchronized state. As shown in Fig. 7.6(c), for short delays (compared with the characteristic time scales of the laser) M_c exhibits a sharp resonance at a τ corresponding to the cavity decay time, but for longer delays M_c is reduced and is almost independent of τ . When the coupling delays are not identical[201], results similar to those of Fig. 7.5 are found, but for larger coupling strengths. In that case the synchronized dynamics may be characterized by periodic fluctuations of small

amplitude, or even steady state emission.

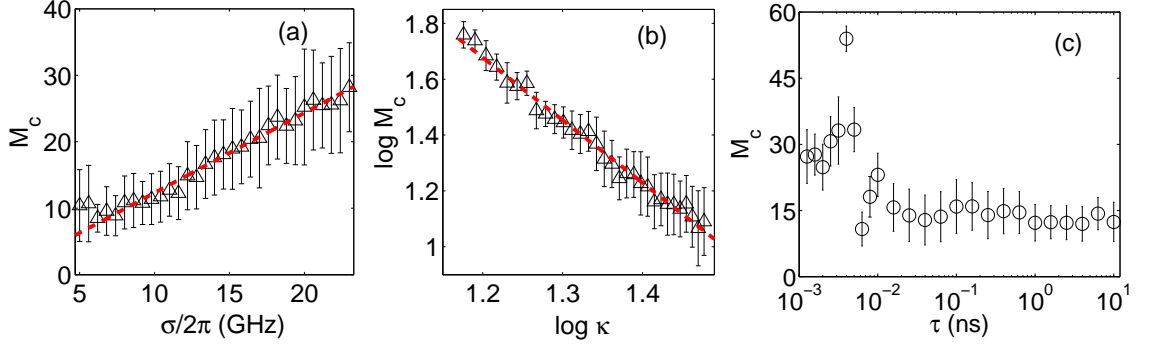


Figure 7.6: Critical number of lasers, M_c , as a function of different system parameters, for pump currents $\mu = 1.02$, $\mu_H = 0.4$. (a) M_c as a function of the width of the frequency distribution, σ . The dashed line shows a linear fit for $\sigma/2\pi > 6$ GHz ($M_c \propto 1.2\sigma$, $r^2 = 0.982$). Other parameters are $\kappa = 30 \text{ ns}^{-1}$ and $\tau = 5 \text{ ns}$. (b) Doubly logarithmic plot of M_c as a function of the coupling strength κ . The dashed line shows a power-law fit of the data ($M_c \propto 1/\kappa^{2.2}$, $r^2 = 0.987$). Other parameters are $\sigma = 20\pi \text{ rad/ns}$ and $\tau = 5 \text{ ns}$. (c) M_c as a function of the time delay, τ . Other parameters are $\kappa = 30 \text{ ns}^{-1}$ and $\sigma = 20\pi \text{ rad/ns}$. The simulations are averaged over 20 stochastic realizations of the initial conditions and frequency distribution.

7.3 Conclusions and discussion

In conclusion, we have shown numerically that a system of non-identical semiconductor lasers coupled to a common hub laser with time delay can be synchronized with zero lag. The transition to the synchronization occurs above a certain critical number M_c of coupled lasers, provided the pump current of the hub laser is smaller than the solitary pump current threshold μ_{th} . The type of synchronization transition can be controlled via the pump current of the star lasers: a gradual (second-order-like) transition is observed for star lasers with $\mu > \mu_{th}$, and an abrupt (first-order-like)

transition arises for $\mu < \mu_{th}$. A similar behavior has been exhibited by a chemical quorum sensing system [170].

The critical number of lasers increases linearly with the width of frequency distribution, and depends on the coupling strength via a power-law with negative exponent, in agreement with the crowd synchronization transition reported in the Millennium bridge [166]. On the other hand, the coupling delay reduces the critical number of lasers while it has no influence on it for large enough time delays, even though the delay is evident through the lag time with which the hub laser is synchronized with the star lasers, which are synchronized isochronously to one another. We have also considered a distribution of time delays which results in a decrease of the synchronization that can be recovered by increasing the coupling strength. A further investigation in this results should be interesting to better understand the synchronization of non-identical time delay couplings that frequently arise in experiments.

We are currently developing analytical expressions for M_c as a function of the parameters of the system as an extension of the theoretical analysis done in [202]. We are interested in the instability produced by the transition to the synchronized state, thus, we want to know for which parameters the unsynchronized state loses its stability. This problem can be solved by using linear perturbation theory around the unsynchronized steady state to obtain the critical parameter space boundary for synchronization. We expect that new analytical results will improve our knowledge on how the different parameters affect the synchronization transition.

Part III

FINAL REMARKS

Chapter 8

Summary of results and future work

This thesis is a contribution to the understanding of how stochastic and nonlinear phenomena in semiconductor lasers influences information processing and synchronization in these devices. The technological importance of semiconductor lasers and their rich variety of nonlinear dynamics have been the main motivation of our research.

The interplay between deterministic nonlinear dynamics and stochastic dynamics has been analyzed with the aim of exploiting the constructive effects that appear combining these two ingredients. The interplay of deterministic nonlinear dynamics, current modulation and noise leads to phenomena such as low frequency fluctuations, stochastic and coherent resonances, excitability and synchronization.

Noise is unavoidable in nature and is specially relevant in semiconductor lasers where random fluctuations due to the spontaneous emission are usually considered a drawback but, on the other hand, without noise a laser can not turn-on. A main point of this Thesis has been to demonstrate that the combination of noise and non-linearities can be exploited for innovative applications of semiconductor lasers.

8.1 Summary of results

The numerical simulations of rate equations for semiconductor lasers, as devoted in this Thesis, are important for the prediction and better understand the dynamics in these devices. The use of nonlinear effects to generate reliable and useful signals have been proposed in this Thesis and new phenomena have been observed and studied in laser with optical feedback and in a coupled network with delay. We hope that the contribution of our research will motivate new studies in laser dynamics and in non-linear science. Here we briefly highlight the main results obtained.

The critical slowing down that occurs close to the bifurcation points can be used to generate an optimal signal in VCSELs. In Chapter 4 we showed that VCSELs with direct asymmetric current modulation emit sharp sub-nanosecond pulses of irregular amplitude in two orthogonal linear polarizations even for pump currents, on average, below the solitary laser threshold, leading to an effective threshold reduction of about 20%. We have shown that pulses with maximum intensity and amplitude and minimum dispersion are emitted for an optimal current modulation asymmetry. The interplay between spontaneous emission noise and the radiation left by the previous pulse are responsible of the emission of that pulses for a slow rising and a fast decreasing current modulation. On the other hand, for a fast rising and a slow decreasing ramp the pulses are suppressed. For an average current modulation above the solitary threshold, the optimal asymmetry moves to the opposite situation with a fast rising ramp followed by a slow decreasing one. The intensity-current response show kinks related with the appearance of new pulses on each modulation period for a large modulation amplitude. We have shown that both polarizations are sustained for a large range of pump currents contrary to what can be observed without current modulation where the simultaneous emission of the two polarizations is not allowed. Stochastic resonance have been observed leading to the maximum amplitude of pulses and the minimum dispersion for an optimal amount of spontaneous emission.

Logic Stochastic Resonance have been demonstrated as a reliable mechanism to

obtain a nonlinear logical operator due to the interplay between bistability, noise and an appropriate current modulation. In Chapter 5 we have shown this effect in VCSELs that can act as logic operators due to the effect of noise. Two logical input signals have been encoded in a three-level current modulation that varies the relative stability of the orthogonal linear polarizations of the laser. A logical response, encoded in the two orthogonal linear polarizations, have been obtained when the current modulation is adjusted to favor one polarization for two modulation levels and to favor the opposite polarization for the third modulation level. The VCSEL-based logic operator allows to reproduce the truth table for the fundamental logic operations AND, OR, NAND and NOR when an appropriate amount of noise induces the transition to the most stable polarization. An appropriate amount of noise leads to the diminution of the critical slowing down when the current modulation is varied between consecutive bits. We have demonstrated that VCSELs can act as reliable logic operators in a wide range of noise strengths and different laser characteristics, and becomes a promising mechanism for logic operations under a strong noise background.

Is well known that the regime of coexistence between stable emission and Low Frequency Fluctuations (LFFs) can be observed in semiconductor lasers with optical feedback for low pump currents and moderate feedback strengths. In this parameter region, the Lang-Kobayashi model shows chaotic transients, observed when the LFF dynamics stabilizes to the maximum gain mode after a certain time. In Chapter 6 we demonstrated the deterministic nature of the transient LFFs. In this regime, a moderate noise level has no influence on the statistics of the transient time. We studied how various model parameters representing different light-matter interactions affect the duration of these transients. A large enough noise strength allows to reproduce the coexistence regime, with alternance of chaotic transients and stable emission, which can lead to excitability and stochastic resonance effects. We have also found a qualitatively good agreement in the inter-dropout time for the transient regime with previous results obtained in the literature for the sustained LFFs. We

have also discussed the role of the chaotic dynamics of the transient LFFs by comparing the transients in the Lang-Kobayashi model with a phenomenological ODE model concluding that the noise plays an important role when the dimensionality of the system is low but not when it is large.

Finally, synchronization of independent non-identical oscillators coupled through a common element can be observed above a certain minimum number of coupled oscillators as occurs in crowd synchrony and in quorum sensing. In Chapter 7 we presented a general mechanism for the gradual transition observed in the emergence of crowd synchrony and for the sharp transition to the synchronized state in the case of quorum sensing. We discussed these in a system of star-coupled semiconductor lasers with time-delayed coupling and different optical frequencies. The transition occurs when the common laser, i.e. the hub laser, is pumped below its solitary threshold. We demonstrated that the kind of transition to the synchronized state can be controlled by the pump current of the outer, i.e. the star, lasers. A smooth transition above a critical number of coupled lasers, as occurs in the crowd synchrony can be observed when the star-lasers are pumped above the solitary laser threshold, while a sharp transition to the synchronized state, as in the quorum sensing transition, occurs when the star-lasers are pumped below the solitary laser threshold. We have studied the effect of different parameters in the minimum number of lasers required for the emergence of the synchronization. This number decreases as a power law of the coupling strength, while short time delays reduce the amount of lasers required for synchronization. We have shown that a large enough time delay, larger than the characteristic time scales of the system, does not affect the transition.

8.2 Perspectives for future work

During the work performed in this Thesis, several questions have arisen that can be the natural continuation of the investigations presented here. A few of these

questions are summarized below.

With respect to the dynamics of VCSELs with direct current modulation:

- Is it possible to control the polarization of the emitted pulses by tuning the parameters of the asymmetric modulation? Which could be interesting for the reliable transmission of signals in the pulses.
- Is it possible to implement a stochastic logic gate with VCSELs when the input logical signal is encoded in an optical injected signal? All-optical logic operations are the basis of a new generation of information processing devices. Optical injection in VCSELs can induce chaotic dynamics in both polarizations and the logic stochastic resonance could be different in this situation.
- Is it possible to increase the bit rate in both pulse generation and logical stochastic resonance? For practical applications high bit rates are required. A better control on the critical slowing down and polarization switching could improve the performance of the generated signals. Successful results could motivate the design and development of VCSELs with improved characteristics.
- Which is the impact of thermal effects in both pulse generation and stochastic logic gates? A more realistic model is needed in order to accurately predict experimental results. Thermal effects modify the polarization stabilities, thus the results shown in this Thesis could be extended to a more realistic situation. Furthermore, transverse modes, that also modify the polarization stabilities, could be considered in future investigations.

With respect to the dynamics studied in EELs:

- Which is the effect of multi-longitudinal mode emission in the duration of the transient LFF time? Most of the commercial EELs emit multiple longitudinal modes, and the complex interactions between them change the transient LFFs

dynamics. Specially interesting is the effect of self- and cross-saturations that strongly affect the coupling between longitudinal modes and the LFF dynamics induced by an external reflector.

- How to develop a mathematical framework for studying synchronization transitions controlled by the system size? A stability analysis of the rate-equation model presented in this Thesis will help to better understand the crowd synchrony and quorum sensing transitions. We expect that similar mathematical treatments will be possible in other systems that show system-size dependent synchronization.
- Are there other coupling topologies that allow for crowd synchrony and quorum sensing transitions? Similar results are expected for other dynamical network topologies with passive central elements, but there are other network topologies without a central element, such as scale-free networks, that show a critical behavior with the system size under appropriate conditions. It could be interesting, for instance, to study crowd synchrony and quorum sensing transitions in the framework of percolation theory.

In addition, we hope that the theoretical results presented in this thesis will motivate new experimental studies, such as:

- Dynamics of SCLs with asymmetric current modulation: experimental demonstration of subthreshold pulse generation.
- Experimental demonstration of stochastic logic resonance in VCSELs with direct aperiodic current modulation and aperiodic optical injection.
- Experimental characterization of the duration of the transient LFFs time.
- Experimental demonstration of the transition to crowd synchrony and quorum sensing in SCLs by tuning the pump current of the outer lasers.

Part IV

Bibliography

Bibliography

- [1] A. Einstein, *Zur Quantentheorie der Strahlung*, Physikalische Zeitschrift **18**, 121-128 (1917).
- [2] J. P. Gordon, H. Zeiger, C. H. Townes, *Molecular microwave oscillator and new hyperfine structure in microwave spectrum of NH_3* , Phys. Rev. **95**, 282 (1954).
- [3] A. L. Schawlow and C. H. Townes, *Infrared and optical masers*, Phys. Rev. **112**, 1940 (1958).
- [4] A. M. Prokhorov, *Molecular amplifier and generator for sub-millimeter waves*, J. Exptl. Theoret. Phys. USSR **34**, 1658 (1958).
- [5] T. H. Maiman, *Stimulated optical radiation in ruby*, Nature **187**, 493 (1960).
- [6] J. von Neumann, *Notes on the photon-disequilibrium-amplification scheme (JvN)*, IEEE J. Quant. Electron. **QE-23**, 659-673 (1987).
- [7] D. P. Russell, *An introduction to the development of the semiconductor laser*, IEEE J. Quant. Electron. **30**, 668 (1987).
- [8] N. G. Basov, O. N. Krokhin, and Y. M. Popov, *Application of molecular beams to the radiospectroscopic study of the rotation spectrum of molecules*, Sov. Phys. JEPT **13**, 1320 (1961).
- [9] M. I. Nathan, W. P. Dumke, G. Burbs, F. H. Dill, and G. J. Lasher, *Stimulated emission of radiation from GaAd p-n junction*, Appl. Phys. Lett. **1**, 62 (1962).

- [10] R. N. Hall, G. E. Fenner, J. D. Kingsley, T. J. Soltys, and R. O. Carlson, *Coherent light emission from GaAs junctions*, Phys. Rev. Lett. **9**, 366 (1962).
- [11] T. M. Quist, R. J. Keyes, W. E. Krag, B. Lax, A. L. McWhorter, R. H. Rediker, and H. J. Zeiger, *Semiconductor maser of GaAs*, Appl. Phys. Lett. **1**, 91 (1962).
- [12] H. Kroemer, *A proposed class of heterojunction injection lasers*, Proc. IEEE **51**, 1782-1783 (1963).
- [13] Zh. I. Alferov, and R. F. Kazarinov, *Semiconductor laser with electrical pumping*, USSR Patent 181737 (1963).
- [14] Zh. I. Alferov, V. M. Andreev, E. L. Portnoi, and M. K. Trukan, *AlAs-GaAs heterojunction injection lasers with low room-temperature threshold*, Fiz. Tekh. Poluprov **3**, 1328-1332 (1969).
- [15] Y. Nishimura, K. Kobayashi, T. Ikegami, and Y. Suematsu, *Hole-burning effect in semiconductor laser*, Proc. Int. Quantum Electronics Conf., Kyoto, Japan **20**, 8 (1970).
- [16] Y. Nishimura, K. Kobayashi, T. Ikegami, and Y. Suematsu, *Axial-mode interactions in a semiconductor laser*, (in Japanese) Trans. IECE Jpn., **QE71**, 1-14 (1971), Tech. Rep. Quant. Electron.
- [17] D. B. Keck, R. D. Maurer, and P. C. Schultz, *On the ultimate lower limit of attenuation in glass optical waveguides*, Appl. Phys. Lett. **22**, 307-309 (1973).
- [18] D. N. Payne and W. A. Gambling, *Zero material dispersion in optical bers*, Electron. Lett. **11**, 176-178 (1975).
- [19] K. Oe and K. Sugiyama, *GaInAsP/InP double-hetero structure lasers prepared by a new LPE apparatus*, Jpn. J. Appl. Phys. **15**, 740-741 (1976).

- [20] T. Yamamoto, K. Sakai, S. Akiba, and Y. Suematsu, *Fast pulse behavior of InGaAsP/InP double heterostructure lasers emitting at 1.27 μm* , Electron. Lett. **13**, 142-143 (1977).
- [21] S. Arai, M. Asada, Y. Suematsu, and Y. Itaya, *Room temperature CW operation GaInAsP/InP DH laser emitting at 1.51 μm* , Jpn. J. Appl. Phys. **18**, 2333-2334 (1979).
- [22] S. Akiba, K. Sakai, Y. Matsushima, and T. Yamamoto *Room-temperature C. W. operation of InGaAsP/InP heterostructure lasers emitting at 1.56 μm* , Electron. Lett. **15**, 606-607 (1979).
- [23] H. Kawaguchi, T. Takahei, Y. Toyoshima, H. Nagai, and G. Iwane, *Room-temperature C.W. operation of InP/InGaAsP/InP double heterostructure diode lasers emitting at 1.55 μm* , Electron. Lett. **15**, 669-700 (1979).
- [24] I. P. Kaminow, R. E. Nahory, M. A. Pollack, L. W. Stulz, and J. C. DeWinter, *Single-mode C. W. ridge-waveguide laser emitting at 1.55 μm* , Electron. Lett. **15**, 763-765 (1979).
- [25] H. Kogelnik and C. V. Shank, *Coupled wave theory of distributed feedback lasers*, J. Appl. Phys. **43**, 2327-2335 (1972).
- [26] K. Iga, T. Kambayashi, and C. Kitahara, *GaInAsP/InP surface emitting lasers (I)* presented at the 26th Spring Meeting of Applied Physics Societies, (in Japanese) (1978), 27p-C-1.
- [27] H. Soda, K. Iga, C. Kitahara, and Y. Suematsu, *GaInAsP/InP surface-emitting injection lasers*, Jpn. J. Appl. Phys **18**, 2329-2330 (1979).
- [28] Y. Suematsu and K. Iga, *Semiconductor lasers in photonics*, J. Lightw. Technol. **26**, 1132-1144 (2008).

- [29] F. Koyama, S. Kinoshita, and K. Iga, *Room temperature CW operation of GaAs vertical cavity surface emitting laser*, Trans. IEICE **E71**, 1089-1090 (1988).
- [30] R. P. Mirin, J. P. Ibbetson, K. Nishi, A. C. Gossard, and J. E. Bowers, *1.3 μ m photoluminescence from InGaAs quantum dots on GaAs*, Appl. Phys. Lett. **67**, 3795-3797 (1995).
- [31] J. A. Lott, N. N. Ledentsov, V. M. Ustinov, N. A. Maleev, A. E. Zhukov, A. R. Kovsh, M. V. Maximov, B. V. Volovik, Z. I. Alferov, and D. Bimberg, *InAs-InGaAs quantum dot VCSELs on GaAs substrates emitting at 1.3 μ m*, Electron. Lett. **36**, 1384-1385 (2000).
- [32] K. Otsubo, N. Hatorim, M. Ishida, S. Okumura, T. Akiyama, Y. Nakata, H. Ebe, M. Sugawara, and Y. Arakawa *Temperature-insensitive eyeopening under 10-Gb/s modulation of 1.3- μ m P-doped quantum-dot lasers without current adjustments*, Jpn. J. Appl. Phys. B **43**, L1124-1126 (2004).
- [33] J. Faist, F. Capasso, D. L. Sivco, C. Sirtori, A. L. Hutchinson, and A. Y. Cho, *Quantum Cascade Laser*, Science **264**, 553-556 (1994).
- [34] S. Nakamura, *Pulsed operation of violet laser diodes*, Electr. Mater., 159-164 (1996).
- [35] S. Nakamura, *Blue light emitting laser diodes*, Thin Solid Films **343-344**, 345-349 (1999).
- [36] M. Holub, J. Shin, S. Chakrabarti, and P. K. Bhattacharya, *Electrically-injected spin-polarized vertical-cavity surface-emitting lasers*, Appl. Phys. Lett., **87**, 091108 (2005).
- [37] M. Holub, J. Shin, D. Saha, and P. Bhattacharya, *Electrical spin injection and threshold reduction in a semiconductor laser*, Phys. Rev. Lett., **98**, 146603, (2007).

- [38] M. T. Hill, H. J. S. Dorren, T. de Vries, X. J. M. Leijtens, J. H. den Besten, B. Smalbrugge, Y. S. Oei, H. Binsma, G. D. Khoe, and M. K. Smit, *A fast low-power optical memory based on coupled micro-ring lasers*, Nature **432**, 206 (2004).
- [39] S. Kalusniak, H. J. Wünsche, and F. Henneberger, *Random Semiconductor Lasers: Scattered versus Fabry-Perot Feedback*, Phys. Rev. Lett. **106**, 013901 (2011).
- [40] Laser Focus World, *Diode-laser market grows at a slower rate*, <http://www.optoiq.com/index.html>, Feb. 1 (2005).
- [41] J-M Liu, *Photonic devices*, Cambridge University Press, Cambridge, England (2005).
- [42] D. Lenstra, B. H. Verbeek, and A. J. den Boef, *Coherence Collapse in Single-Mode Semiconductor Lasers Due to Optical Feedback*, IEEE J. Quantum Electron. **21**, 674 (1985).
- [43] B. Tromborg and J. Mørk, *Non-linear injection locking dynamics and the onset of coherence collapse in external cavity lasers*, IEEE J. Quantum Electron. **26**, 642 (1990).
- [44] C. Risch and C. Voumard, *Self-pulsation in the output intensity and spectrum of GaAs-AlGaAs cw diode lasers coupled to a frequency selective external optical cavity*, J. Appl. Phys. **48**, 2083 (1977).
- [45] J. Mørk, B. Tromborg, and P. L. Christiansen, *Bistability and low-frequency fluctuations in semiconductor-lasers with optical feedback - a theoretical-analysis*, IEEE J. Quantum Electron. **24**, 123-133 (1988).
- [46] N. Kikuchi, Y. Liu, and J. Ohtsubo, *Chaos control and noise suppression in external-cavity semiconductor lasers*, IEEE J. Quantum Electron. **33**, 56-65 (1997).

- [47] T. Heil, I. Fischer, and W. Elsaßer, *Coexistence of low-frequency fluctuations and stable emission on a single high-gain mode in semiconductor lasers with external optical feedback*, Phys. Rev. A **58**, R2672-R2675 (1998).
- [48] G. Huyet, S. Balle, M. Giudici, C. Green, G. Giacomelli, and J. R. Tredicce, *Low frequency fluctuations and multimode operation of a semiconductor laser with optical feedback*, Opt. Commun. **149**, 341-347 (1998).
- [49] J. Ohtsubo, *Feedback induced instability and chaos in semiconductor lasers and their applications*, Opt. Lett. **6**, 1-15 (1999).
- [50] J. N. Blakely, L. Illing, and D. J. Gauthier, *Controlling Fast Chaos in Delay Dynamical Systems*, Phys. Rev. Lett. **92**, 193901 (2004).
- [51] A. Ahlborn and U. Parlitz, *Chaos control using notch filter feedback*, Phys. Rev. Lett. **96**, 034102 (2006).
- [52] K. Iga, *Surface-emitting lasers - Its birth and generation of new optoelectronics field*, IEEE J. Sel. Top. Quantum Electron. **6**, 1201-1215 (2000).
- [53] F. Koyama, K. Morito, and K. Iga, *Intensity noise and polarization stability of GaAlAs/GaAs surface emitting lasers*, IEEE J. Quantum Electron **27**, 1410 (1991).
- [54] C. J. Chang-Hasnain, J. P. Harbison, G. Hasnain, A. C. VonLehmen, L. T. Florez, and N. G. Stoffel, *Dynamic, polarization, and transverse mode characteristics of vertical cavity surface emitting lasers*, IEEE J. Quantum Electron. **27**, 1402 (1991).
- [55] H. Li, T. L. Lucas, J. G. McInerney, and R. A. Morgan, *Transverse modes and patterns of electrically pumped vertical-cavity surface-emitting semiconductor lasers*, Chaos, Solitons and Fractals **4**, 1619 (1994).

- [56] T. Mukaihara, N. Ohnoki, Y. Hayashi, N. Hatori, F. Koyama, and K. Iga, *Polarization control of vertical-cavity surface-emitting lasers using a birefringent metal/dielectric polarizer loaded on top distributed Bragg reflector*, IEEE J Sel.Topics Quantum Electron. **1**, 667-673 (1995).
- [57] H. Saito, K. Nishi, S. Sugou, and Y. Sugimoto, *Coherent polarization stabilization in large-aperture rectangular post bottom-emitting vertical-cavity surface-emitting lasers*, Appl. Phys. Lett. **71**, 590 (1997).
- [58] P. Debernardi, J. M. Ostermann, M. Feneberg, C. Jalics, and R. Michalzik, *Reliable polarization control of VCSELs through monolithically integrated surface gratings: a comparative theoretical and experimental study*, IEEE J. Sel. Top. Quantum Electron. **11**, 107-116 (2005).
- [59] K. Hasebe, F. Koyama, N. Nishiyama, C. Caneau, and C. E. Zah, *All-optical polarization controller using elliptical-apertured 1.5 μm VCSEL*, presented at the Conf. Lasers and Electro-Optics, Long Beach, CA, Paper CWP1 (2006).
- [60] M. C. Y. Huang, Y. Zhou, and C. J. Chang-Hasnain, *A surface-emitting laser incorporating a high-index-contrast subwavelength grating*, Nat. Photonics **1**, 119 (2007).
- [61] R. F. M. Hendriks, M. P. van Exter, J. P. Woerdman, A. van Geelen, L. Weegels, K. H. Gulden, and M. Moser, *Electro-optic birefringence in semiconductor vertical-cavity lasers*, Appl. Phys. Lett., **71**, 2599 (1997).
- [62] A. K. J. van Doorn, M. P. van Exter, and J. P. Woerdman, *Elasto-optic anisotropy and polarization orientation of vertical-cavity surface-emitting semiconductor lasers*, Appl. Phys. Lett. **69**, 1041 (1996).
- [63] M. San Miguel, *Semiconductor Quantum Optoelectronics*, Eds. A. Miller, M. Ebrahimzadeh and D.M Finlayson, Institute of Physics, Bristol 339-366 (1999).

- [64] J. Kaiser, C. Degen, and W. Elsässer, *Polarization-switching influence on the intensity noise of vertical-cavity surface-emitting lasers*, J. Opt. Soc. Am. B **19**, 672 (2002).
- [65] M. B. Willemsen, M. U. F. Khalid, M. P. van Exter, and J.P. Woerdman, J.P. *Polarization switching of a vertical-cavity semiconductor laser as a Kramers hopping problem*, Phys. Rev. Lett., **82** 4815-4818 (1999).
- [66] F. Prati, G. Giacomelli, and F. Marin, *Competition between orthogonally polarized transverse modes in vertical-cavity surface-emitting lasers and its influence on intensity noise*, Phys. Rev. A., **62** 033810 (1999).
- [67] K. D. Choquette, R. P. Schneider, K. L. Lear, and R. E. Leibenguth, *Gain-dependent polarization properties of vertical-cavity lasers*, IEEE J. Select. Top. Quantum Electron. **1**, 661 (1995).
- [68] A. Valle, K. A. Shore, and L. Pesquera, *Polarization selection in birefringent VCSELs*, J. Lightwave Technol. **14**, 2062 (1996).
- [69] K. Panajotov, B. Ryvkin, J. Danckaert, M. Peeters, H. Thienpont, and I. Veretennicoff, *Polarization switching in VCSEL's due to thermal lensing*, IEEE Photon. Technol. Lett. **10**, 6 (1998).
- [70] K. D. Choquette, K. L. Lear, R. P. Schneider, Jr., R. E. Leibenguth, J. J. Figiel, S. P. Kilcoyne, M. Hagerott-Crawford, and J. C. Zolper, *Polarization characteristics, control, and modulation of vertical-cavity surface emitting lasers*, Proc. SPIE **2382**, 125 (1995).
- [71] J. Martín-Regalado, J. L. A. Chilla, J. J. Rocca, and P. Brusenbach, *Polarization switching in vertical-cavity surface emitting lasers observed at constant active region temperature*, Appl. Phys. Lett. **70**, 3350 (1997).
- [72] M. San Miguel, Q. Feng, and J. V. Moloney, *Light-Polarization dynamics in surface-emitting semiconductor lasers*, Phys. Rev. A **52**, 1728 (1995).

- [73] J. Martín-Regalado, M. San Miguel, N. B. Abraham, and F. Prati, *Polarization properties of vertical-cavity surface-emitting lasers*, IEEE J. Quantum Electron. **33**, 765 (1997).
- [74] J. Martín-Regalado, S. Balle, M. San Miguel, A. Valle, and L. Pesquera, *Polarization and transverse-mode selection in quantum-well vertical-cavity surface-emitting lasers: index- and gain-guided devices*, Quantum Semiclass. Opt. **9**, 713 (1997).
- [75] C. O. Weiss and R. Vilaseca, (1991), *Dynamics of lasers*, VCH Verlagsgesellschaft, Weinheim, Germany.
- [76] R. Lang and K. Kobayashi, *External Optical Feedback Effects on Semiconductor Injection Laser Properties*, IEEE J. Quantum Electron. **16**, 347 (1980).
- [77] C. H. Henry, *Theory of the linewidth of SCLs*, IEEE J. Quantum Electron. **18**, 259 (1982).
- [78] G. P. Agrawal and N. K. Dutta, *Long-wavelength semiconductor lasers*, New York: Van Nostrand Reinhold (1986).
- [79] M. Hofmann, M. Koch, H. J. Heinrich, G. Weiser, J. Feldmann, W. Elsässer, E. O. Göbel, W. W. Chow, and S. W. Koch, *Temporal and spectral gain dynamics in an actively mode-locked semiconductor-laser*, IEE Proc.-J: Optoelectron. **141**, 127 (1994).
- [80] A. M. Levine, G. H. M. van Tartwijk, D. Lenstra, and T. Erneux, *Diode lasers with optical feedback: Stability of the maximum gain mode*, Phys. Rev. A **52**, 3436 (1995).
- [81] S. Barland, P. Spinicelli, G. Giacomelli, and F. Marin, *Measurement of the working parameters of an air-post vertical-cavity surface-emitting laser*, IEEE J. Quantum Electron. **41**, 1235-1243 (2005).

- [82] M. Giudici, C. Green, G. Giacomelli, U. Nespolo, and J. R. Tredicce, *Andronov bifurcation and excitability in semiconductor lasers with optical feedback*, Phys. Rev. E **55**, 6414 (1997).
- [83] J. Mulet and C. R. Mirasso, *Numerical statistics of power dropouts based on the Lang-Kobayashi model*, Phys. Rev. E **59**, 5400 (1999).
- [84] S. Wieczorek, B. Krauskopf, and D. Lenstra, *Multipulse Excitability in a Semiconductor Laser with Optical Injection*, Phys. Rev. Lett. **88**, 063901 (2002).
- [85] I. Fischer, G. H. M. van Tartwijk, A. M. Levine, W. Elsässer, E. Göbell, and D. Lenstra, *Fast Pulsing and Chaotic Itinerancy with a Drift in the Coherence Collapse of Semiconductor Lasers*, Phys. Rev. Lett. **76**, 220 (1996).
- [86] T. Heil, I. Fischer, W. Elsässer, J. Mulet, and C. R. Mirasso, *Chaos synchronization and spontaneous symmetry-breaking in symmetrically delay-coupled semiconductor lasers*, Phys. Rev. Lett. **86**, 795 (2001).
- [87] S. Wieczorek, T. B. Simpson, B. Krauskopf, and D. Lenstra, *Global quantitative predictions of complex laser dynamics*, Phys. Rev. E **65**, 045207(R) (2002).
- [88] A. Hohl, A. Gavrielides, T. Erneux, and V. Kovanis, *Localized Synchronization in Two Coupled Nonidentical Semiconductor Lasers*, Phys. Rev. Lett. **78**, 4745 (1997).
- [89] V. Ahlers, U. Parlitz, and W. Lauterborn, *Hyperchaotic dynamics and synchronization of external-cavity semiconductor lasers*, Phys. Rev. E **58**, 7208 (1998).
- [90] C. Masoller, *Anticipation in the Synchronization of Chaotic Semiconductor Lasers with Optical Feedback*, Phys. Rev. Lett. **86**, 2782 (2001).
- [91] J. M. Buldú, T. Heil, I. Fischer, M. C. Torrent, and J. García-Ojalvo, *Episodic Synchronization via Dynamic Injection*, Phys. Rev. Lett. **96**, 024102 (2006).

- [92] D. W. Sukow, A. Gavrielides, T. Erneux, B. Mooneyham, K. Lee, J. McKay, and J. Davis, *Asymmetric square waves in mutually coupled semiconductor lasers with orthogonal optical injection*, Phys. Rev. E **81**, 025206(R) (2010).
- [93] P. Mandel, *Theoretical Problems in Cavity Nonlinear Optics*, Cambridge University Press, Cambridge, England (1997).
- [94] J. R. Tredicce, G. L. Lippi, P. Mandel, B. Charasse, A. Chevalier, and B. Picque, *Critical slowing down at a bifurcation*, Am. J. Phys. **72**, 799 (2004).
- [95] M. C. Torrent and M. San Miguel, *Stochastic-dynamics characterization of delayed laser threshold instability with swept control parameter*, Phys. Rev. A **38**, 245 (1988).
- [96] C. Masoller, M. S. Torre, P. Mandel, *Influence of the injection current sweep rate on the polarization switching of vertical-cavity surface-emitting lasers*, J. Appl. Phys. **99**, 026106 (2006).
- [97] J. Paul, C. Masoller, Y. Hong, P. S. Spencer, and K. A. Shore, *Experimental study of polarization switching of vertical-cavity surface-emitting lasers as a dynamical bifurcation*. Opt. Lett. **31**, 748-750 (2006).
- [98] G. P. Agrawal, *Effect of gain nonlinearities on period doubling and chaos in directly modulated semiconductor-lasers*, Appl. Phys. Lett. **49**, 1013-1015 (1986).
- [99] S. Bennett, C. M. Snowden and S. Iezekiel, *Nonlinear dynamics in directly modulated multiple-quantum-well laser diodes*, IEEE J. Quantum Electron. **33**, 2076-2083 (1997).
- [100] H. Lamela, G. Carpintero, and F. J. Mancebo, *Period tripling and chaos in the dynamic behavior of directly modulated diode lasers*, IEEE J. Quantum Electron. **34**, 1797-1801 (1998).

- [101] J. P. Toomey, D. M. Kane, M. W. Lee, and K. A. Shore, *Nonlinear dynamics of semiconductor lasers with feedback and modulation*, Opt. Express **18**, 16955 (2010).
- [102] A. Valle, L. Pesquera, S. I. Turovets, and J. M. Lopez, *Nonlinear dynamics of current-modulated vertical-cavity surface-emitting lasers* Opt. Commun. **208**, 173-182 (2002).
- [103] M. Sciamanna, A. Valle, P. Megret, M. Blondel, and K. Panajotov, *Nonlinear polarization dynamics in directly modulated vertical-cavity surface-emitting lasers*, Phys. Rev. E **68**, 016207 (2003).
- [104] A. Valle, M. Sciamanna, and K. Panajotov, *Nonlinear dynamics of the polarization of multitransverse mode vertical-cavity surface-emitting lasers under current modulation*, Phys. Rev. E **76**, 046206 (2007).
- [105] A. Valle, M. Sciamanna, and K. Panajotov, *Irregular pulsating polarization dynamics in gain-switched vertical-cavity surface-emitting lasers*, IEEE J. Quantum Electron. **44**, 136-143 (2008).
- [106] C. Masoller, M. S. Torre, and K. A. Shore, *Polarization dynamics of current-modulated vertical-cavity surface-emitting lasers*, IEEE J. Quantum Electron. **43**, 1074-1082 (2007).
- [107] A. Torcini, S. Barland, G. Giacomelli, and F. Marin, *Low-frequency fluctuations in vertical cavity lasers: Experiments versus Lang-Kobayashi dynamics*, Phys. Rev. A **74**, 063801 (2006).
- [108] T. Heil, I. Fischer, and W. Elsaßer, *Influence of amplitude-phase coupling on the dynamics of semiconductor lasers subject to optical feedback*, Phys. Rev. A **60**, 634-641 (1999).

- [109] J. Mørk, B. Tromborg, and P. L. Christiansen, *Chaos in Semiconductor Lasers with Optical Feedback: Theory and Experiment*, IEEE J. Quantum Electron. **28**, 93-108 (1992).
- [110] J. Ye, H. Li, and J. G. McInerney, *Period-doubling route to chaos in a semiconductor laser with weak optical feedback*, Phys. Rev. A **47**, 2249 (1993).
- [111] H. Li, J. Ye, and J. G. McInerney, *Detailed analysis of coherence collapse in semiconductor lasers*, IEEE J. Quantum Electron. **29**, 2421 (1993).
- [112] A. Ritter and H. Haug, *Theory of laser diodes with weak optical feedback. I. Small-signal analysis and side-mode spectra*, J. Opt. Soc. Am. B **10**, 145 (1993).
- [113] C. H. Henry and R. F. Kazarinov, *Instability of Semiconductor Lasers Due to Optical Feedback from Distant Reflectors*, IEEE J. Quantum Electron. **22**, 294 (1986).
- [114] J. Sacher, W. Elsässer, and E. O. Gobel, *Intermittency in the coherence collapse of a semiconductor-laser with external feedback*, Phys. Rev. Lett. **63**, 2224 (1989).
- [115] T. Sano, *Antimode dynamics and chaotic itinerancy in the coherence collapse of semiconductor lasers with optical feedback*, Phys. Rev. A **50**, 2719 (1994).
- [116] J. Hales, A. Zhukov, R. Roy, and M. I. Dykman, *Dynamics of Activated Escape and Its Observation in a Semiconductor Laser*, Phys. Rev. Lett. **85**, 78 (2000)
- [117] D. W. Sukow, J. R. Gardner, and D. J. Gauthier, *Statistics of power-dropout events in semiconductor lasers with time-delayed optical feedback*, Phys. Rev. A **56**, R3370-R3373 (1997).
- [118] Y. Hong and K. Shore, *Statistical measures of the power dropout ratio in semiconductor lasers subject to optical feedback*, Opt. Lett. **30**, 3332 (2005).

- [119] J. M. Buldú and J. García-Ojalvo, and M. C. Torrent, *Delay-induced resonances in an optical system with feedback*, Phys. Rev. E **69**, 046207 (2004).
- [120] Y. Hong and K. Shore, *Influence of Optical Feedback Time-Delay on Power-Drops in Vertical-Cavity Surface-Emitting Lasers*, IEEE J. Quantum Electron. **41**, 1054-1057 (2005).
- [121] A. Hohl, H. J. C. van der Linden, and R. Roy, *Determinism and stochasticity of power-dropout events in semiconductor lasers with optical feedback*, Opt. Lett. **20**, 2396 (1995).
- [122] W. S. Lam, P. N. Guzdar, and R. Roy, *Effect of spontaneous emission noise and modulation on semiconductor lasers near threshold with optical feedback*, Int. J. Mod. Phys. B, **17**, 4123-4138 (2003).
- [123] J. F. Martinez Avila, H. L. D. de S. Cavalcante, and J. R. Rios Leite, *Experimental deterministic coherence resonance*, Phys. Rev. Lett. **93**, 144101 (2004).
- [124] M. C. Eguia, G. B. Mindlin, and M. Giudici, *Low-frequency fluctuations in semiconductor lasers with optical feedback are induced with noise*, Phys. Rev. E **58**, 2636 (1998).
- [125] A. M. Yacomotti, M. C. Eguia, J. Aliaga, O. E. Martinez, G. B. Midlin, and A. Lipsich, *Interspike Time Distribution in Noise Driven Excitable Systems*, Phys. Rev. Lett. **83**, 292 (1999).
- [126] J. M. Méndez, J. Aliaga, and G. B. Mindlin, *Limits on the excitable behavior of a semiconductor laser with optical feedback*, Phys. Rev. E **71**, 026231 (2005).
- [127] J. F. Martinez Avila, H. L. D. de S. Cavalcante, and J. R. Rios Leite, *Coarse grained variables and deterministic chaos in an excitable system*, Phys. Rev. Lett. **100**, 044101 (2008).

- [128] C. H. Henry, *Theory of Spontaneous Emission Noise in Open Resonators and its Application to Lasers and Optical Amplifiers*, J. Lightwave Technol. **4**, 288-297 (1986).
- [129] D. Lenstra, G. Vemuri, S. Wieczorek, and M. I. Yousefi, *The influence of noise on the dynamics of semiconductor lasers*, Proc. of the society of photo-optical instrumentation engineers (spie) **5468**, 165-179 (2004).
- [130] H. Kramers, Physica (Utrecht) **7**, 284 (1940).
- [131] L. Gammaitoni, P. Hänggi, P. Jung and F. Marchesoni, *Stochastic resonance*, Rev. Mod. Phys. **70**, 223-287 (1998).
- [132] C. Nicolis, *Solar variability and stochastic effects on climate*, Sol Phys **74**, 473-478 (1981).
- [133] C. Nicolis and G. Nicolis *Stochastic aspects of climatic transitions - additive fluctuations*, Tellus **33**, 225 (1981).
- [134] S. Fauve and F. Heslot, *Stochastic resonance in a bistable system*, Phys. Lett. A **97**, 5 (1983).
- [135] B. McNamara, K. Wiesenfeld, and R. Roy, *Observation of Stochastic Resonance in a Ring Laser*, Phys. Rev. Lett. **60**, 2626 (1988).
- [136] J. K. Douglass, L. Wilkens, E. Pantazelou, and F. Moss, *Noise enhancement of information transfer in crayfish mechanoreceptors by stochastic resonance*, Nature **365**, 337-340 (1993).
- [137] F. Marino, M. Giudici, S. Barland, and S. Balle, *Experimental evidence of stochastic resonance in an excitable optical system*, Phys. Rev. Lett. **88**, 040601 (2002).
- [138] J. M. Buldú, J. García-Ojalvo, C. R. Mirasso, and M. C. Torrent, *Stochastic entrainment of optical power dropouts*, Phys. Rev. E **66**, 021106 (2002).

- [139] S. Barbay, G. Giacomelli, and F. Marin, *Stochastic resonance in vertical cavity surface emitting lasers*, Phys. Rev. E. **61**, 157-166 (2000).
- [140] B. Nagler, M. Peeters, I. Veretennicoff, and J. Danckaert, *Stochastic resonance in vertical-cavity surface-emitting lasers based on a multiple time-scale analysis*, Phys. Rev. E. **67**, 056112 (2003).
- [141] K. Wiesenfeld and F. Jaramillo, *Minireview of stochastic resonance*, Chaos **8**, 539 (1998).
- [142] K. Murali, S. Shina, W. L. Ditto and A. R. Bulsara, *Reliable logic circuit elements that exploit nonlinearity in the presence of a noise floor*, Phys. Rev. Lett. **102**, 104101 (2009).
- [143] S. Boccaletti, J. Kurths, G. Osipov, D. L. Valladares, and C. S. Zhou, *The synchronization of chaotic systems*, Phys. Rep. **366**, 1 (2002).
- [144] A. Pikovsky, M. Rosenblum, and J. Kurths, *Synchronization: A Universal Concept in Nonlinear Sciences*, Cambridge University Press, Cambridge, England, (2003).
- [145] M. Bennett, M. F. Schatz, H. Rockwood, and K. Wiesenfeld, *Huygens's clocks*, Proc. R. Soc. London **458**, 563-579 (2002).
- [146] J. Buck and E. Buck, *Mechanism of Rhythmic Synchronous Flashing of Fireflies*, Science **159**, 1319 (1968).
- [147] S. Wicczorek, T. B. Simpson, B. Krauskopf, and D. Lenstra, *Global quantitative predictions of complex laser dynamics*, Phys. Rev. E **65**, 045207R (2002).
- [148] J. García-Ojalvo, J. Casademont, C. R. Mirasso, M. C. Torrent, and J. M. Sancho, *Coherence and synchronization in diode-laser arrays with delayed global coupling*, Int. J. Bifurcation Chaos Appl. Sci. Eng. **9**, 2225 (1999).

- [149] C. M. Gonzalez, C. Masoller, C. Torrent, and J. García-Ojalvo, *Synchronization via clustering in a small delay-coupled laser network*, Europhys. Lett. **79**, 64003 (2007).
- [150] L. Goldberg, H. F. Taylor, J. F. Weller, and D. R. Scifres, *Injection locking of coupled-stripe diode laser arrays*, Appl. Phys. Lett. **46**, 236-238 (1985).
- [151] S. Wieczorek, *Stochastic bifurcation in noise-driven lasers and Hopf oscillators*, Phys. Rev. E. **79**, 036209 (2009).
- [152] I. Fischer, R. Vicente, J. M. Buldu, M. Peil, C. R. Mirasso, M. C. Torrent, and J. Garcia-Ojalvo, *Zero-Lag Long-Range Synchronization via Dynamical Relaying*, Phys. Rev. Lett. **97**, 123902 (2006).
- [153] H. G. Winful and L. Rahman, *Synchronized chaos and spatiotemporal chaos in arrays of coupled lasers*, Phys. Rev. Lett. **65**, 1575 (1990).
- [154] J. R. Terry, K. S. Thornburg Jr., D. J. DeShazer, G. D. VanWiggeren, S. Zhu, P. Ashwin, and R. Roy, *Synchronization of Chaos in an Array of Three Lasers*, Phys. Rev. E **59**, 4036 (1999).
- [155] I. Gomes da Silva, J. M. Buldu, C. R. Mirasso, J. Garcia-Ojalvo, *Synchronization by dynamical relaying in electronic circuit arrays*, Chaos **16**, 043113 (2006).
- [156] O. DHuys, R. Vicente, T. Erneux, J. Danckaert, and I. Fischer, *Synchronization properties of network motifs: Influence of coupling delay and symmetry*, Chaos **18**, 037116 (2008).
- [157] S. Hod, *Analytic Treatment of the Network Synchronization Problem with Time Delays*, Phys. Rev. Lett. **105**, 208701 (2010).

- [158] V. Flunkert, S. Yanchuk, T. Dahms, and E. Schöll, *Synchronizing Distant Nodes: A Universal Classification of Networks*, Phys. Rev. Lett. **105**, 254101 (2010).
- [159] P. R. Roelfsema, A. K. Engel, P. König, and W. Singer, *Visuomotor integration is associated with zero time-lag synchronization among cortical areas*, Nature (London) **385**, 157 (1997).
- [160] E. Klein, N. Gross, M. Rosenbluh, W. Kinzel, L. Khaykovich, and I. Kanter, *Stable isochronal synchronization of mutually coupled chaotic lasers*, Phys. Rev. E **73**, 066214 (2006).
- [161] J. F. Martinez Avila and J. R. Rios Leite, *Time delays in the synchronization of chaotic coupled lasers with feedback*, Opt. Express **17**, 21442 (2009)
- [162] M. Zigzag, M. Butkovski, A. Englert, W. Kinzel, and I. Kanter, *Zero-lag synchronization and multiple time delays in two coupled chaotic systems*, Phys. Rev. E **81**, 036215 (2010).
- [163] J. Mulet, C. Mirasso, T. Heil, and I. Fischer, *Synchronization scenario of two distant mutually coupled semiconductor lasers*, J. Opt. B **6**, 97 (2004).
- [164] S. Sivaprakasam, J. Paul, P. S. Spencer, P. Rees, and K. A. Shore, *Nullified time-of-flight lead-lag in synchronization of chaotic external-cavity laser diodes*, Opt. Lett. **28**, 1397 (2003).
- [165] P. Dallard, A. J. Fitzpatrick, A. Flint, S. LeBourva, A. Low, R. M. Ridsdill Smith, and M. Willford, *The London Millennium Footbridge*, Struct. Eng. **79**, 17-35 (2001).
- [166] S. H. Strogatz, D. M. Abrams, A. McRobie, B. Eckhardt, and E. Ott, *Crowd synchrony on the Millennium Bridge*, Nature **438**, 43 (2005).

- [167] B. Eckhardt, E. Ott, S. H. Strogatz, D. M. Abrams, and A. McRobie, *Modeling walker synchronization on the Millennium Bridge*, Phys. Rev. E **75**, 021110 (2007).
- [168] J. García-Ojalvo, M. B. Elowitz, and S. H. Strogatz, *Modeling a synthetic multicellular clock: Repressilators coupled by quorum sensing*, Proc. Natl. Acad. Sci. U.S.A. **101**, 10955 (2004).
- [169] S. Pratt, E. Mallon, D. Sumpter, and N. Franks, *Quorum sensing, recruitment, and collective decision-making during colony emigration by the ant *Leptothorax albipennis**, Behavioral Ecology and Sociobiology **52**, 117-127 (2002).
- [170] A. F. Taylor, M. R. Tinsley, F. Wang, Z. Huang, and K. Showalter, *Dynamical Quorum Sensing and Synchronization in Large Populations of Chemical Oscillators*, Science **323**, 614 (2009)
- [171] E. Sahin and N. Franks, *Measurement of Space: From Ants to Robots*, Proceedings of WGW 2002: EPSRC/BBSRC International Workshop, (2002).
- [172] L. Illing and M. B. Kennel, *Shaping current waveforms for direct modulation of semiconductor lasers*, IEEE J. Quantum Electron. **40**, 445-452 (2004).
- [173] X. Hachair, S. Barland, J. R. Tredicce, and G. L. Lippi, *Optimization of the switch-on and switch-off transition in a commercial laser*, Appl. Opt. **44**, 4761-4774 (2005).
- [174] J. Zamora-Munt and C. Masoller, *Generation of optical pulses in VCSELs below the static threshold using asymmetric current modulation*, Opt. Ex., **16**, 17848-17853 (2008).
- [175] C. E. Preda, B. Segard and P. Glorieux, *Weak temporal ratchet effect by asymmetric modulation of a laser*, Opt. Lett. **31**, 2347-2349 (2006).

- [176] K. Murali, I. Rajamohamed, S. Shina, W. L. Ditto, and A. R. Bulsara, *Realization of reliable and flexible logic gates using noisy nonlinear circuits*, Appl. Phys. Lett. **95**, 194102 (2009).
- [177] L. Worschech, F. Hartmann, T. Y. Kim, S. Hofling, M. Kamp, A. Forchel, J. Ahopelto, I. Neri, A. Dari, and L. Gammaitoni, *Universal and reconfigurable logic gates in a compact three-terminal resonant tunneling diode*, Appl. Phys. Lett. **96**, 042112 (2010).
- [178] W. L. Ditto, A. Miliotis, K. Murali, S. Sinha, and M. L. Spano, *Chaogates: Morphing logic gates that exploit dynamical patterns*, Chaos **20**, 037107 (2010).
- [179] D. N. Guerra, A. R. Bulsara, W. L. Ditto, S. Sinha, K. Murali, P. Mohanty, *A Noise-Assisted Reprogrammable Nanomechanical Logic Gate*, Nano Lett. **10**, 1168-1171 (2010).
- [180] K. P. Singh and S. Sinha, *Enhancement of “logical” responses by noise in a bistable optical system*, Phys. Rev. E **83**, 046219 (2011).
- [181] J. Zamora-Munt and C. Masoller, *Numerical implementation of a VCSEL-based stochastic logic gate via polarization bistability*, Opt. Ex., **18**, 16418 (2010).
- [182] C. Masoller and N. B. Abraham, *Low-frequency fluctuations in vertical-cavity surface-emitting semiconductor lasers with optical feedback*, Phys. Rev. A **59**, 3021-3031 (1999).
- [183] S. Balle, E. Tolkachova, M. San Miguel, J. R. Tredicce, J. Martin-Regalado, and A. Gahl, *Mechanisms of polarization switching in single-transverse-mode vertical-cavity surface-emitting lasers: thermal shift and nonlinear semiconductor dynamics*, Opt. Lett. **24**, 1121-1123 (1999).

- [184] G. Verschaffelt, J. Albert, I. Veretennicoff, J. Danckaert, S. Barbay, G. Giacomelli and F. Marin, *Frequency response of current-driven polarization modulation in vertical-cavity surface-emitting lasers*, App. Phys. Lett. **80**, 2248-2250 (2002).
- [185] C. Masoller and M. S. Torre, *Modeling thermal effects and polarization competition in vertical-cavity surface-emitting lasers*, Opt. Express **16**, 21282-21296 (2008).
- [186] M. Borromeo and F. Marchesoni, *Asymmetric probability densities in symmetrically modulated bistable devices*, Phys. Rev. E **71**, 031105 (2005).
- [187] S. Barbay, G. Giacomelli and F. Marin, *Noise-assisted binary information transmission in vertical cavity surface emitting lasers*, Opt. Lett. **25**, 1095-1097 (2000).
- [188] S. Barbay, G. Giacomelli, and F. Marin, *Noise-assisted transmission of binary information: Theory and experiment*, Phys. Rev. E **63**, 051110 (2001).
- [189] D. V. Dylov and J. W. Fleischer, *Nonlinear self-filtering of noisy images via dynamical stochastic resonance*, Nature Photon. **4**, 323-328 (2010).
- [190] C. Grebogi, E. Ott and J. A. Yorke, *Crises, sudden changes in chaotic attractors, and transient chaos*, Physica D **7**, 181 (1983).
- [191] J. Zamora-Munt, C. Masoller, and J. García-Ojalvo, *Transient low frequency fluctuations in semiconductor lasers with optical feedback*, Phys. Rev. A **81**, 033820 (2010).
- [192] J. Zamora-Munt, C. Masoller, and J. García-Ojalvo, *Multi-stability and transient chaotic dynamics in semiconductor lasers with time-delayed optical feedback*, World Scientific Publishing, p. 78-83 (2010).

- [193] J. M. Méndez, R. Laje, M. Giudici, J. Aliaga, and G. B. Mindlin, *Dynamics of periodically forced semiconductor laser with optical feedback*, Phys. Rev. E **63**, 066218 (2001).
- [194] R. Davidchack, Y.C. Lai, A. Gavrielides, and V. Kovanis, *Chaotic transitions and low-frequency fluctuations in semiconductor lasers with optical feedback*, Physica D **145**, 130 (2000).
- [195] J. Zamora-Munt, C. Masoller, J. García-Ojalvo and R. Roy *Crowd synchrony and quorum sensing in delay-coupled lasers*, Phys. Rev. Lett. **105**, 264101 (2010).
- [196] J. Aldridge and E. K. Pye, *Cell density dependence of oscillatory metabolism*, Nature **259**, 670 (1976).
- [197] S. De Monte, F. d'Ovidio, S. Danø, and P. G. Sørensen, *Dynamical quorum sensing: Population density encoded in cellular dynamics*, Proc. Natl. Acad. Sci. U.S.A. **104**, 18377 (2007).
- [198] R. Vicente, C. R. Mirasso, and I. Fischer, *Simultaneous bidirectional message transmission in a chaos-based communication scheme*, Opt. Lett. **32**, 403 (2007).
- [199] R. Vicente, L. L. Gollo, C. R. Mirasso, I. Fischer, G. Pipa *Relaying in the brain: a network topology capable of generating zero time-lag neuronal synchrony despite long conduction delays*, Proc. Natl. Acad. Sci. USA **105**, 17157 (2008).
- [200] B. B. Zhou and R. Roy, *Isochronal synchrony and bidirectional communication with delay-coupled nonlinear oscillators*, Phys. Rev. E **75**, 026205 (2007).
- [201] W. S. Lee, E. Ott, and T. M. Antonsen, *Large Coupled Oscillator Systems with Heterogeneous Interaction Delays*, Phys. Rev. Lett. **103**, 044101 (2009).

- [202] E. Ott and T. M. Antonsen, *Low dimensional behavior of large systems of globally coupled oscillators*, *Chaos* **18**, 037113 (2008).

Part V

Publications

List of publications

- J. Zamora-Munt and C. Masoller, *Generation of optical pulses in VCSELs below the static threshold using asymmetric current modulation*, Opt. Ex., **16**, 17848-17853 (2008).
- J. Zamora-Munt and C. Masoller, *Numerical implementation of a VCSEL-based stochastic logic gate via polarization bistability*, Opt. Ex., **18**, 16418 (2010).
- J. Zamora-Munt, C. Masoller, and J. García-Ojalvo, *Transient low frequency fluctuations in semiconductor lasers with optical feedback*, Phys. Rev. A **81**, 033820 (2010).
- J. Zamora-Munt, C. Masoller, and J. García-Ojalvo, *Multi-stability and transient chaotic dynamics in semiconductor lasers with time-delayed optical feedback*, World Scientific Publishing, p. 78-83 (2010).
- J. Zamora-Munt, C. Masoller, J. García-Ojalvo and R. Roy *Crowd synchrony and quorum sensing in delay-coupled lasers*, Phys. Rev. Lett. **105**, 264101 (2010).
- J. Zamora-Munt and C. Masoller, *Exploiting noise, nonlinearities and polarization bistability in vertical-cavity surface-emitting lasers*, Nonlinear Laser Dynamics-From Quantum Dots to Cryptography, Wiley-VCH, Ed. Kathy Lüdge, to be published.

Contributions in seminars, congress and workshops

- No-Linear'08 (Barcelona, 2008), *Emisión por Debajo del Umbral Estático en un Láser Tipo "Vertical-Cavity Surface-Emitting Laser" usando una Modulación Asimétrica de la Corriente de Inyección*, J. Zamora-Munt and C. Masoller. |P|
- FISES'09 (Huelva, 2009), *Chaotic transient dynamics in a semiconductor laser with optical feedback*, J. Zamora-Munt, C. Masoller, and J. García-Ojalvo. |P|
- LPHYS'09 (Barcelona, 2009), *Transient low frequency oscillations in semiconductor lasers with optical feedback*, J. Zamora-Munt, C. Masoller, and J. García-Ojalvo. |O|
- LPHYS'09 (Barcelona, 2009), *Sub-nanosecond pulses emitted by VCSELs subjected to asymmetric current modulation and operating below the static threshold*, J. Zamora-Munt and C. Masoller. |P|
- Delayed Complex Systems (Dresden, 2009), *Transient behaviour in the edge-emitting semiconductor lasers with optical feedback*, J. Zamora-Munt, C. Masoller, and J. García-Ojalvo. |P|
- PHYSCON 2009 (Catania, 2009), *Multi-stability and chaotic transient LFF*

dynamics in semiconductor lasers with time-delayed optical feedback, J. Zamora-Munt, C. Masoller, and J. García-Ojalvo. |O|

- QUONLOP 2011 (Valladolid, 2011), *Experimental study of different LFF regimes in semiconductor lasers with external cavities*, A. Aragoneses, J. Zamora-Munt, M. C. Torrent and C. Masoller. |P|
- Applied Dynamics Seminar (University of Maryland, 2011), *Crowd Synchrony and Quorum Sensing in Semiconductor Lasers*, J. Zamora-Munt, C. Masoller, J. García-Ojalvo, E. Ott and R. Roy. |O|
- FISES'11 (Barcelona, 2011), *Crowd Synchrony and Quorum Sensing Transition in Star-coupled Non-identical Semiconductor Lasers with Time Delay*, J. Zamora-Munt, C. Masoller, J. García-Ojalvo and R. Roy. |P|

|P|: Poster, |O|: Oral